UNIVERSITY OF TURKU

Microwave Processing of Black Mass from Spent Lithium-ion Batteries

Department of Mechanical and Materials Engineering
Master of Science in Technology Thesis

Author:
Md Mozammel Hossain

Supervisors:
Assoc. Prof. Pekka Peljo
Dr. Mamdouh Omran

March 2024
Turku

Master of Science in Technology Thesis
Subject: Materials Engineering
Author: Md Mozammel Hossain
Title: Microwave Processing of Black Mass from Spent Lithium-ion Batteries
Supervisor(s): Dr. Pekka Peljo, Dr. Mamdouh Omran
Number of pages: 97 pages
Date: March 2024

Abstract

In this Master's thesis, the effect of microwave radiation on the black mass derived from spent lithium-ion batteries was analysed with an aim of discovering an energy-efficient, and cost-effective route for recycling lithium-ion battery, and recovering valuable metals. Microwave heating requires less amount of energy compared to conventional heating while producing larger impact on the cracking of cathodic structures. Due to the inside-out heating mechanism volumetric and selective heating is possible with microwave radiation which increases the formation of easily leachable elements from the mixture of anode and cathode.

Theoretical section of this manuscript described the components of a battery. The chemical composition of the cathode and anode along with other parts such as electrolyte, current collector, and separator was being presented. Then the recent scenario of recycling and what are the industries that have already been taking the initiative was mentioned. After that, different methods of battery recycling were discussed. After taking their advantages and disadvantages into consideration, a combination of two processes were analysed. Finally, the theory behind microwave heating, their usage in different material processing sectors, and their application in battery recycling were discussed.

The results aligned with our objective of the thesis. After thermal treatment of the pre-processed samples in a microwave, the characterization was done using XRD, and SEM-EDX. On the other hand, to understand the thermal behaviour of those samples, TGA-DSC-MS was done as well in two different atmospheres (air, and inert). Results showed that the burning of the raw samples was better within the air atmosphere, because of the availability of oxygen. However, in an inert atmosphere, more elements were found in metallic form rather than in their oxide forms. Meanwhile, microwave radiation can enhance the breakdown of the cathode's structure. Therefore, the cathode materials were broken down into separate metals and metallic oxides just after processing at 400 ℃. The increasing temperature made the formation of metals within the sample easier and at the final stage of processing which was at 1200 ℃ metallic elements were dominant in the sample.

Key words: microwave heating, recycling, battery, metal recovery, pyrometallurgy.

Table of contents

1 Introduction

Technological advances sparked the development of machines driven by electricity. Hence, the demand for producing electrical energy is on the rise. A shift towards fossil-free energy production can be seen worldwide to reduce carbon emissions. However, renewable energy resources such as solar energy, wind energy, and geothermal energy are site-specific as well as fluctuating. To minimize the seasonal or daily variation, different types of electrical energy storage systems are being used. Lithium-ion batteries (LIBs) are one of the best options for short-term energy storage. Another growing sector where LIBs are being extensively used is transportation. An attempt to reduce the use of fossil fuel in the transport sector has enlarged the electric vehicle (EV) market. High volumetric and gravimetric energy density makes LIBs suitable for use in EVs. On top of that, portable devices, for example, laptop computers, mobile phones, and wearable devices are powered by LIBs. Thus, the demand and production of this battery have been increasing rapidly.

Despite being useful, LIBs pose a threat to the environment. They have an average lifespan of around 10-15 years which varies depending on the types and applications. Handling those spent batteries can be a challenging task due to their construction. The batteries consist of different organic and inorganic components, bonded tightly in a pack. Some of the materials used in the batteries can be harmful to the environment unless recycled properly. The cathode of these batteries is made with metallic oxides, mainly lithium, cobalt, nickel, iron, and manganese *etc*. Among them, lithium, cobalt, and nickel are very expensive and classified as critical raw materials by EU. Recovering them is of great importance both to the industry and to the scientific community. Proper recycling of spent batteries would bring environmental, social, and economic benefits.

The current recycling status is not satisfactory. Only a fraction of the waste is being handled properly and recovery of valuable metals is not sufficient. Recently, the hydrometallurgical process of recycling has become popular due to its high recovery rate. Also, the quality of the recovered materials is very high. However, the solvents required for the process are very expensive and they need to be handled carefully as they can otherwise be toxic for the environment. The other recycling method is the pyrometallurgical process, which is energy-intensive, has a low recovery rate, and recovered metals have inferior quality. Therefore, a combination of both processes can be implemented where the complex cathodic structure can be broken

down into easily soluble substances by applying high heat, and then leached out by hydrometallurgical technique.

The thermal pre-treatment of the black mass derived from the spent lithium-ion batteries can done using microwave radiation replacing conventional heating systems in the pyrometallurgical process. Microwave heating is considered rapid, volumetric, and low-cost. Since the primary energy source in microwave devices is electricity, the process can be realized by electricity from renewable sources as well. Therefore, the whole process of recycling would be cost-effective, energy-efficient, and environmentally friendly.

In this thesis work, the black mass from spent lithium-ion batteries was thermally treated under microwave radiation up to several different temperatures. After that, the characterisation of the treated materials was done to determine the effects of microwave radiation on black mass samples. The characterisation tools that were used in this work are, X-ray Diffraction (XRD), and Scanning Electron Microscopy coupled with Energy Dispersive X-ray Spectroscopy (SEM-EDX). Similarly, the effect of conventional heating has also been studied in different atmospheric conditions, namely, in air and under inert conditions using Thermogravimetric Analysis, Differential Scanning Calorimetry, and Mass Spectrometry (TGA-DSC-MS) experiments. A writing-assisted tool called ‘Grammarly’ was used in this report.

1.1 Objectives

1. Study the effects of microwave radiation on the decomposition of complex cathodic structures.

2. Study the effects of microwave radiation on the phase transformation of the complex structure of the cathode into simple metal oxides and metal forms.

3. Develop energy-efficient and effective recycling methods to improve the recovery of valuable metals from spent lithium-ion batteries.

2 Literature Review

Recently, lithium-ion batteries have been used in various applications such as Electric Vehicles (EVs), Energy Storage Systems and many other small-scale applications, like Cell Phones, Laptops, and wearable products (Figure 1). To counter the effects of pollution and to reduce the dependence on fossil fuels, EVs are gaining popularity worldwide. By using EVs in urban areas, air quality can be improved, and noise pollution can be reduced significantly [1]. Thus, the number of electric vehicles sold during the year 2022 has broken all the records. More than 26 million electric cars were on the road during that period which accounted for 60% more than the previous year. Although China experienced the highest growth, the same trend is followed in Europe as well, with 15% higher than in 2021 in 2022, when 2.7 million electric cars are on the streets [2]. This upward trend is expected to continue since the European Commission has taken some initiatives like Clean Planet for all and the European Strategy for low-emission mobility. Their main objective would be to reduce CO_2 emissions by 60% from the transport sector in 2050 compared to 1990 [3].

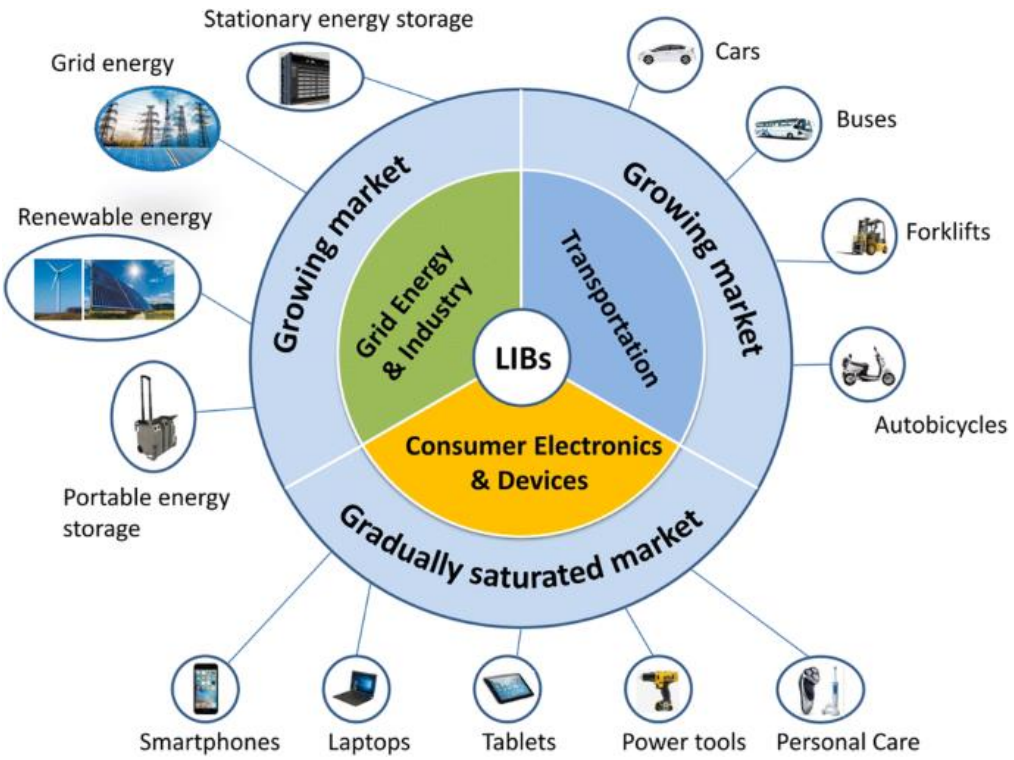

Figure 1: Different applications of lithium-ion battery. Reprinted from Electrochemical Energy Reviews, Volume No. 2, Yuanli Ding, Zachari P. Cano, Aiping yu, Jun Lu, Zhongwei Chang, Automotive Li-ion Batteries: Current Status and Future Perspective, Page no. 3, Copyright (2019), with permission from Springer Nature.

Another significant sector, where lithium batteries are being used is energy storage systems. In Europe, during the year 2020, almost 37% of the total electric energy was supplied from renewable sources [4]. Most of the renewable energy sources, such as solar, wind, hydropower and geothermal, are site-specific and unpredictable. Thus, it is important to reduce the power variation and increase the flexibility of the systems. To mitigate these problems, some kind of storage system is required with renewable energy systems [5]. Using, LIB has some advantages over other storage systems, for instance, self-discharge rate (8% per month) is very low, batteries have quick response, and their energy to weight ratio is comparatively high, LIBs longer lifetime, very high cycle efficiency compared to other batteries, and they can be environmentally friendly [6]. Because of these benefits, LIBs are being used in renewable energy storage systems. Additionally, several other devices have LIBs as a power source. Cell phones, laptops, wearable devices, and cameras are some of the products where LIBs are used [7].

2.1 Lithium-Ion Batteries

After the development of the first lithium-ion battery, extensive research has been done on this battery technology to increase the capacity, improve safety, and decrease the weight, and cost *etc*. Several changes have been made during these 30 years, for example replacing lithium metal with graphite as anode [8]. Generally, a lithium-ion battery consists of a positive electrode (cathode), a negative electrode (anode), an electrolyte solution or in some cases solid electrolyte, two current collectors (negative and positive) and a separator. A description and the typical materials used in these components is provided in the later section of the report.

2.1.1 Working Principles

A simple demonstration of the working principle of lithium-ion batteries has been illustrated in Figure 2. An ion-conducting electrolyte is situated between the electrodes separated by a thin, porous separator. During discharge, positive ions de-intercalate from the negative electrode, which can be made from different carbon material, then they pass through the porous membrane and intercalate into the positive electrode typically made of lithium metal oxides. Meanwhile, electrons move from the negative electrode to the positive electrode using an external connection. The flow of electrons and ions is reversed during the charging phase [9].

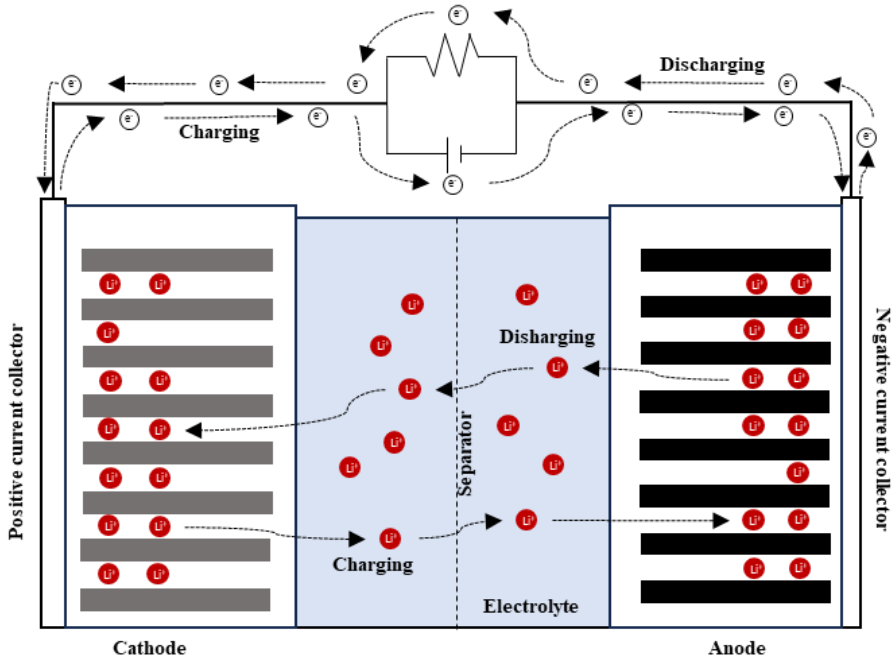

Figure 2: Schematic diagram of lithium-ion battery. CC By licence from ref [10]

Reaction at the anode:

$$LiMO_2 \rightleftarrows Li_{1-x}MO_2 + Li^+ + xe^-$$

Reaction at the cathode:

$$C + Li^+ + xe^- \rightleftarrows Li_xC$$

Overall:

$$LiMO_2 + C \rightleftarrows Li_{1-x}MO_2 + Li_xC$$

2.1.1.1 Anode

Generally, the most popular material for the anode is graphite because of the advantages it provides. Some of the factors that make graphite a suitable option include, its low cost, availability, and stability during lithium insertion and low thermal expansion during charging and discharging. Even then, the researchers are working on developing better materials and combination to improve the capacity and performance. For graphite the theoretically charge storage capacity is 372 [mAh/g] [11]. Some materials, such as silicon, aluminium, and antimony, can have higher theoretical capacity (4200 mAh/g for $Li_{22}Si_5$). Unlike graphite that intercalates lithium ions, these metals store lithium by forming an alloy with lithium [12] However, they experience more than 300-500% expansion and contraction during charging and discharging respec-

tively, leading to structural instability. To counter this drawback a blended model of the electrode can be studied where graphite can provide the structural stability [13]. Another interesting field of study could be carbon nanotube (CNT) as a prospective anode material. They can be used as free-standing electrodes because they are highly conductive. By using CNTs as free-standing electrodes, the need for additional current collectors can be omitted, which will increase the usable capacity. The fabrication of the electrodes might not require any binders, resulting in a lightweight component which could function at higher temperatures, since most binders are unstable at temperatures higher than 200 °C. Also, CNT has good electrical conductivity, 5×10^5 S/m for purified single walled carbon nanotubes (SWCNT). In addition, CNTs are very strong materials with high tensile strength (80 to 100 MPa) and Young's modulus (5-10 GPa) [14].

2.1.1.2 Cathode

Typically, cathodes of Li-ion batteries are generally made of metal oxides or phosphates able to intercalate Li^+ into their lattice, such as $LiMnO_2$, $LiCoO_2$, and $LiFePO_4$. However, their conductivity is poor compared to graphite or metals. This problem is minimized by using conductive additives such as carbon which are blended with finely powdered active material [11]. Meanwhile, ternary lithium batteries employing mixtures of Ni, Co, and Mn or Ni, Co, and Al are gaining popularity, as they are safer and cheaper than cobalt oxide based batteries without compromising the high energy density as with lithium iron phosphate batteries. Having three different metals (Mn, Ni, and Co) is making their structure and recycling more complex [15]. The choice of binder also affects the electrochemical performance along with other characteristics of the battery. Polyvinylidene difluoride (PVDF) is being used extensively as binder, as it has desired properties, for example, high adhesion to electrodes and current collectors and electrodes. Meanwhile, some studies are being conducted to find better alternatives, to minimize the toxicity and to reduce the cost of binder [16].

2.1.1.3 Electrolyte

Electrolytes can be categorized into two types: liquid electrolytes and semisolid or solid-state electrolytes. Liquid electrolytes are typically composed of lithium salt dissolved in organic carbonates. Popular lithium salts are $LiPF_6$, $LiBF_4$, lithium bis(oxalate)borate, and $LiN(CF_3SO_2)_2$, whereas ethylene carbonate, propylene carbonate, ethyl methyl carbonate, dimethyl carbonate and their mixtures are used as solvent. On the other hand, lithium-ion polymer batteries utilize

electrolytes of lithium salts dissolved in a solid matrix composed for instance from polyvinylidene fluoride, poly-ethylene oxide, and polyvinylidene fluoride hexafluoropropylene [11]. Apart from those salts and organic solvents, some additives can be added to improve battery efficiency, reversible capacity, and improved solid electrolyte interphase (SEI) formation which can ultimately help increase the lifetime and safety of battery [17]. Solid states electrolytes which include inorganic Li-ion conductors, polymer electrolytes, and organic-inorganic hybrid composites are becoming popular due to their lower risk of flammability and higher energy density. However, before it could be used commercially, some improvements would be required including, decrease grain boundary resistance at the interphase of electrolyte and electrodes, Li-ion transport into the bulk, and structural stability for long term usability [18].

2.1.1.4 *Separator*

The preliminary function of the separator was to restrict physical contact between the electrodes by letting the ions pass through the pores. However, recent advances in batteries and battery technologies are forcing separators to have additional functionality. For example, if the batteries which need to operate at high temperatures, the separators must withstand higher temperatures [19]. Separators can be categorized as microporous membranes, nonwoven-based, gel polymer electrolyte, and composite membranes [20]. Focus has been given to improving the most used membranes, which are polyolefins (polypropylene, and polyethylene) [21].

2.1.1.5 Current Collector

The transfer of electrons from the cell to the load or from the external source to the cell is facilitated by current collectors. Current collectors are required to have high conductivity, hence, metals, such as stainless steel, copper, aluminium, titanium, and nickel are utilized. Among them, aluminium and copper are prioritized [22], copper for the anode and aluminium for the cathode.

2.2 Necessity of Recycling

Substantial growth in lithium-ion battery production and use can have enormous effects on the environment, and human health. Several elements and chemicals are used in modern lithium-ion batteries, and some of them can be hazardous as confirmed by several studies. Fluorinated chemicals that are essential parts of both electrodes, acting as binders, are responsible for emitting persistent organic pollutants (POP). However, the magnitude of the risk posed by them is still not fully understood [23]. Another toxic element for human and aquatic creatures could be

vinylene carbonate used as an additive in electrolytes [24]. Also, Diethyl carbonate which is usually mixed with ethyl methyl carbonate comes with its drawbacks. Not only the solvent is flammable, but also, according to the European Chemical Agency (ECHA), it is also carcinogenic, and poses threats to the human reproductivity system [25]. Apart from the environmental issues, material availability has become a major concern, especially for metals such as lithium, cobalt, manganese, and nickel. In 2011, the ceramic industry was the highest consumer of lithium, consuming 30% of the total. Now 60% of the total consumption is associated with batteries. The demand for lithium is expected to reach 63 million tons by 2050 if the rate follows a similar trend. This will influence the cost of lithium, which can already be seen as the price of Li_2CO_3 rising 2.3 times in a span of 3 years (from 2015 to 2018) [7]. Correspondingly, the amount of cobalt usage has also increased, and the principal area of application is again rechargeable batteries. Over 50% of the total produced cobalt is being used in batteries, compared to only 21% in 2005 [26]. Considering the increasing global demand for the years 2030 and 2050 cobalt is assumed to be approaching near-critical level in terms of supply risks. This imposing a threat towards the clean energy policy´s short and long-term vision [27]. Recently, less cobalt containing batteries (NMC and NCA), and cobalt free batteries LFP are being manufactured. According to the British Geological Survey of 2018, 3%-4% of global nickel consumption was used in batteries. This share is expected to increase because of the advancements in battery technologies [28]. The high cost of nickel, cobalt, and copper, makes recycling economically feasible. However, manganese is cheaper, hence a cost-effective recycling method should be established [29]. Between 2013 and 2014 a total of 65,000 tons of lithium-ion batteries was produced only in Europe while only 9000 tons were recycled. The root cause could be the inefficient collection system and lack of cost-effective recycling facility [30]. Thus, an imminent solution to this problem is required to handle this large amount of waste.

2.3 Recycling Process

Recently, lithium-ion battery recycling has received great attention owing to its importance regarding financial and environmental aspects. Along with academic participants, several business organizations from all over the world, for example, ABT from the USA, Fortum from Finland, Northvolt from Norway, Guanghua from China, and Envirostream from Australia, have also shown interest. Currently, recovering lithium and cobalt has been in the focal point, while studies on recycling other metals such as nickel, manganese, and iron can also be seen [31]. Considering the complex structure of LIB, their recycling is not straightforward. Starting from collecting the used batteries to getting the usable products, the whole process involves

several steps. In a recent publication, Qiang Wei et al. described different stages of recycling batteries used in electric vehicles that include a second life use to utilize the remaining capacity for other less stressful applications, like, electrical energy storage for renewable energy, smart grid applications, and low-speed EVs, recycling of materials, and ending with recovery of valuable metals [32].

2.3.1 Second-Life Application

Once the battery loses 20% to 30% of its initial energy storage capacity, it is not possible to use it in electric vehicles since it will not give desired mileage and might cause issues regarding safety [33]. Echelon utilization (Figure 3) of retired lithium-ion batteries is considered beneficial since the lifespan of batteries can be increased while the cost of recycling can be reduced. Thus, the upfront cost of EVs can be controlled, and large-scale scrapping of the spent batteries will be minimized [32]. Conventionally, detecting battery performance deterioration is a cumbersome task. However, it is essential to sort them by assessing the internal resistance, residual life, side reactions, and remaining capacity to understand their current state as well as for safety purposes [34].

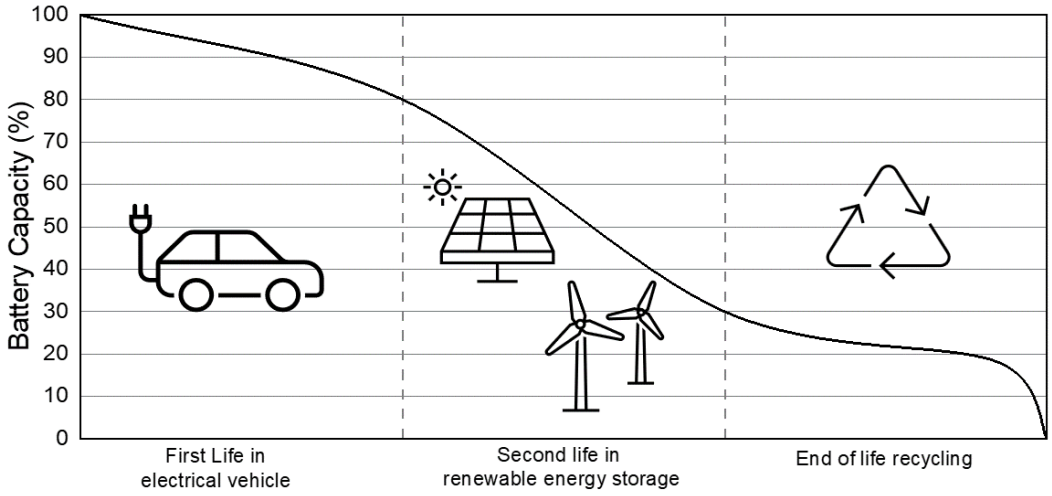

Figure 3: Application in different capacity ranges. Reproduced under CC BY licence from ref [35]

Traditionally, testing was done by fully charging and discharging each cell separately to determining the remaining utilization battery capacity, also named state of health. This method requires a long time and is not suitable for larger applications. Hence, methods aiming for faster and more scalable evaluation of the battery state of health have been developed and they could be categorized into model-driven and data-driven methods. One model named, Back Propagation Neural Network (BPNN), has shown higher accuracy for large-scale applications and its effectiveness in determining small-scale performance is also remarkable [36]. This BPNN machine learning algorithm provides the state of health of the battery by analysing the input data. Datasets can be external for example temperature, charging and discharging rates, and depth of discharge, and internal would be the physical and chemical properties of the LIB such as generation of solid electrolyte interphase (SEI), self-discharge, and decomposition of the anode [37]. After sorting, different groups of batteries can be used in different applications. Usually, batteries with higher internal resistance are used in the recycling process, where valuable materials are recovered [32].

2.3.2 Lithium-Ion Battery Recycling Steps

Since, lithium-ion batteries are made of various components (electrodes, current collectors, separator, electrolyte), and some of them are made of different materials, it makes their recycling a very difficult task. Hence, an effective, and efficient recycling method includes different steps (Figure 4).

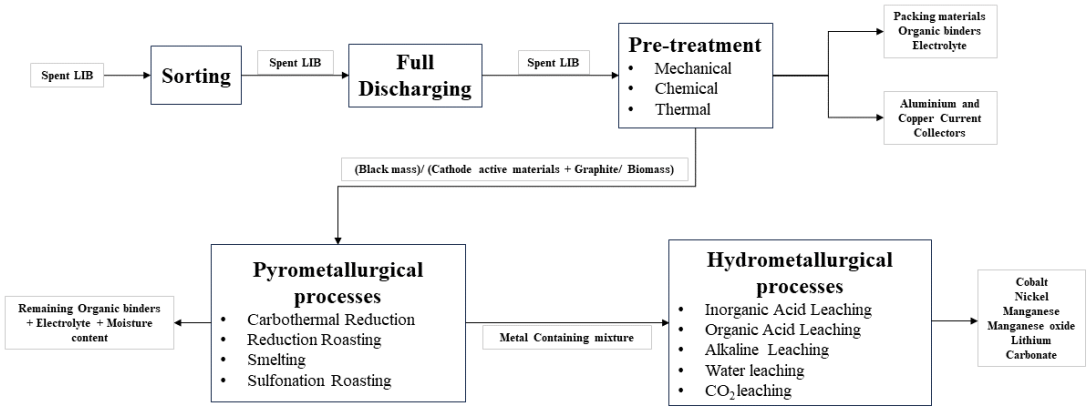

Figure 4: Simplified flow sheet of lithium-ion battery recycling process with combine pyrometallurgy and hydrometallurgy process.

2.3.2.1 Full Discharging

First, sorted batteries are fully discharged before performing any other operation, that might lead to some serious consequences. If dismantling is being done without fully discharging the battery, an uncontrolled flow of stored electric energy can be released, which would create overheating and, in the worst-case fire and explosion. A few techniques can be employed for discharging, such as discharging by solid electrical conductors, immersion in aquas solution, thermal deactivation, and cryogenic deactivation [38].

2.3.2.2 Pre-Treatment Methods

Treating recyclable materials would increase the effectiveness and efficiency of the recycling process. Different materials such as aluminium and copper used as current collectors must be removed at the beginning of the metal recovery process from the battery since it is easy to remove them by manually dismantling [39]. Also, they can influence the melting ability [40]. Different methods of pre-treatment have a distinct outcome in the recycling process, but they can also cause some environmental complications. Mechanical separation, dissolution treatment, and thermal treatment are commonly used pre-treatment processes.

2.3.2.2.1 Mechanical Treatment

One of the important aspects of mineral processing is to grind the substance so that it can be separated from the encapsulated form. Also, its importance has been noticed by the researchers, and they consider it to be one of the prerequisites for the hydrometallurgical lithium-ion battery treatment process [41]. Manual disassembly and different types of comminutions such as crushing, and particle size classification can be the part of mechanical treatment process [38].

2.3.2.2.2 Chemical Treatment

Organic solvents can weaken the adhesive properties, hence treating battery materials with substances such as N, N-dimethylformamide (DMF), N, N-dimethylacetamide (DMAC), N-methyl pyrrolidone (NMP), dimethylsulfoxide (DMSO) can increase the effectiveness and efficiency of recycling [42]. The cost of setting up equipment and organic compounds needs to be reduced before it can be used on an industrial scale [32]. Plastics and foils remaining in the black mass can be separated by using floatation techniques. The same process can also be used to recover graphite which is mostly overlooked as a valuable item during the recycling process from the mixture of anode and cathode [43].

2.3.2.2.3 Thermal Treatment

Organic materials and binders usually remained in the bulk even after mechanical treatment. Binding forces can be eliminated by applying heat, which would separate electrode material from foils which would increase the liberation efficiency and floatation of the electrode materials. Also, residual electrolytes can be separated by applying pyrolysis technology [44]. Although, organic additives and binders will be pyrolyzed at elevated temperatures, producing such an amount of heat would need extensive power. For example, aluminium and PVDF can be separated by heating at 650 °C and 400 °C respectively. However, it can release toxic gases such as fluoride derivatives through exhaust. Thermogravimetric analysis shows a mass loss at the initial stage at the temperature range of 450 °C to 550 °C, which could be the decomposition of PVDF [32,45]. Applying heat will separate fluoride from metal-containing substances by forming hydrogen fluoride [46]. Hence, some expensive arrangements would be needed to counter the negative effects on the environment.

Pre-treatment stages are employed to remove all the undesired substances such as F, Al, Cu, Si, and P etc. However, even after careful execution of the pre-processes, some traces of those impurities can be seen in black mass, which can affect the overall yielding efficiency of the metal recovery process [47]. For example, at high temperatures, recovered $LiCO_3$ breaks down into Li_2O and CO_2, but having F inside the system might cause LiF to form at 700 °C. Also, the incineration process at the same temperature might produce $Li_2SiO_3(LiF)_2$ [48].

2.3.2.3 Metal Extraction

Pre-treated materials are then recycled to extract valuable metals. Most of the metal elements are separated from batteries after passing through several treatments. At present, conversion of the metal to soluble substances is done in two ways, pyrometallurgy and hydrometallurgy. In some cases, these two processes are combined to effectively recover metals [49].

2.3.2.3.1 Pyrometallurgy

This is a process, where materials are smelted using high temperature in dry conditions. Normally, the pyrometallurgical method includes oxidation, reduction, chlorination, roasting, and slagging, yet sometimes liquid metals are extracted and separated from the unit [50]. Also, the furnace used in the pyrometallurgical process plays an important role in efficient recovery. The high contact area between the active material and reducing agent, homogenous heat supply, and a shorter passage for the volatile materials are some desirable properties of a furnace [51]. The

pyrometallurgical process is not as popular as hydrometallurgy among battery recycling industries. However, the hydrometallurgical process poses some environmental threats and further handling of those toxic wastes can become expensive, which makes the pyrometallurgical method for battery recycling an interesting research topic.

Studies suggest that reduction roasting can increase the efficiency of the following hydrometallurgical recycling process. Roasting temperature, retention time, and reducing agents such as lignite can affect the recovery rate. All these parameters have an optimal range and beyond that range, the effect is very negligible [52]. In one study, lithium carbonate, cobalt, and graphite were recovered by first applying oxygen-free roasting and then the products were separated from a solution by magnetic force. More than 90% graphite and 95% metals (Li, and Co) was recovered while roasting at 1000 ℃ in a Carbolite STF Tubular Furnace for 30 minutes [53]. Recent analysis from SEM and EDX substantiates the breakdown of the crystal structure of the cathode materials during thermal treatment [52]. The reduction of ternary cathodes can be achieved when the substances are heated over 650 ℃. At that temperature, initial materials decompose into Li_2CO_3, Ni, Co, and MnO. A large quantity of Li_2CO_3 is not achievable unless 10% of graphite is introduced in the heating process [54]. A laboratory scale recycling process experiment was conducted to evaluate the possibility of a large-scale application. The process was assumed to be energy efficient because only 1.08 MWh energy was consumed for every tonne of electrode material processing while recovering 100% of the metals. Hence, a pilot-scale experiment was being suggested before implementing large-scale operation [55]. During the pilot-scale experiment, EAF was used for the heating of the materials. However, more control and productivity are expected by using DC furnaces that are dedicated to smelt conduction in industrial operation [56].

Carbothermal reduction also has the potential for lithium recovery from spent lithium-ion batteries. Although lignite and carbon black are economically advantageous, the impurities present in them can be an obstacle [57]. Hence, recent researchers are focusing on using graphite from the spent anode. Utilizing spent anode graphite as a reducing agent would reduce the recycling steps, and energy consumption because separation of anode and cathode is not required, and environmental impact would also be less since they are often considered as waste [58]. In a study, where NMC was reduced using graphite from spent anode showed better results. Since anode graphite passes through several aging reactions, for example formation and decomposition of solid electrolyte interphase (SEI), and intercalation and deintercalation of lithium-ions, make some structural changes. As a result, better reactions can be occurred on both the surface

and inside the material [59]. However, the amount of graphite present in the spent anode can be higher than the required amount for stoichiometrically equivalent reactions [40]. Hence a separation technique could be introduced that uses the differences in surface wettability [60]. Studies suggested that $LiCoO_2$ can be decomposed at a temperature higher than 700 °C while the decomposition of solid Li_2O and Co_3O_4 might be possible in the range of 813 °C – 938 °C, further increase in the temperature would produce CoO [61]. Although higher temperature provides higher yielding, the metallic recovery rate decreases after a certain temperature. A possible reason for the phenomena could be the reoxidation of CoO and Co to Co_3O_4 [62]. Though increasing graphite dosage would have a positive impact on carbothermic reduction reaction, after a certain limit, the improvement would not be significant [63].

2.3.2.3.2 Hydrometallurgy

Hydrometallurgy is a wet process where some solution is used to treat metal-containing substances [50]. Metals from spent lithium-ion batteries can be dissolved into solution by a leaching process and, after that separated and purified [64]. Leaching process can be divided into three categories: acid, alkali, and bio [32]. Compared to the pyrometallurgical process, hydrometallurgy has some advantages, such as lesser energy demand, minimal release of gaseous pollutants, and higher purity of recovered metals [65].

Inorganic acids are very strong leaching agents. Sulfuric acid being one of the strongest acids has been used for hydrometallurgical lithium-ion battery recycling [66–68]. The recovery rate is enhanced with higher concentration. Similarly, increasing temperature, liquid-to-solid ratio, and leaching time can impact positively. Also, a reducing agent such as F_2S might be necessary for decomposing the solid pre-treated materials [66]. Other strong acids, for example, HCl, HNO_3, and H_3PO_4 have also been examined as leaching agents [69]. Leaching with HCl would produce metal chlorides and chlorine in the product stream. Cl can be considered toxic waste. So, instead of using HCl, in some cases, H_2O_2 was added as a reducing agent [69].

Among the compounds, Li_2CO_3 can be leached using water at room temperature because increasing the temperature would decrease the solubility of lithium carbonate [70]. Ammonium solvent can be used to leach other elements with the assistance of oxygen [71]. Manganese exhibits good efficiency while low concentration of ammonium citrate was used but Co and Ni needed to be oxidized first before they could react with ammonia solvent. Similar effects were realized when ethylenediamine was used as a leaching agent. Increasing leaching time and temperature ensures higher efficiency until a certain point [70]. In addition to water, CO_2 leaching

has also been studied to recover lithium. However, CO_2 concentration does not have a significant impact on the recovery [54]. Another important thing to notice is that the fluoride should be removed from the materials before leaching with supercritical CO_2 [72].

Using organic acids can mitigate the risks associated with inorganic acids such as soil pollution, water pollution, health issues of operators, releasing toxic gases (chlorine, sulphur, and nitrogen oxides) [73]. However, organic acid has low acidity, and solubility in water. Hence leaching efficiency is also very low [74]. Adding a reducing agent has a positive impact on the process, as Co_2^+ is more soluble in water than Co_3^+. Also, the H_2O_2 reducing agent can loosen the strong bond of $LiCoO_2$ [75]. Increasing the concentration of the acid provides more H^+ which improves the efficiency of the leaching process [74]. Citric acid has chelating properties which make it suitable as a leaching agent [75]. That chelating property also makes the precipitation process tedious and chemical-intensive [76]. Some benefits of using this weak organic acid, for example, cost effectivity, less industrial arrangements, and reduced toxic emissions drawn the attention of the researchers [77].

Coordination-enhanced leaching with inorganic acid and organic reductant can solve the problem of slow leaching kinetics. The inorganic acid-organic reductant system creates a reducing atmosphere with higher proton availability which improves the kinetics of the reaction [78]. Strong acids H_2SO_4 and HCl were paired with L-ascorbic and were examined to recover metals from spent batteries. Although both systems show identical characteristics, HCl-L-ascorbic is kinetically faster [79]. On the other hand, ascorbic acid has better leaching properties than HCl because of its ability to act as a reducing agent as well as an acid [80].

Even though hydrometallurgy processes are currently in extensive use, the slow reaction kinetics leads to longer recovery time making it difficult to be used in industrial applications. Also, large volume processing of materials can be difficult since a huge quantity of leaching agents as well as reducing agents would be needed. On the other hand, pyrometallurgy looks more suitable for large-scale industrial applications, yet the recovery rate and purity of the metals should be improved. Hence, a combination of both procedures can be employed.

Leaching with ascorbic acid was studied by Lie et al. inside a closed vessel under microwave heating. Higher temperatures increased the leaching efficiency and shortened the time required for recovery [81]. Microwave can speed up the heating process by the collision of induced ions in the leaching solution. The process of intensified microwave-assisted extraction has several benefits over conventional leaching methods. Shorter yielding time, higher yield, and smaller

amounts of solvent are some of the advantages [82]. Exposing mixed electrode materials to microwaves makes the valuable metal recovery easier since cathode materials get reduced during the process. The active materials get heated so rapidly that in 12 minutes the temperature rises to 831 ℃ while losing 30.2% of mass. From the study, they could spot the phases of Co, CoO, MnO, Li_2CO_3, Ni, Co_3O_4, and C, which suggests the breakdown of Li and O [83].

2.3.3 Industrial-Scale Recycling

Industrial-scale recycling of retired lithium-ion batteries requires a combination of more than one pre-treatment method. Recupyl Valibat recovered Li_2CO_3, Li_3PO_4, $Co(OH)_2$ or elemental Co by recycling cobalt-containing cathode material with $LiFePO_4$. First, the shearing of lithium-ion batteries was done in an inert atmosphere, then sheared substances were milled and finally classified based on size [30]. Another large-scale example can be found in JX Nippon Milling and Metals. First, the electrolyte was incinerated by burning. The next step was mechanical treatment followed by classification. Cathode material having Mn, Co or Ni was fed into the furnace. Nickel and cobalt were recovered as metals whereas manganese and lithium were recovered as carbonate compounds [84]. A relatively relaxed approach was taken by Sumitomo where only sorting and dismantling methods were applied. The reason behind that could be lesser complex cathodes that contain only cobalt. Recovery products from the process are, Steel and Cu from mechanical separation [85]. An advanced recycling technique was adopted by Duesenfeldt. They begin the process by recovering residual energy from batteries to be used in the recycling plant or fed into the grid. After that, disassembling of the discharge batteries is done. Duesenfeldt mechanical process then recovers electrolyte, copper, aluminium, and black mass. Finally, $CoSO_4$, $NiSO_4$, $MnSO_4$, Li_2CO_3, and the remaining graphite can be recovered with the hydrometallurgical recycling process of the black mass [86]. Onto Technology is also successful in terms of recovery rate where lithium was recovered at 99% purified form along with other metals and grapite. After recovering the material, they could also fabricate cell cathode powders from recovered materials [30]. Fortum, a Finland-based company, recycles retired lithium-ion batteries where the mechanical process is employed to recover 80% of the components and 95% of the total valuable metals remaining in black mass is being recycled through the hydrometallurgical process [87]. Swedish organisation, Stena got funding worth SEK 70.7 million for building recycling facilities. They will have a high amount, nearly 10000 tons of initial recycling material handling capacity with a 95% recovering rate [88]. Technology Minerals has got the approval to open a recycling plant in the UK. A successful implementation of the project would make the country's first battery recycling plant. According

to the Environmental Agency (EA) permit, 8300 tons per year recycling capacity is allowed. However, they want to increase its capacity to 22000 tons per year after the completion of the construction and gradually to 50000 tons per year by constructing five more plants [89].

2.3.4 Microwave Heating

Microwave energy is nonionizing electromagnetic radiation having wavelengths of 1 mm to 1 m [90]. The typical frequency ranges can be categorised as ultra-high (300 MHz to 3 GHz), super high (3 GHz to 30 GHz), and extremely high (30 GHz to 300 GHz) frequencies [91]. Microwaves have a diverse set of uses, such as power transmission, radar, telecommunication, medical sectors, and some other scientific applications. Therefore, it is important to have unique frequencies and wavelengths for domestic and industrial microwave heating, so that they do not interfere with other applications. The designed frequencies are 900 MHz and 2.4 GHz corresponding to 33.3 cm and 12.2 cm wavelengths respectively [92]. Microwave can be generated by using electrical energy with relatively good efficiency. An efficiency of 85% can be achieved for the radiation of 900 MHz while 2.4 GHz has a 50% conversion efficiency [93]. Along with the efficient conversion, heating with a microwave can be cost-effective as well as environmentally friendly, if renewable sources, such as wind and solar power are used.

Microwave electromagnetic radiation consists of two electric and magnetic fields oscillating and propagating through space (Figure - 5). Some materials can absorb this radiation, they are classified as dielectrics. Other materials can either reflect the radiation or the microwave can pass through them without being absorbed. The materials that are transparent to microwaves can be considered insulators which can be used to hold and support the substances to be heated. Reflective materials are used to guide the waves and act as a conductor [94]. Due to the oscillating electromagnetic field, absorption of microwaves by the dielectrics would induce rotational and translational types of molecular motion by species, known as dipolar momentum. An exothermic effect of heating is generated by breaking and creating new weak intermolecular bonds because of the dipolar momentum [93].

There is a significant difference between the conventional and microwave modes of heating. Since. microwave is absorbed by the materials, the core is heated first, followed by the outer surface. On the contrary, by a conventional method, the outer surface is heated primarily, followed by heat transfer inside the material by conduction, convection, or radiation. A noticeable temperature gradient could be visible where the inside temperature would be less than that of

the outside temperature of the material subjected to conventional heating. Rapid, volumetric, noncontracting, and efficient heating can be done by microwave irradiation [95].

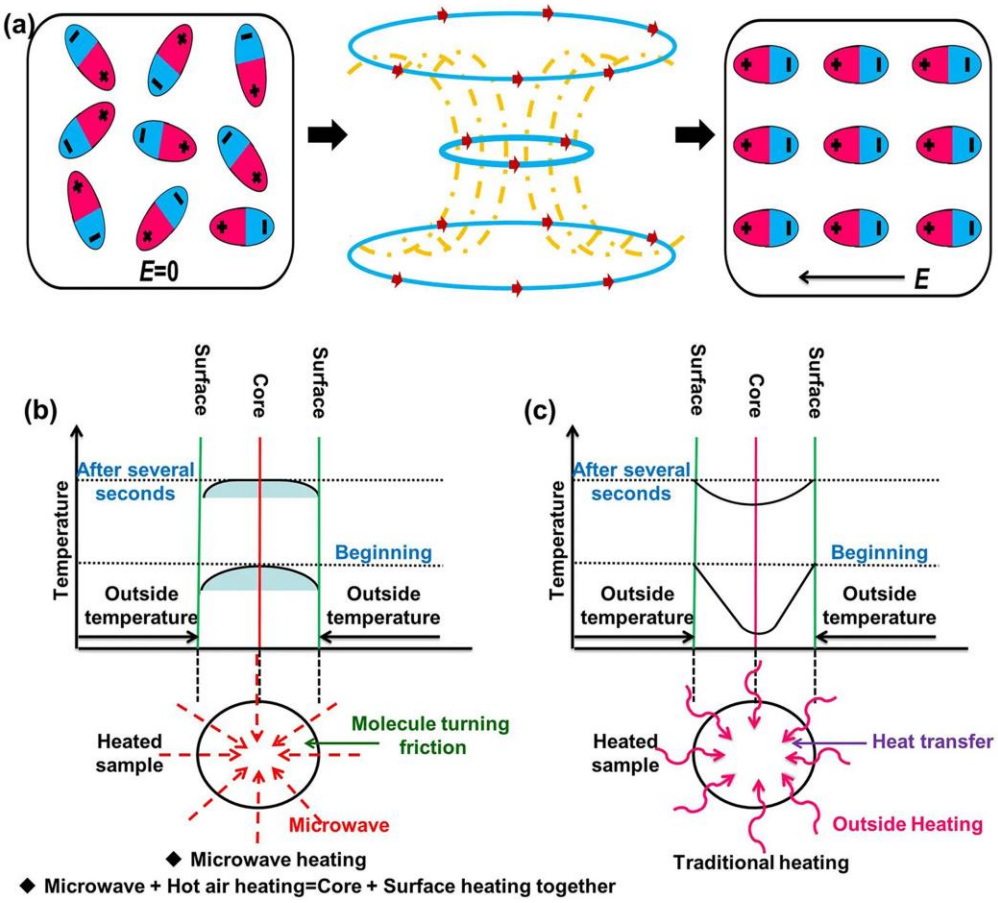

Figure 5: a) Effect of electromagnetic radiation on the dipolar materials. b) Microwave heating profile and transfer direction. c) Conventional heating profile and transfer direction. Reprinted from Renewable and Sustainable Energy Reviews, Volume No. 124, Sasi Kumar N, Denys Grekov, Pascaline Pré, Microwave mode of heating in the preparation of porous carbon materials for adsorption and energy storage applications – An overview, Page no. 3, Copyright (2020), with permission from Elsevier.

In the field of oscillating microwaves, dipoles of the sample will align themselves in the electric field. The alignment will be rotated which will create friction between the atoms leading to heat generation. This effect can be named as dipolar polarization. Also, charged particles or ions oscillate with the oscillation of microwaves making them collide with neighbouring atoms or molecules. The heat generated by this phenomenon can be referred to as ionic conduction. The ability of a material to be heated by microwave radiation can be estimated by loss tangent which is denoted by tan δ and depends on dielectric loss (ε′′) that is a measure of the material's ability or efficiency to convert microwave into heat, dielectric constant (ε′) determines material's ability to be polarized, magnetic loss (μ''), and magnetic permeability (μ'), as show in equation [96]. So, materials having less loss tangent values indicate that they cannot absorb microwave

radiation easily. However, some additives, such as catalysts, ionic and liquids, can be added to those mediums to heat them under microwave exposure [97].

$$tan\,\delta = \frac{\varepsilon''\mu' - \varepsilon'\mu''}{\varepsilon'\mu' + \varepsilon''\mu''} \quad (1)$$

We can see that the amount of produced heat is dependent on both the dielectric and magnetic properties of a material. Hence, heat generated in magnetic materials would be greater than in non-magnetic materials because the dipole might get coupled with the magnetic field to provide additional heat. Loss tangent for materials having minimal magnetism could be expressed by equation [98].

$$tan\,\delta = \frac{\varepsilon''}{\varepsilon'} \quad (2)$$

An advantage of microwave heating is the uniform distribution of heat throughout the material which can be approximated by two parameters: absorbed power, and depth of penetration. The material's internal electric field and magnetic conductivity influence the amount of absorbed power [99]. Similarly, to loss tangent, the depth of penetration also relies on the electric and magnetic properties of the material [98]. The microwave absorption ability of a material can be estimated by measuring the microwave penetration depth. It also indicates the uniformity of the heating which depends on the dielectric properties of the substance as well as the microwave frequency. If the depth of penetration is higher than the particle size, there is a positive response towards microwave exposure [100]. Penetration depth in metallic powders with high surface area is sufficient for volumetric heating [101]. In the case of non-metallic materials loss tangent and depth of penetration varies with temperature. The increasing temperature would increase the loss tangent while the complete opposite happens regarding depth of penetration [96].

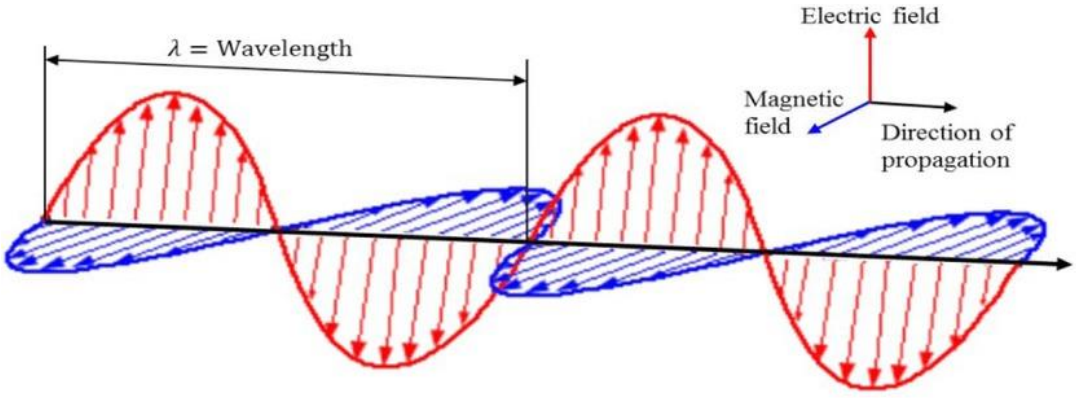

Figure 6: Electromagnetic wave propagation. Reused under CC BY-NC-ND 4.0 from ref [102].

2.3.4.1 Microwave for Material Processing

The utilization of microwave heating has been studied in many materials processing techniques. Deposition of 3d polymeric graphene foam (PGF) with Mn_3O_4 nanocrystals was assessed by Liu et al., using microwave shock to enable higher heating and cooling rates. The synthesized materials have higher Mn_3O_4/graphene while processing time can be only 1.2 seconds at a high temperature of 1549 K [103]. An attempt to regenerate activated carbon was made using microwave heating. Irradiation from microwaves can preserve the pore structure, adsorption capacity, and original active sites in activated carbon. Hence, the efficiency of regeneration using microwave is higher than that with conventional heating [104]. Since the cost of activated carbons is huge, the regeneration of them would reduce the expenses in their applications of wastewater treatment, metal recovery, and air pollution control [105]. Porous carbon materials are widely used as adsorbents in environmental applications, and anode in storage devices can also be prepared using microwave heating. Microwaves can be an alternative source which will generate very fast heating with renewable energy sources. Also, the production time can be reduced. Activated carbon materials that are synthesized by microwave irradiation exhibit higher specific surface area. Hence, they possess higher adsorption, faradic efficiency, and catalytic ability [106]. The use of microwave heating was examined by Kosai et al. in the recycling of obsolete alkaline batteries. Recovery of ZnO and MnO from the Mn_3O_4, ZnO, and graphite was executed with microwave heating. In their study, two times the stoichiometric amount of carbon was taken where 92 to 97% zinc was recovered [107]. The utilization of microwaves in synthesizing manganese-based cathodes has been studied. Research showed that microwave irradiation can significantly improve the physiochemical properties of the cathodes with a lesser amount of power and within a short time. Microwave-assisted synthesis would reduce the secondary impurities and one extra lithium can be inserted in per formula unit. Also, the particle size that can impact the electrochemical performance of the battery, is reduced in cathodes processed with microwave, resulting in better performance [96].

Although the value of graphite in the spent anode is overlooked, recovering that would be economically beneficial and better for environmental pollution control. Additionally, several studies have shown the use of anode graphite as a reducing agent in pyrometallurgical process [59,83]. The regeneration of graphite can also be done by microwave processing. Organic binders and electrolytes remaining in the anode would volatilize and lithium ions become Li_2CO_3 under high heat from microwave exposure in a brief time. Microwave radiation reduces a significant amount of fluorine impurities in the graphite, meanwhile, regenerated graphite shows

commending performance [108]. Regenerated graphite exhibited higher specific capacity than that of fresh commercially available graphite, this was explained by enlarged interlayer distances of the recycled graphite as well as removal of both organic and inorganic impurities, that were blocking the insertion of lithium-ions. The characteristics and performance of the regenerated graphite depend on exposure time as well, where exposing longer might not be good for the products [109].

2.3.4.2 Recovery of Metals from Spent Lithium-ion Battery Using Microwave

Microwave technology is being researched to understand its applicability in battery materials recycling. The performance of the recovery process depends on the absorbability of the microwave radiation by the substance. Absorbing property can be dependent on materials' apparent density, temperature, and carbon dosage. Increasing the apparent density would decrease the gap between the particles that were filled with air having inferior dielectric properties. So, with higher apparent density, microwave radiation can be absorbed better. However, with very high apparent density, the effective heating area might get reduced because of penetration of the radiation occurring easily, reducing the thermal conversion efficiency. Raising temperature also increases the microwave absorbing capacity. According to a study by Zhao et al., the whole process can be divided into sections. First, the raw material loses weight gradually till 450 ℃ because of the evaporation of the water. Even though the evaporation happens, the transformation of amorphous MnO_2 to γ- MnO_2 promotes absorption. Then in the range of 450 ℃ to 650 ℃, due to the volatilization of the polar molecules, less absorbing properties were seen. Above 650 ℃, as the carbothermal reaction progressed the dielectric properties increased, which suggests that microwave heating can promote carbothermal reduction reaction. The amount of graphite does not have any significant influence until the start of reduction reactions. The optimal percentage of graphite was estimated to be 12% to 18%. The improvement in the absorbing properties after that range is not distinguishable [110]. Measuring the temperature of different components placed inside the microwave can be used to understand the microwave absorption of different materials. The factors that determine the attained temperature of the active materials from under microwave radiation are their dielectric properties, susceptibility, and polarizability [111]. The recovery is also dependent on a reduction reaction, so reducing agents can influence the efficiency of the whole process. Thus, a comparison of different reductants in terms of reducibility would be necessary. For example, the reduction of cathode-active materials from LCO and a mixture of LCO, LMO, and LMNO were studied using char-

coal and graphite from the anode. In both cases, graphite performed better than the charcoal[111]. Lin et al. measured the dielectric properties of cathode stripped from LMO batteries and mixed with moso bamboo as a reducing agent that helped the reduction process to recover MnO. In the beginning, relative dielectric properties increased. Then, when the moisture content on the surface of the cathode material was evaporated, dielectric properties were reduced. After that, a gradual increase in the value can be seen. Finally, at 900 ℃, new materials, such as Mn and Li, started to form which made a rapid change in the relative dielectric level. However, the addition of biomass decreased the absorption ability of the mixture. The reason could be the weak dielectric properties of the biomass and 12% of biomass was recommended [112]. Pinder et al. demonstrated a time-temperature plot in their work. There was a significant difference between the attained temperature of cathode active materials and silicon carbide susceptor or crucible which means cathode active materials are good microwave absorbers [113].

Since, there are several types of batteries depending on cathodes, a sorting pre-treatment stage should be employed in the hydrometallurgical recycling process because specific materials might need to be leached with specific leaching agents and conditions. However, sorting spent batteries accordingly would be time and energy consuming. A general process to recycle all types of batteries can make large-scale recycling easier and more profitable. In a study conducted by Fahimi et al., all kinds of mixed batteries were processed by microwave heating, followed by leaching with L-Malic acid. A hundred times more power would have been needed if conventional heating arrangements were used instead of microwaves [114]. Theoretical feasibility was checked by Fu et al. before conducting experiments. They calculated the Gibbs free energy for the transition metals in the roasting process, using HSC Chemistry 6.0 software. Reduction of Co_3O_4 to CoO and Mn_2O_3 to MnO was possible at room temperature. Further increasing the temperature would enhance the process, because the value of Gibbs free energy will decrease if temperature is increased. Raising the temperature would also be better to produce Ni and Co from NiO and CoO respectively using graphite as a reductant, however, it is only possible with a temperature higher than 450 ℃. Formation of Co from CoO using CO would not be possible because Gibbs free energy remains positive and further increases with increasing temperature. For the same reason, higher temperature would not necessarily increase Li_2CO_3 production. However, under the optimized microwave condition, transition metals transformed into lower valance states from higher valence states. Also, microwave reduction time has a positive impact on leaching efficiency. Graphite absorbs the radiation and temperature increases uniformly. However, different metals in the cathode have different dielectric

properties which means different parts of the heterogeneous cathode would have different thermal effects (Figure 7). Due to that variance inside the structure, thermal stress would be generated, and material would crack from the inside. Hence, higher yield is possible with lower power when using a microwave, compared to the traditional acid leaching method [115].

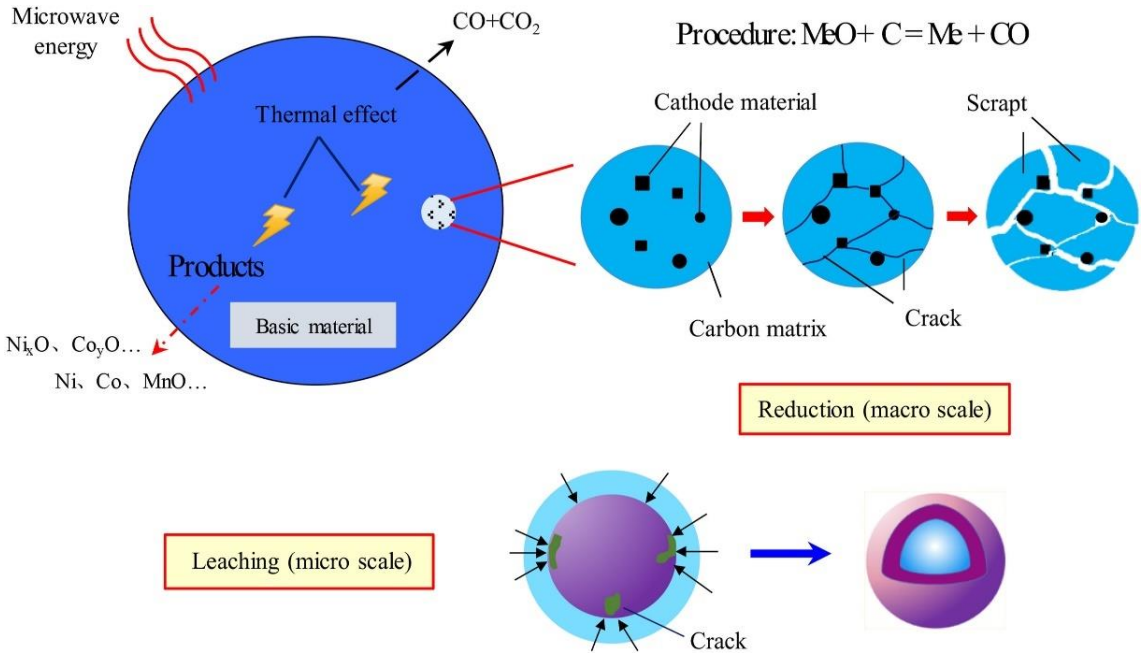

Figure 7: Mechanism of microwave assisted leaching of black mass from lithium-ion battery. Reprinted from Journal of Alloys and Compounds, Volume No. 832, Yuanpeng Fu, Yaqun He, Yong Yang, Lili Qu, Jinlong Li, Rui Zhou, Microwave reduction enhanced leaching of valuable metals from spent lithium-ion batteries, Page no. 10, Copyright (2020), with permission from Elsevier.

3 Methods

3.1 Materials

3.1.1 Materials By-Product

Raw materials for this experiment were black mass from spent lithium-ion batteries. Several pretreatments (Figure 8) were done on the sample before we could process them with microwave. Pretreated samples were then characterized to quantify their chemical composition. Carbon content was found to be 33 wt.% analysed via CHNS analyser. The quantity of other elements was measured by using ICP-OES (Table 1). Among the valuable metals, the presence of nickel is the highest, and amount of Li, and Co were similar, while amount of manganese is almost half of the amount of Co or Li. The traces of copper and aluminium can also be found that might have been remained even after the microwave assisted acid leaching pre-treatment process. Plenty of other materials were also present in the black mass in small quantities.

Table 1. The composition of black mass attained from microwave microwave-assisted acid leaching pre-treatment process was determined through ICP-OES.

Element	Amount	Element	Amount
Aluminium (Al)	9.06 (mg/g)	Nickel (Ni)	272.11 (mg/g)
Calcium	0.11 (mg/g)	Phosphorus (P)	3.92 (mg/g)
Cobalt	38.54 (mg/g)	Silicon (Si)	0.18 (mg/g)
Chromium (Cr)	0.01 (mg/g)	Titanium (Ti)	0.01 (mg/g)
Copper (Cu)	23.47 (mg/g)	Zinc (Zn)	1.11 (mg/g)
Iron (Fe)	0.15 (mg/g)	Zirconium (Zr)	0.91 (mg/g)
Potassium (K)	0.07 (mg/g)	Barium (Ba)	0.00785 (mg/l)
Lithium (Li)	38.93 (mg/g)	Cerium (Ce)	<0.007 (mg/g)
Magnesium (Mg)	0.03 (mg/g)	Neodymium (Nd)	<0.002 (mg/g)
Manganese (Mn)	15.55 (mg/g)	Palladium (Pd)	<0.004 (mg/g)
Sodium (Na)	0.97 (mg/g)	Strontium (Sr)	0.00259 (mg/l)

3.1.2 Material Preparation

First, the material was dried and divided into several representative samples. Before applying thermal treatment using microwave radiation as well as after the treatment, the raw materials were characterized using several techniques such as XRD, SEM-EDX, and ICP-OES.

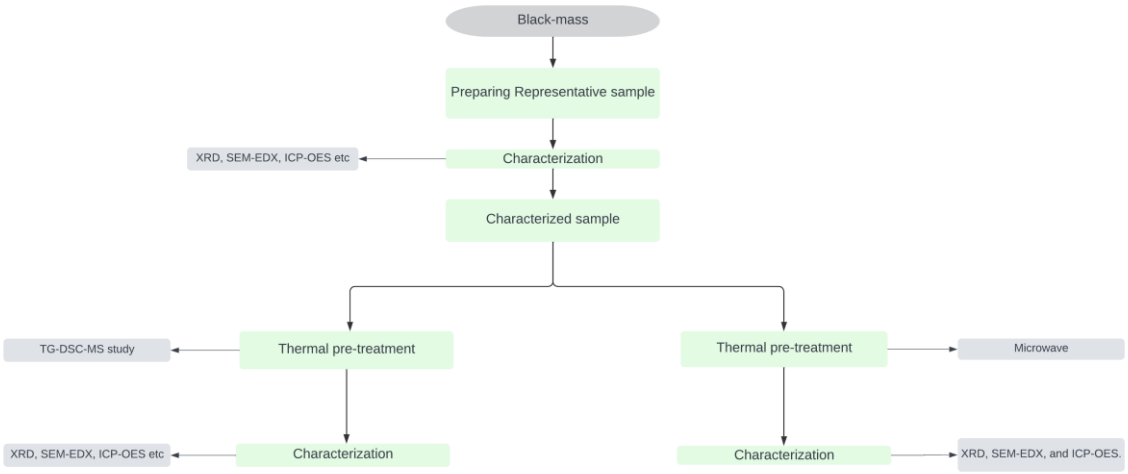

Figure 8: Pre-treatment flowsheet of material preparation.

After collecting some representative samples, characterization was done. After that, thermal behaviour was determined using the TGA-DSC-MS technique followed by sample characterization. Then a thermal treatment with conventional heating took place. Finally, the black mass sample (Figure 9) for microwave processes was obtained. Another characterisation stage was included after the process to determine the chemical composition, morphology, and crystal phases of the sample.

Figure 9: Black mass attained after the pre-processing stage.

3.2 Analysis Techniques

3.2.1 X-Ray Diffraction Analysis (XRD)

X-ray diffraction (XRD) is one of the most common techniques to determine the composition and crystal structure of any material. It can be used to determine the structure of the atoms within the sample when the crystal size is large, for example, macromolecules and inorganic

materials. Alternatively, with the small crystals, phase purity, crystallinity, and sample composition can be determined. The wavelength of X-ray beams is similar in size to the spacing between the atoms. So, the angle of diffraction would be affected by this spacing. Sending x-ray beams through the sample would make them bounce off of the atom when they hit them which would change their direction at a different angle known as diffraction angle. Two beams of similar wavelengths create constructive interference and send a larger signal for a specific angle of diffraction. Bragg´s law is used to calculate the distance between two atomic planes which determines the crystallinity, and composition [116]. One problem with this characterisation technique is amorphous materials cannot be observed by XRD. For this tool to be useful, the sample needs to be crystalline.

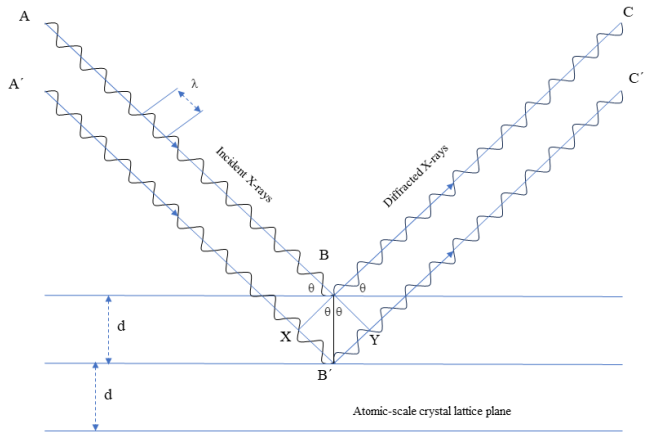

Figure 10: Visual representation of Brag's law. Reproduced under CC By 4.0 from ref [117].

Brag´s law (Figure 10) describes the relationship among the wavelength (λ) of the incident rays (ABC and A´B´C´), the distance between the crystal lattice plane of the atoms (d), and the angle of incidence (θ), where n is an integer number. Here, the incident angle (θ) is equal to the reflected angle. Also, XB´ and B´Y are equal.

So, $n\lambda = 2d \sin\theta$, which is known as the Brag's law. If the distance between the two paths ABC and A´B´C´ is by an integer number of wavelengths (λ), then constructive interference will be exhibited by the diffracted x-rays [118].

Preparation of the sample for XRD analysis begins with a grinding process where Agate Mortar is used to ground the sample. Then, an appropriate amount of sample was mounted on a flat glass sample holder (Figure 11).

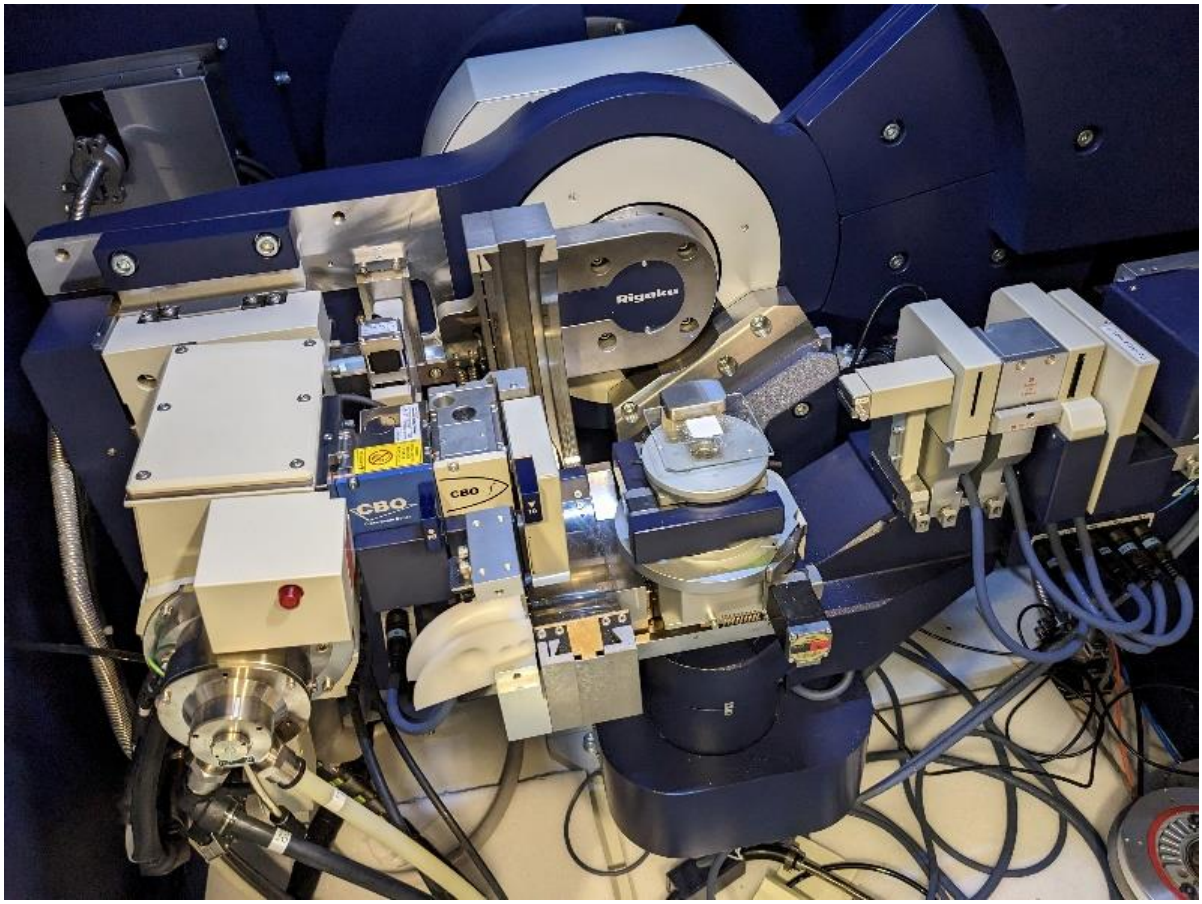

Figure 11: Sample rested onto the glass sample holder for analysis.

XRD analysis was performed with Rigaku SmartLab 9 kW. The crystalline phase identification of the sample was done in the scan range of 2θ from = 5° to 130°, with the step width of 0.02°. Scanning of the samples was done at 40 kV and 135 mA conditions. Phase identification from the diffraction patterns was done using the Rigaku integrated X-ray powder diffraction software PDXL 2.6 with the help of the ICDD PDF 4 database.

Figure 12: Rigaku SmartLab 9 kW XRD machine.

3.2.2 ICP-OES (Pre-treatment: Microwave-Assisted Acid Digestion)

Determining the quantity of different elements in the black mass sample was done using the Inductively Coupled Plasma Optical Emission Spectroscopy (ICP-OES) technique which was carried out at the Sustainable Chemistry unit at the University of Oulu. The general principle behind this method is that according to Bohr´s atomic model [119], electrons can move from one energy level to another when atoms absorb or release energy. In ICP-OES an argon plasma is used to supply the energy typically at 1000 K and the released energy is in the form of light. The wavelength of the emitted light depends on the type of atoms and the movements of their electrons within the energy levels. The quantity of the atoms or ions in transition decides the amount of light released at each wavelength. The concentration of each element can be calculated from the emitted light at each wavelength. A calibration curve needs to be generated by using a solution containing the same element of an amount which is known beforehand. That curve helps identify the concentration of elements by determining the relationship between the intensity of emitted light at a specific wavelength. A nebulizer is used to spray the solution into

the spray chamber as fine aerosol where a stream of argon gas is used. Larger droplets are passed through the drain and removed from the chamber while fine particles go towards the plasma torch. Then another steam of argon gas carries the aerosol of the sample up the centre of the plasma torch. The heat of the plasma torch evaporates the aerosol, then breaks the molecules into atoms and ions, and finally excites the electrons in the atoms and ions that move them to a higher energy level. A radio frequency (RF) generator supplies the energy to the plasma. Controlling the radiofrequency would modulate the energy level of plasma. A lower concentrated solution would need to be moved slower while the supply power is kept at a high level so that all the atoms can emit light and be analysed. Mirrors and other optical components direct the lights into an optical spectrometer which is used to separate the lights similarly as a prism. After that, a detector measures the separated lights of specific wavelengths [120].

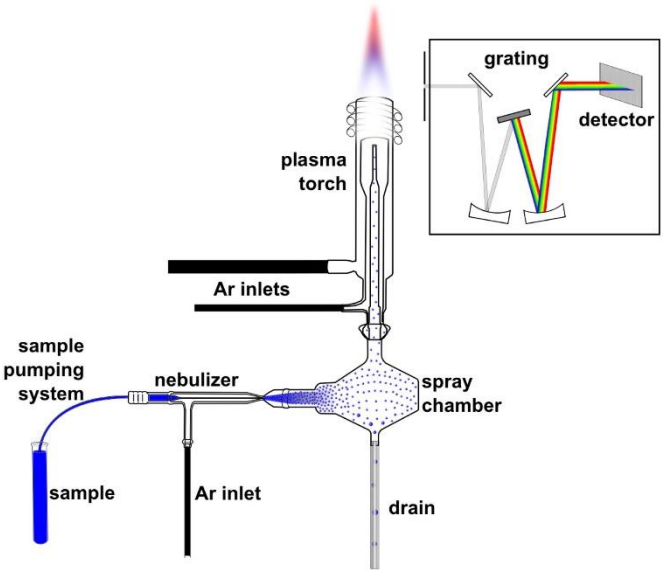

Figure 13: ICP-OES instrumental setup. Reprinted from Cement and Concrete Research, Volume No. 92, Francesco Caruso, Sara Mantellato, Marta Palacios, Robert J. Flatt, ICP-OES method for the characterization of cement pore solutions and their modification by polycarboxylate-based superplasticizers, Page no. 53, Copyright (2017), with permission from Elsevier.

Agilent 5110 VDV (Agilent Technologies, USA) was used with an HF-resistant component for ICP-OES measurements. Elements that were analysed include Al (237.312 nm (NG, ash), 396.152 nm (Slags)), Ca (315.887 nm), Cr (284.325 nm), Cu (324.754 nm), Fe (234.350 nm), K (769.897 nm), Mg (383.829 nm), Mn (293.931 nm), Mo (202.032 nm), Na (256.592 nm), P (213.618 nm), Si (288.158 nm), Ti (334.941 nm), V (292.401 nm), Zn (213.857 nm). Also, the machine was externally calibrated using a matrix-matching standard solution [121].

3.2.3 Scanning Electron Microscopy Coupled with Energy Dispersive X-Ray Spectroscopy (SEM-EDX)

Scanning Electron Microscopy (SEM) equipped with energy-dispersive X-ray spectroscopy (EDX) was also used to determine the phases, chemical composition, and elemental mapping. Minimal sample preparation time, fast data acquisition process, and convenient user interface make SEM one of the most widely used tools in the field of solid material characterisation [122]. However, detecting light elements, in our case lithium is practically impossible. Therefore, the analysis becomes a little cumbersome because one of the key elements that we are analysing is lithium. The main components of an SEM are an electron gun, electron optical system, sample holder, vacuum system, secondary electron detector, image display system, and operating system. An electron gun produces a stable electron beam with a high current as a thermionic emission. The produced energy should be adjustable while maintaining negligible energy dispersion and making small-sized spots. Although there are different types of electron guns available, advanced new SEM contains field emission electron guns for higher resolution. The Electron beam´s diameter is controlled by the magnetic lenses. Magnetic lenses' focal points can be altered by changing the intensity of the current passing through the electric wires. To produce a compact electron beam, double-stage magnetic lenses are placed below the electron gun that serves as both a condenser lens and an objective lens. A metallic aperture plate is placed between two lenses to block the maximum electron beam, allowing a small part to reach the objective lens. Objective lenses are made with careful consideration as their performance decides the effectiveness of the whole scanning operation. They control the ultimate diameter of the electron beam and their focus on the sample (Figure 14). A sample holder is used to hold the sample inside the specimen stage. Apart from moving in three directions, the specimen can be tilted as well as rotated according to the need. A super high level of vacuum (10^{-4} to 10^{-3} Pa.) is required inside the chamber to protect the equipment from contamination and electron beam from scattering. The electrons that are emitted from the sample surface are detected by the detector, after amplification they can be viewed from the display unit and can be saved as images [123].

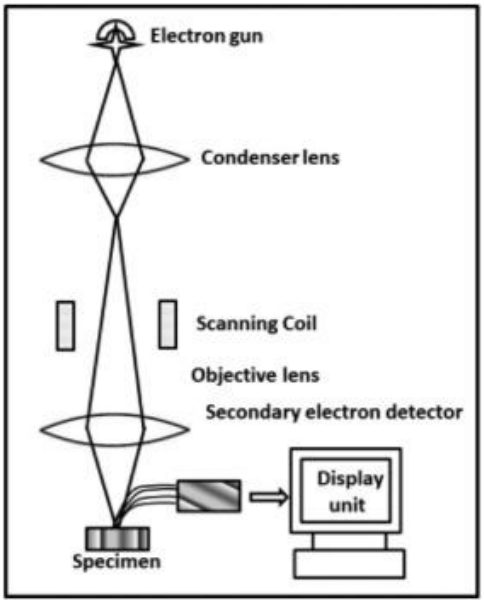

Figure 14: Schematical representation of scanning electron microscopy (SEM) working method. Reprinted from The Textile Institute Book Series, Volume of Characterisation of Polymers and Fibres, Mukesh Kumar Singh, Annika Singh, Chapter 17: Scanning electron microscope, Page no. 389, Copyright (2022), with permission from Elsevier.

Emitted electrons from the electron gun carry a significant amount of kinetic energy. Various kinds of signals are produced when they interact with the sample (Figure 15) which reveals information about the sample.

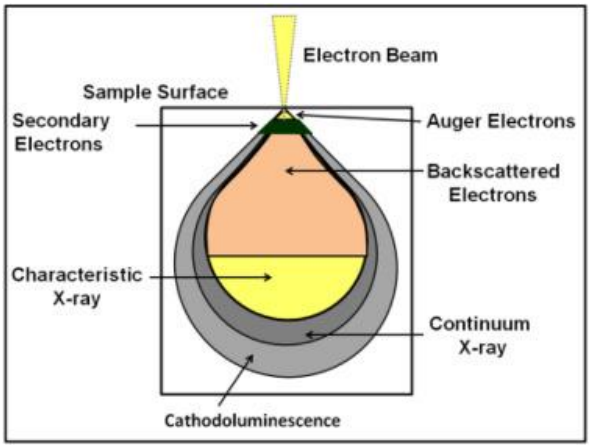

Figure 15: Different signals emitting from the sample. Reprinted from The Textile Institute Book Series, Volume of Characterisation of Polymers and Fibres, Mukesh Kumar Singh, Annika Singh, Chapter 17: Scanning electron microscope, Page no. 402, Copyright (2022), with permission from Elsevier.

The image of the sample is mainly formed by using with the secondary electrons and backscattered electrons. The former is responsible for showing the morphology and topography and the later illustrates the contrasts to distinguishing different phases within a single sample.

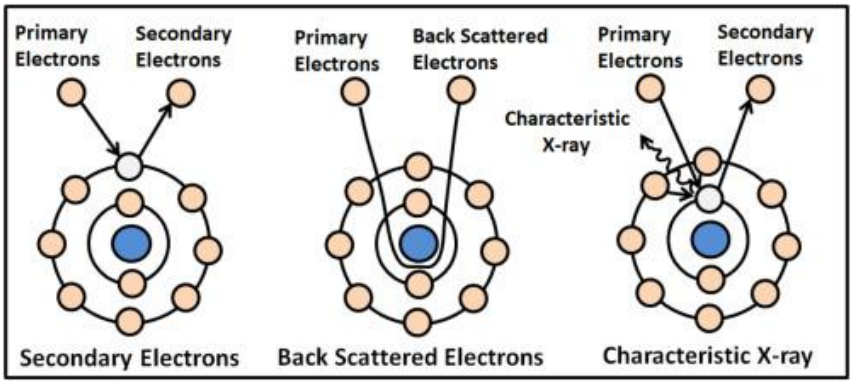

Figure 16: Schematical representation of scanning electron microscopy (SEM) working method. Reprinted from The Textile Institute Book Series, Volume of Characterisation of Polymers and Fibres, Mukesh Kumar Singh, Annika Singh, Chapter 17: Scanning electron microscope, Page no. 401, Copyright (2022), with permission from Elsevier.

Characteristics X-rays (Figure 16) are produced during an inelastic collision between incident electrons and the electrons in discrete orbitals of atoms in the sample. The excited electrons release x-rays when they return to the lower energy states. The yielded x-rays have a fixed wavelength which depends on the energy levels of electrons of different shells of the given sample, hence that can be used for elemental mapping. Also, some visible light (cathodoluminescence CL), and heat are released from the interaction. Different signals that are released from the interaction are detected by different detectors (Figure 17).

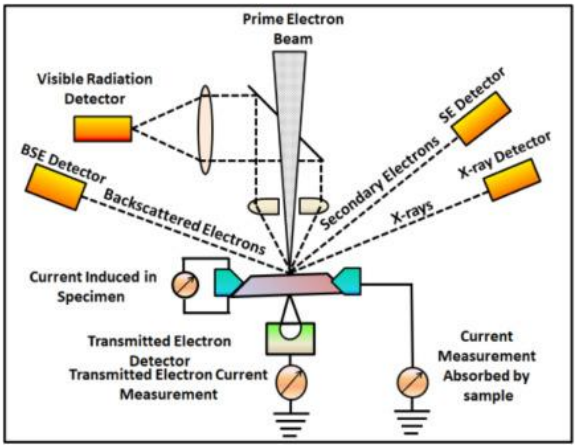

Figure 17: Schematical representation of scanning electron microscopy (SEM) working method. Reprinted from The Textile Institute Book Series, Volume of Characterisation of Polymers and Fibres, Mukesh Kumar Singh, Annika Singh, Chapter 17: Scanning electron microscope, Page no. 405, Copyright (2022), with permission from Elsevier.

At first, an adequate number of samples was taken from each of the candidates (raw samples and treated samples at different temperatures). After that, the samples were taken into V-vials, where they filled two-thirds of them. Then, Epofix resin was inserted into the V-vials by a

syringe. Epofix is a cold-setting and commercially available resin. The mixing process was done according to the instructions of the manufacturer [124]. After adding the resin, the mixture was stirred carefully so that no air bubbles were left in the solution. Finally, the solution was kept at room temperature for almost 24 hours to make it hardened.

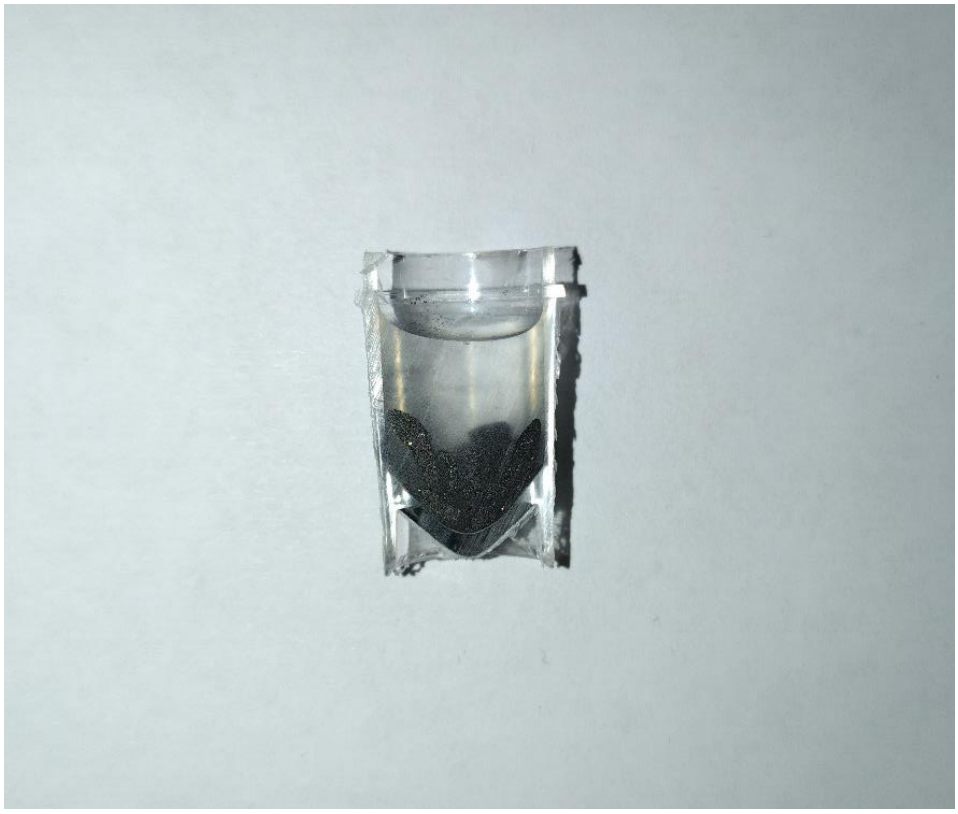

Figure 18: One part of the cut V-vials including a sample mixed with resin.

Once the resin gets hardened, the V-vials are vertically cut from the centre. Struers Secom-50 a commercially available table-top cut-off machine was used in the cutting operation. Since the size and type of the particles were different, their settling behaviour was also varied. So, they could end up at the different heights of the vial. Hence, cutting them horizontally would not be representative of all the particles. Thus, a vertical cut is more suitable than a horizontal one. One part from each slitted vial was placed into a 2-piece mould. The horizontal cut surface was facing upward during the process. The prepared resin was then added to the mould inside a commercially available vacuum impregnation unit, called Struers CitoVac.

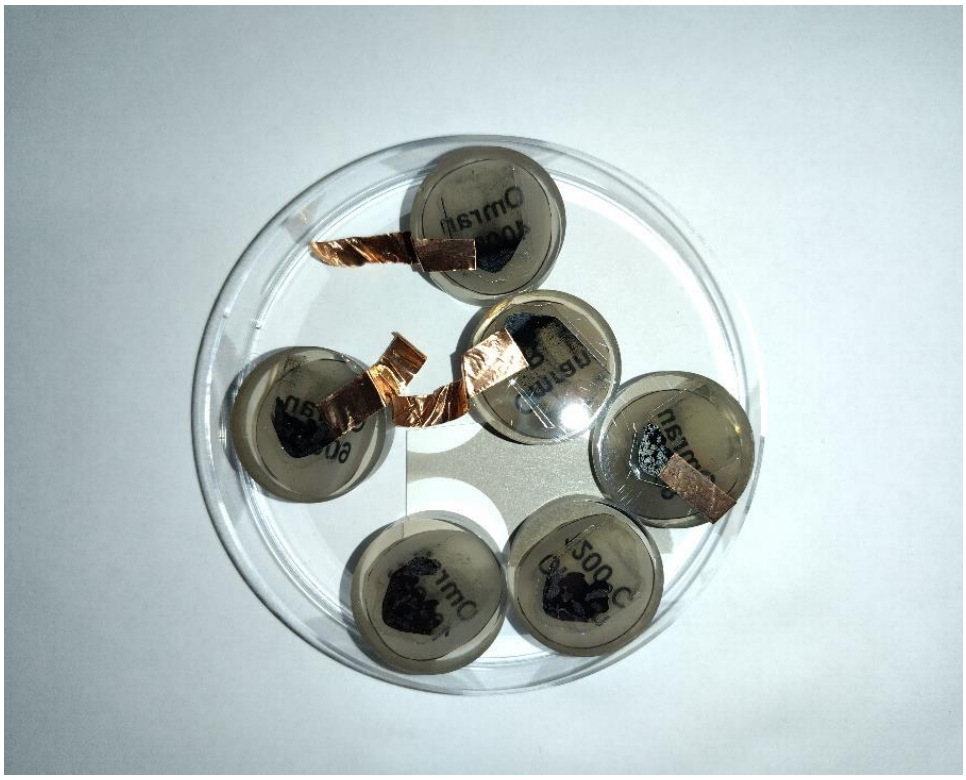

Figure 19: Hardened mould coated with metal ready for analysis.

The hardening process of the mould requires an oven, where the moulds were left for 24 hours at 40 °C. Next, the hardened moulds were taken out for the polishing steps. Similar to the other machines, a polishing machine was also commercially available, Struer LaboPol-6 is a grinding and polishing machine with a variable speed range between 120 to 1200 rpm. The polishing was done in several steps to get the desired surface for the analysis. The final step was to put a thin layer of carbon as a coating using a JEE-420 vacuum evaporator. The carbon-coated samples were analysed using a Zeiss ULTRA Plus field-emission scanning electron microscope (FE-SEM) equipped with energy-dispersive X-ray spectroscopy (EDX) from the Chemical Analysis unit of the University of Oulu.

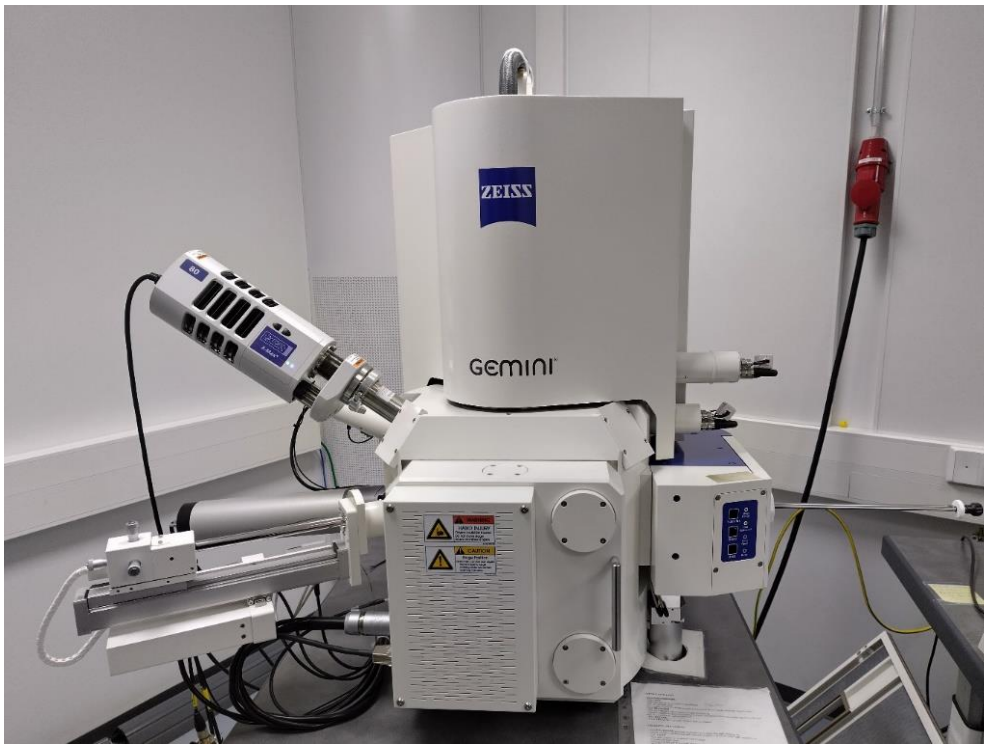

Figure 20: Zeiss ULTRA Plus SEM-EDX Machine.

3.3 Experiments

3.3.1 Differential Scanning Calorimetry – Thermogravimetric Analysis (DSC-TG) & Mass Spectrometry (MS)

The effect of conventional thermal treatment on the black mass was studied by DSC-TG coupled with mass spectroscopy (MS). Thermogravimetric analysis (TGA) was done to determine the mass changes occurring at different temperatures and differential scanning calorimetry (DSC) was used to examine the heat flow rate. DSC reveals if exothermic and endothermic chemical reactions take place during the measurement by comparing the heat flux required to heat the sample to the heat flux required to heat the reference pan. These thermal analysis techniques help determine the chemical properties of desired substances during cooling, heating, and while being rested at a constant temperature. At least two parameters need to be measured to conduct the analysis which implies at least two sensors will be needed, for example, a balance, and thermometer to measure mass and temperature respectively. Again, both would require some kind of calibration[125]. Simultaneously, to analyse the elemental composition of the gas leaving the sample, mass spectrometry analysis (MS) was also used. This process requires the ionization of the chemical compounds to generate charged molecules to measure the mass-to-charge ratio. The measurement can be done in many ways, such as electron ionization (EI), chemical ionization (CI), electrospray ionization (ESI), atmospheric pressure chemical

ionization (APCI), atmospheric solid analysis probe ionization (ASAP), atmospheric pressure photoionization (APPI), and matrix-assisted laser desorption/ionization (MALDI) technique [126]. In this work electron ionization (EI) measurement technique was used.

Figure 21: NETZSCH QMS 403 D Aeolos machine for DSC-TGA-MS experiment.

Figure 22: Crucibles for reference and sample used in DSC-TGA-MS experiment.

The experiments for this work were designed in two atmospheric conditions, air and inert (N_2 of 99.9995% purity). Aluminium oxide crucibles (Figure 22) were used in the process. Before making the DSC analysis, calibration was necessary for both atmospheric conditions. Temperature was increased at a rate of 10 °C/min from room temperature to 1200 °C. Primarily, CO/CO_2, F, Cl, CH_4, O, Mn, Li, OH, and Co were the targeted materials to be analysed from mass spectrometry. NETZSCH QMS 403 D Aeolos machine was used for the experiments.

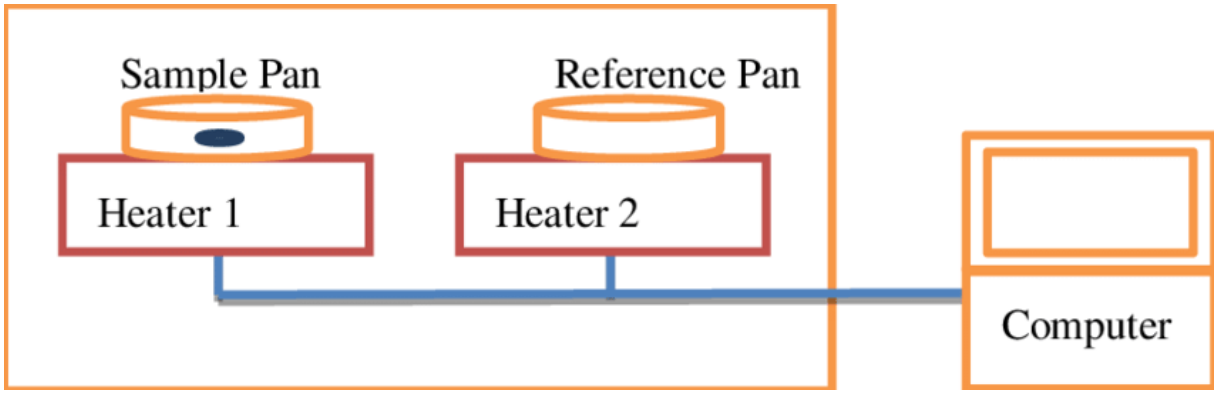

Figure 23: Simplified schematic of TGA-DSC experimental setup. Reused under CC BY 4.0 from ref [142].

3.3.2 Microwave Heating

The thermal pre-treatment of the black mass samples was carried out by a multimode microwave device with a maximum output power of 4kW and frequency of 2.45 GHz.

In general, the main components of the microwave device are:

a) Power source: A magnetron to produce the microwaves.

b) Waveguide: To transport the microwaves

c) Cavity or reaction area: To manipulate microwaves for a specific purpose.

d) Control system: To regulate the temperature and microwave power.

Samples were placed inside an aluminium oxide crucible having a diameter of 60 mm, and the height of the crucible was also 60 mm.

Figure 24: Alumina crucible used in the experiment.

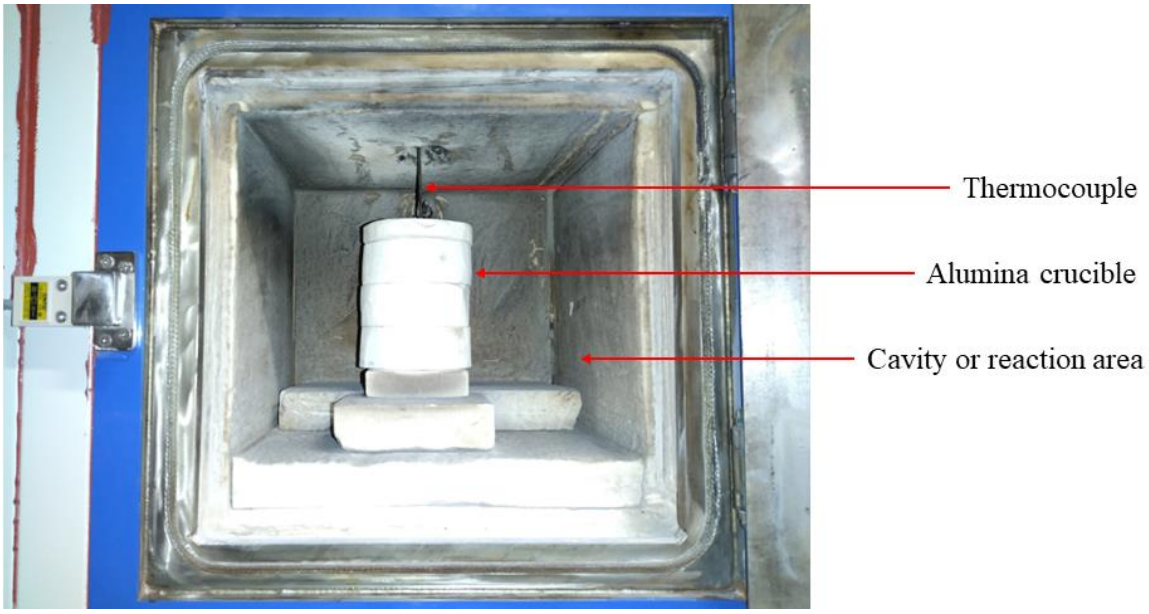

Figure 25: Alumina crucible placed inside the cavity of the microwave device.

To monitor the temperature, a thermocouple was used. The thermocouple provides feedback information to the control panel, which controls the power of the magnetron enabling controlling of the temperature of the sample during the microwave heating process. The vapour from the crucible was pulled by a pump and trapped in a collector. Basically, the pump was making the air flow through the crucible. The experiments were performed under ambient air atmosphere.

A total of five experiments were conducted where the samples were heated from room temperature to a maximum temperature of 400 ℃, 600 ℃, 800℃, 1000℃, and 1200 ℃.

Table 2. Experimental conditions

Experiment no.	Microwave Power (kW)	Temperature (℃)	Duration (min)
1	4	400	10
2	4	600	10
3	4	800	10
4	4	1000	10
5	4	1200	10

Samples were roasted for 10 minutes under each temperature range. After finishing the roasting process, samples were cooled to room temperature before taking them out of the furnace. The weight of each set of samples was measured before and after the roasting experiments.

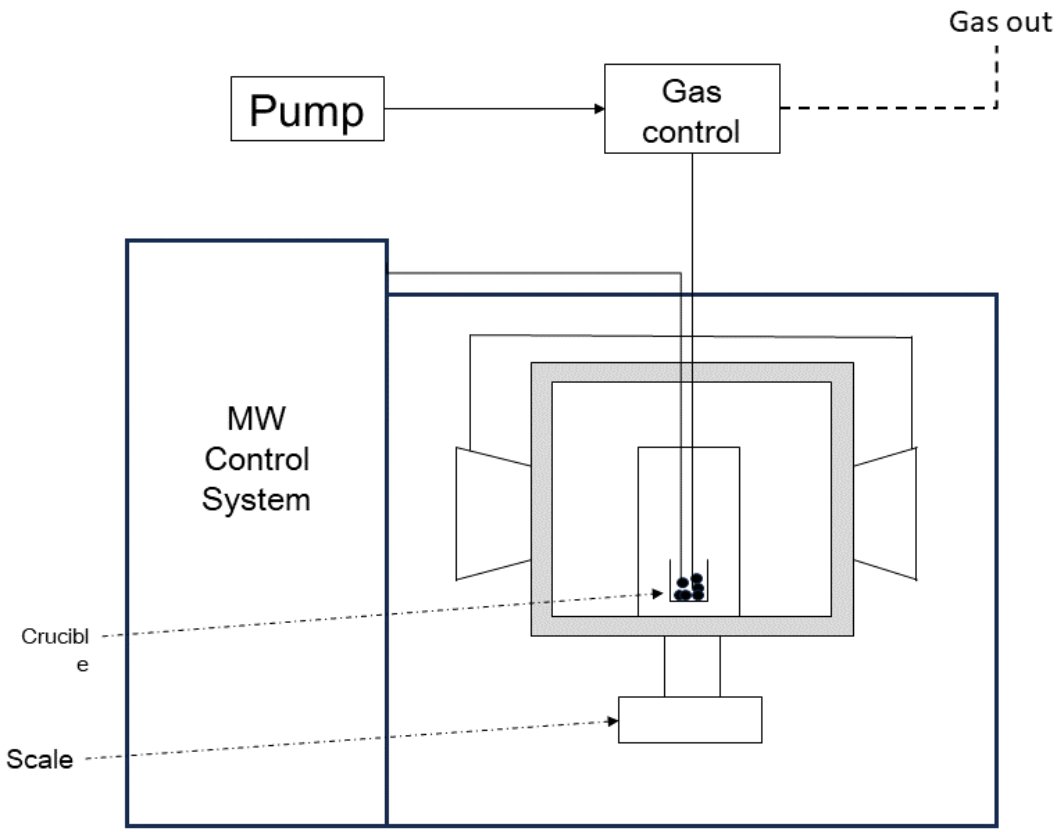

Figure 26: Schematic diagram of the microwave setup.

Figure 27: The microwave device used for the experiment.

4 Results and Discussion

4.1 Material Characterization

4.1.1 Chemical Composition

The chemical composition of the black mass was described in Table 1 of section 3.1.1. The important metallic elements are nickel (272.11 mg/g), lithium (38.93 mg/g), cobalt (38.54 mg/g), and manganese (15.55 mg/g). Traces of copper and aluminium are also present. The weight percentage of graphite in the mixture is 33%. Mousa et al. have also worked with black mass samples with closely related compositions. Their work consists of two types of black mass samples. The first one had 36% graphite, 17.5% cobalt, 5.1% nickel, 3.0% manganese, and 3.9% lithium along with some other elements. The other black mass sample contained 42.1% graphite, 5.4% cobalt, 12.5% nickel, 10.9% manganese, and 2.6% lithium. In both cases, the measurements were done on a weight basis [47].

4.1.2 Black-mass Phase (Crystal Structure)

The XRD results (Figure 28) revealed the crystal structure of the black mass sample. The figure shows the dominance of electrode materials, such as Lithium Cobalt Manganese Nickel Oxide, and Carbon. A huge peak of graphite is present in the graph at $2\theta = 30.9^{o}$ whereas a small peak at 64.38^{o} is also visible. There are several characteristic peaks for the cathode, with three major indications at 21.78^{o}, 52.08^{o}, and 42.8^{o} of 2θ value. In studies of mixed cathode materials with graphite, XRD results gave the same results where peaks can be seen in similar 2-theta values [47,62].

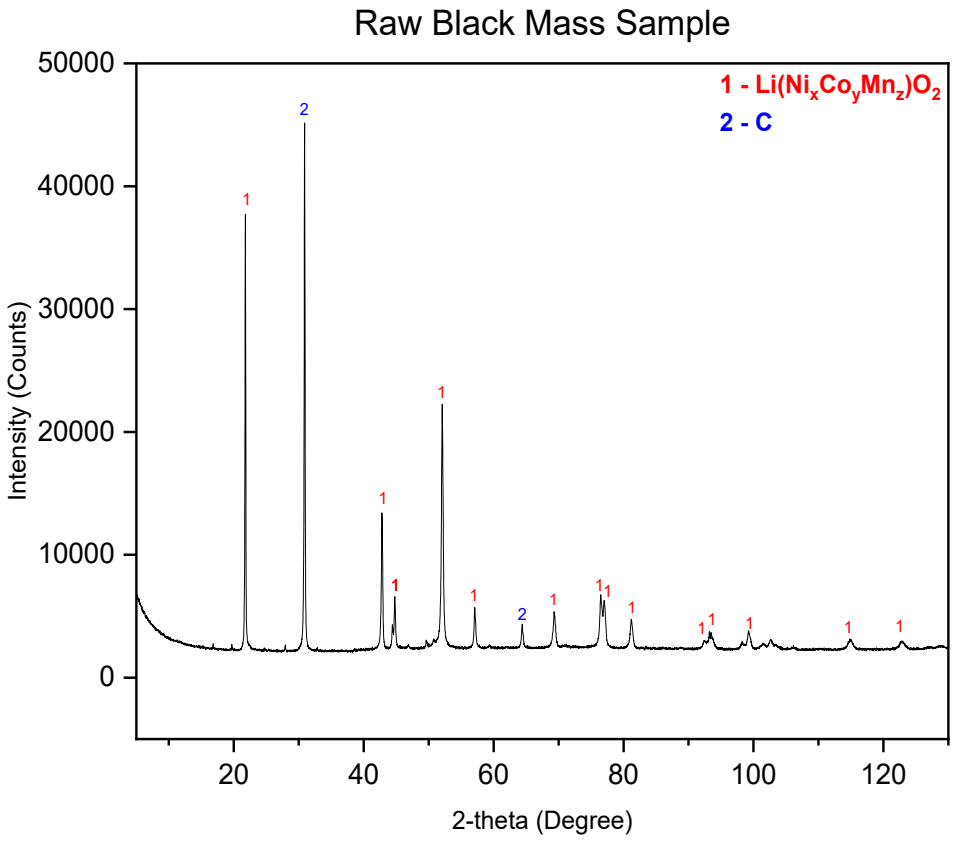

Figure 28: XRD results of the raw black mass sample.

4.1.3 Morphological Structure and Element Distribution (SEM-EDX)

The morphological structure of the raw sample was analysed using scanning electron microscopy. Figure 29 and Figure 31 show the structure in two different magnification levels. At 100 µm magnification, we can observe the distribution of cathodic and anodic materials. Dark flacks are assumed to be graphite and bright spots are Lithium Cobalt Manganese Nickel Oxide cathode.

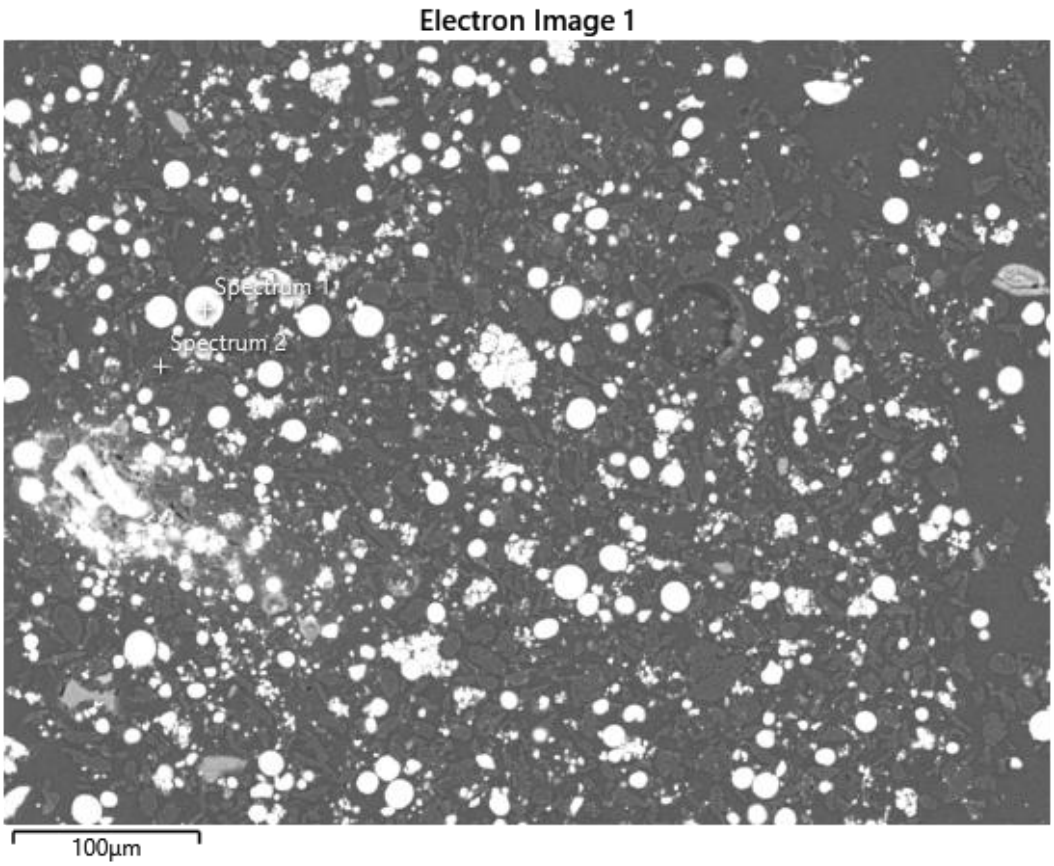

Figure 29: SEM image of raw sample at 100 µm magnification.

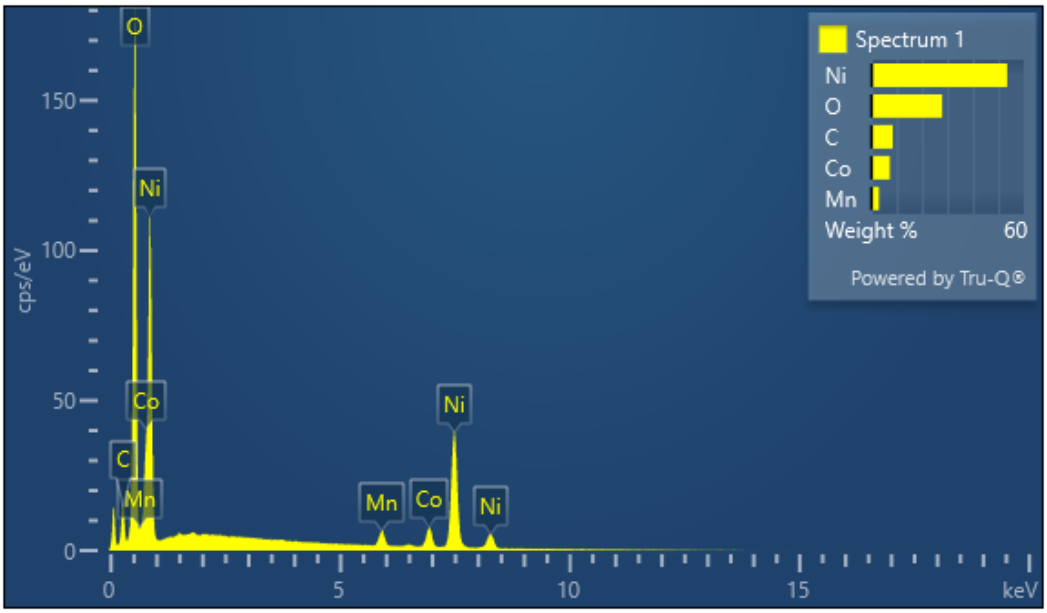

Figure 30: Acquired spectra from the SEM image at 100 µm magnification.

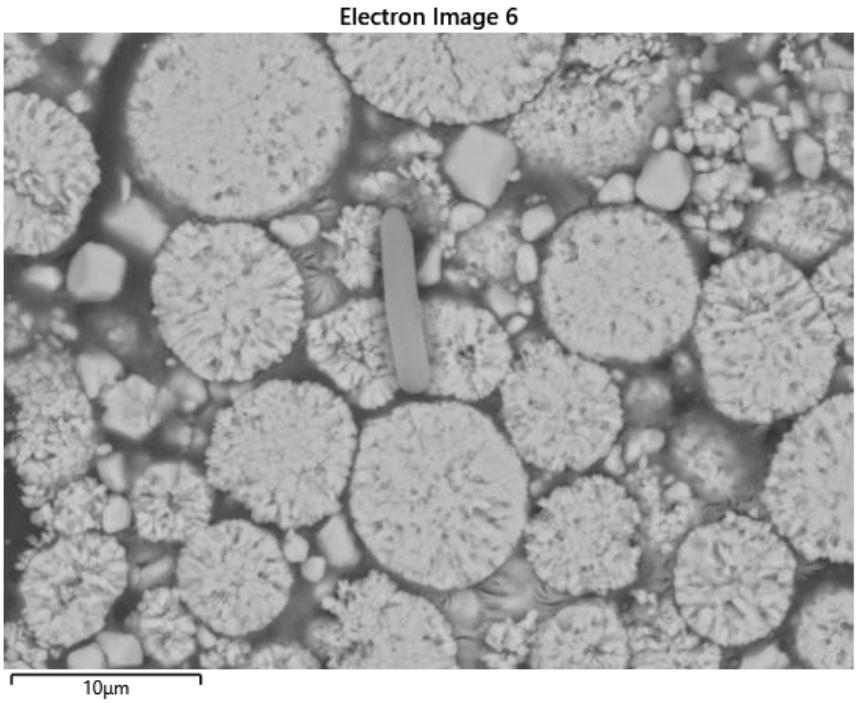

Figure 31: SEM image of the raw sample at 10 µm magnification.

Also, the acquired spectra from the EDX can be seen. We can observe (Figure 30) the presence of complex metals used in the manufacturing of cathode, such as cobalt, nickel, and manganese. Graphite and oxygen are also detected. All of these elements were also noticed in the XRD analysis.

Figure 32: EDX layered image of the raw sample.

Even though lithium was not visible in the spectrum figure, we can notice traces of it in the elemental mapping along with other elements of the sample (Figure 32. d). Here, the dominance of nickel is also noticeable (Figure 32. a). Traces of fluorine (Figure 32. i), copper (Figure 32. g) and aluminium (Figure 32. h), calcium (Figure 32. j), potassium (Figure 32. k) and phosphorus (Figure 32. l) are found in these images. Carbon (Figure 32. e) and oxygen (Figure 32. f) can be seen simultaneously. Other metals cobalt (Figure 32. b) and manganese (Figure 32. c) is being distributed almost evenly throughout the site.

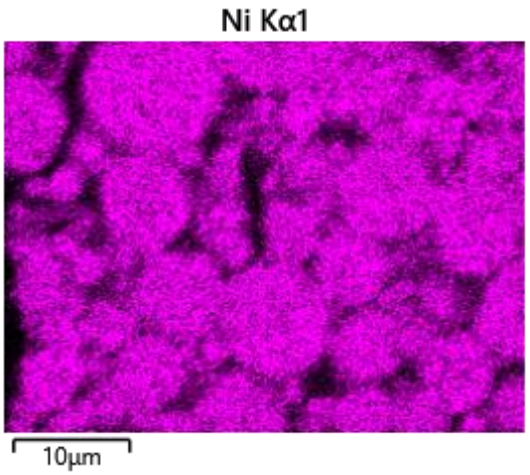

Figure 32. a: EDX mapping for nickel.

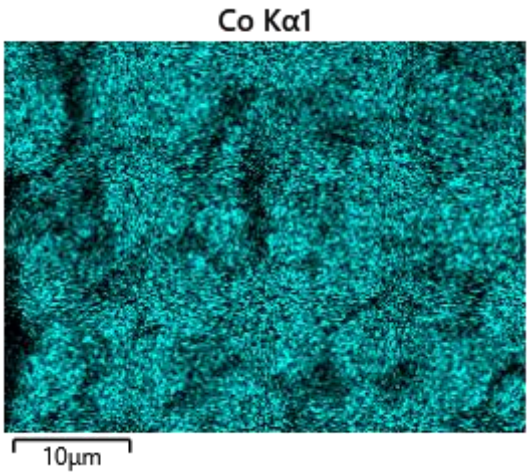

Figure 32. b: EDX mapping for cobalt.

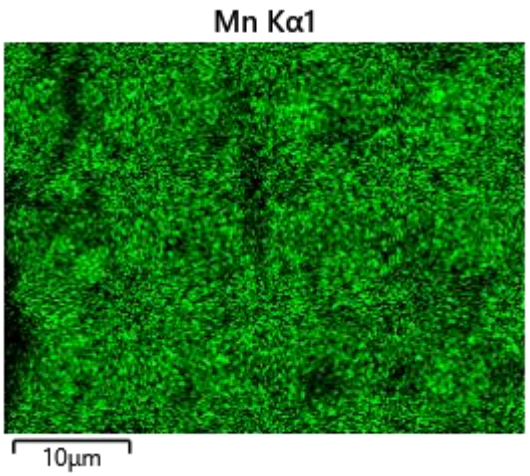

Figure 32. c: EDX mapping for manganese.

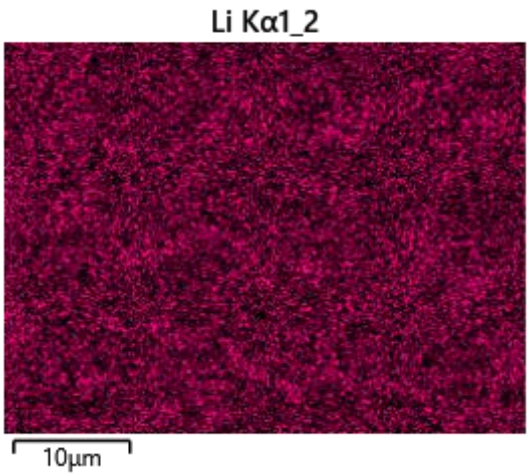

Figure 32. d: EDX mapping for lithium.

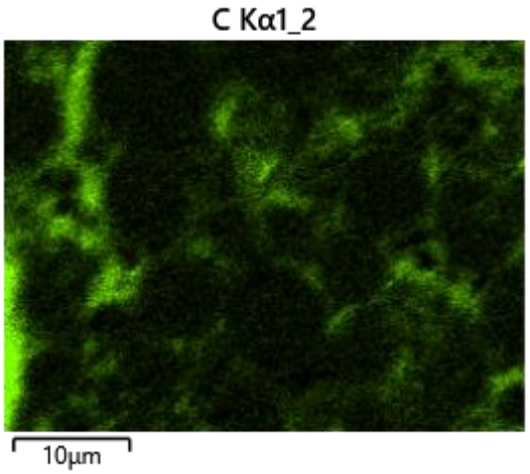

Figure 32. e: EDX mapping for carbon.

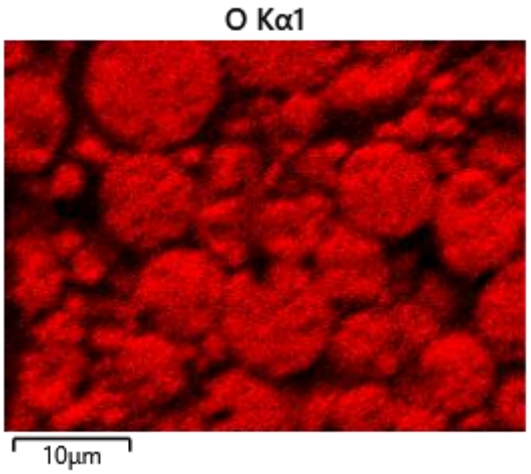

Figure 32. f: EDX mapping for oxygen.

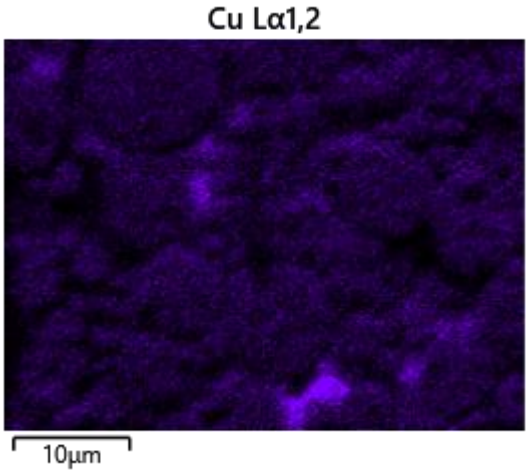

Figure 32. g: EDX mapping for copper.

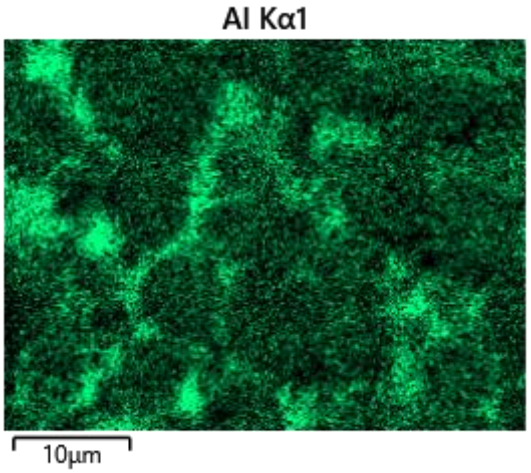

Figure 32. h: EDX mapping for aluminium.

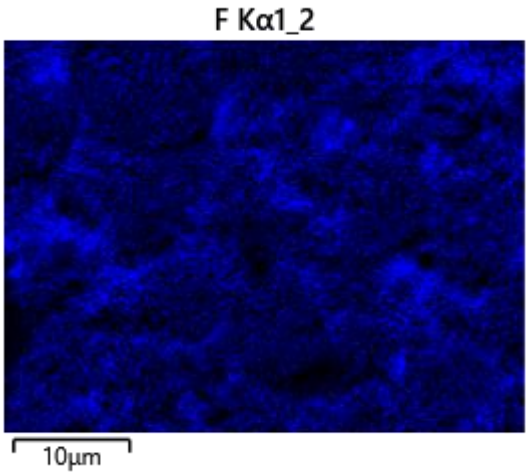

Figure 32. i: EDX mapping for fluorine.

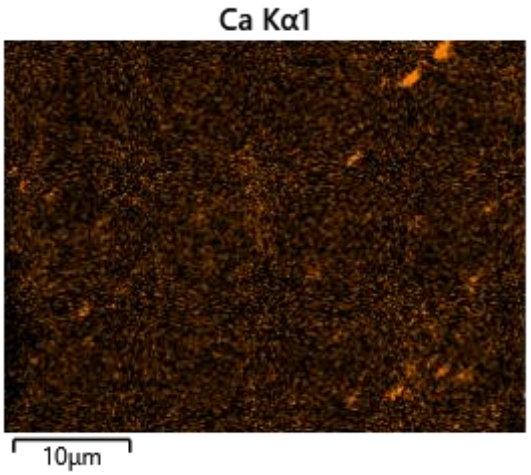

Figure 32. j: EDX mapping for calcium.

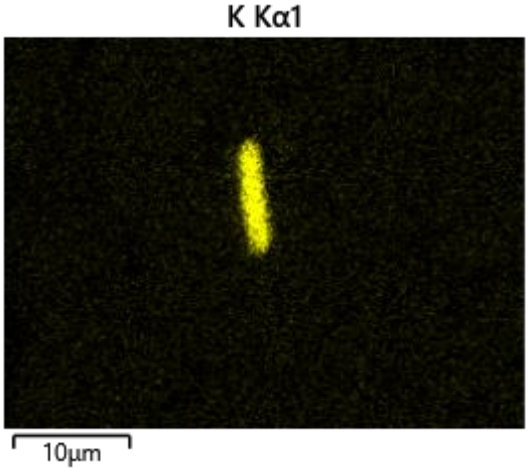

Figure 32. k: EDX mapping for potassium.

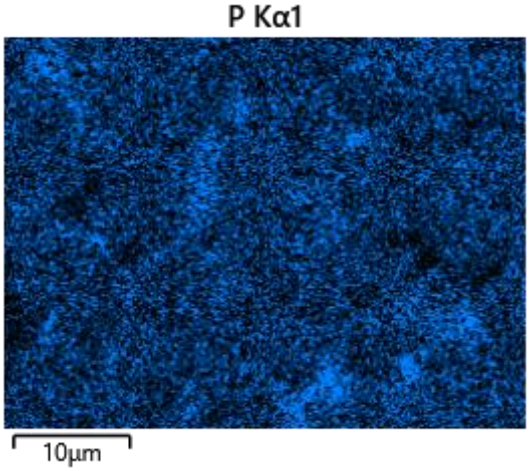

Figure 32. l: EDX mapping for phosphorus.

4.2 Effect of Thermal Treatment on The Black-mass Behaviour

4.2.1 DSC-TG-MS Under Air Atmosphere

The result from the analysis is illustrated in Figure 33. The whole thermal treatment can be divided into 4 parts according to the diagram. At first (stage 1), with the increasing temperature, the moisture present in the sample would start to evaporate. This phenomenon can be observed from the mass-spectrometry results as well. We can see two characteristic peaks, each in Figure 33. c and Figure 33. d which indicates the vaporization of the moisture contents is occurring in that region. A mass loss of 3.39 % per cent can be seen from the TG curve at this stage. Further, an increase in the temperature would cause volatile materials to be removed from the sample. This process (stage 2) starts at 266.19 ℃ temperature. Another 4.37% of the total loss is seen at 511.97 ℃.

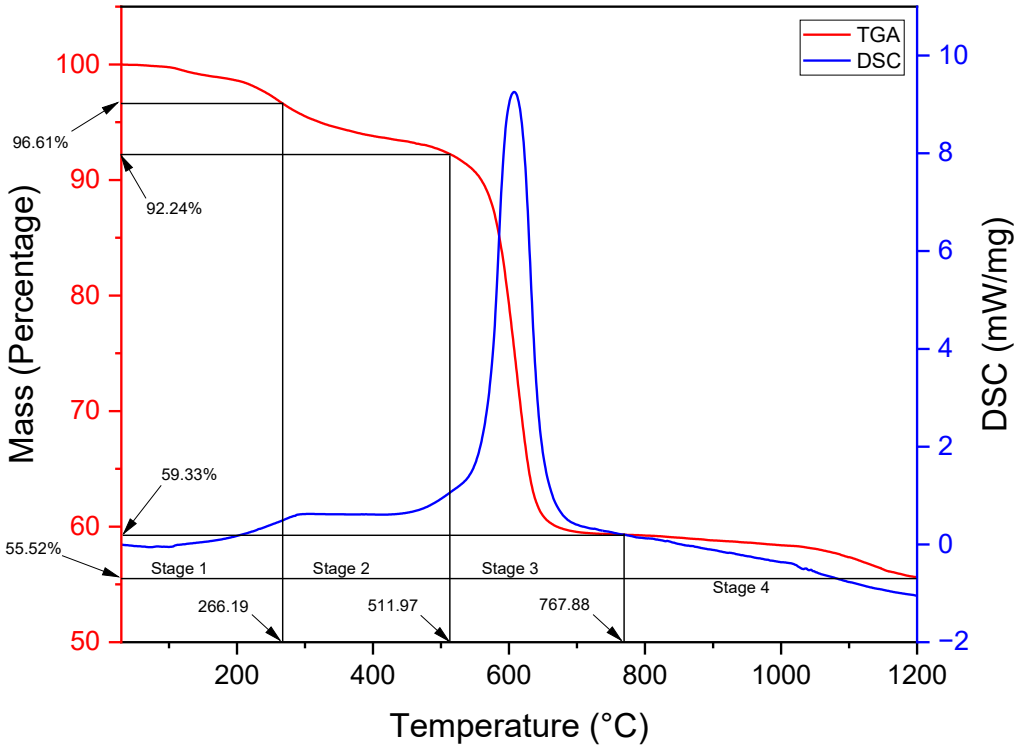

Figure 33: TGA and DSC curves of the black mass in air atmosphere.

From the mass spectrometry figures (Figure 33. e) it is evident that fluoride compounds are decomposing in that temperature range. Then, a big exothermic peak in the DSC curve around 600 °C suggests the decomposition of cathode structures and freed oxygen reacting with the graphite producing CO_2. From Figure 33. b and 33. g) in the mass spectrometry, peaks of oxygen and carbon dioxide are visible. Breaking down of the cathodic structure helps the metals to form metallic oxides as well.

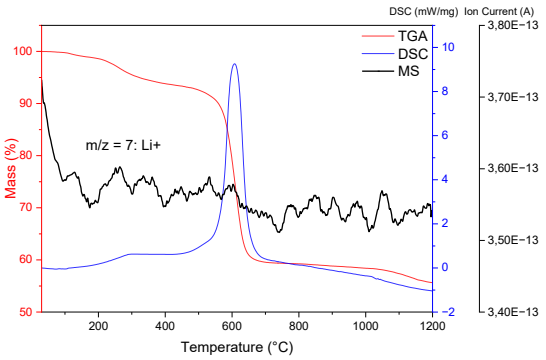

Figure 33. a: Mass spectrometry for lithium.

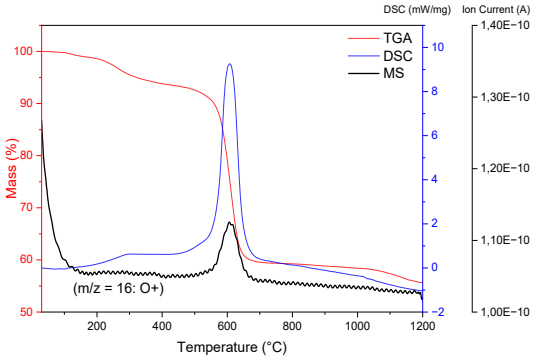

Figure 33. b: Mass spectrometry for oxygen.

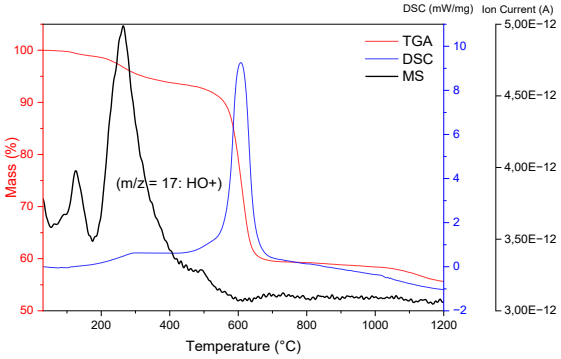

Figure 33. c: Mass spectrometry for HO.

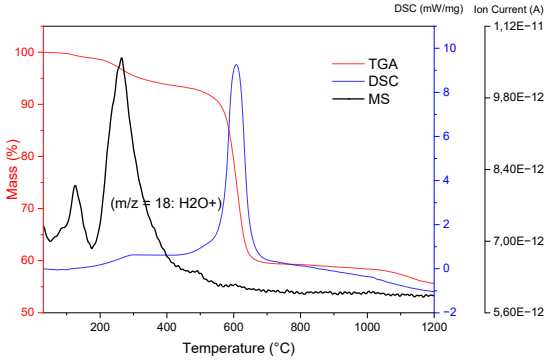

Figure 33. d: Mass spectrometry for H_2O.

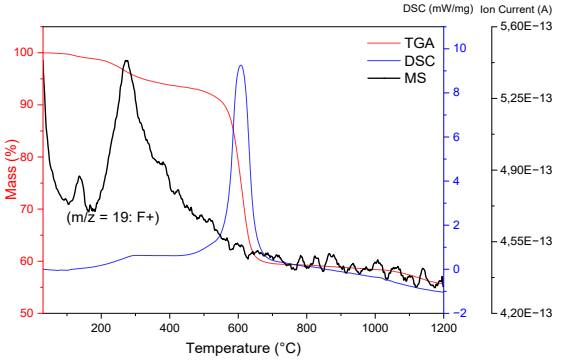

Figure 33. e: Mass spectrometry for fluorine.

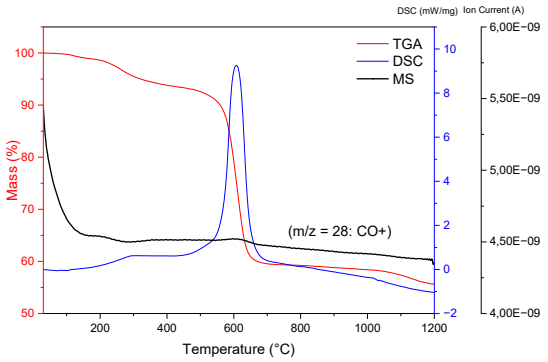

Figure 33. f: Mass spectrometry for CO.

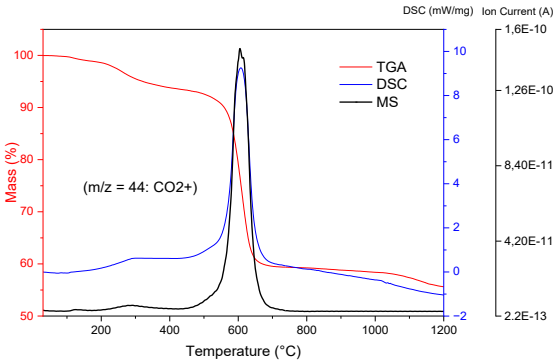

Figure 33. g: Mass spectrometry for CO_2.

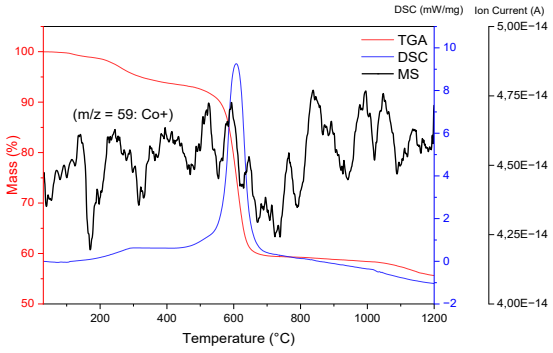

Figure 33. h: Mass spectrometry for Cobalt.

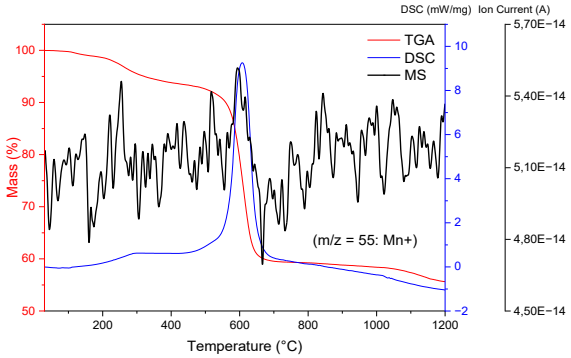

Figure 33. i: Mass spectrometry for Manganese.

A rapid mass loss happens at 767.88 °C temperature. By the end of this stage (stage 3) total remaining mass would be 59.33 %. Finally, higher valence oxides would decompose in the air atmosphere, for example, Co_2O_3 can be formed into CoO due to the higher temperature. formation of metallic values could not be seen from the mass spectrometry data. Possible reason for that could be the ample amount of oxygen making that difficult to happen at a higher temperature. Possible reactions under the given conditions are:

$$LiNi_xMn_yCo_zO_2 + O_2 \rightarrow Li_2O + Co_2O_3 + Mn_3O_4 + NiO + O_2$$

$$C + O_2 \rightarrow CO_2$$

$$C + O_2 \rightarrow CO$$

After the treatment at 1200 °C, 55.52 % of the total mass from the black mass sample remained. The mass loss was approximately close to the initial graphite content of the sample. A huge amount of mass loss happens due to the combustion of the graphite present in the sample to form CO_2 and a small amount of CO gases. The reason behind this can be related to the availability of oxygen inside the chamber which promotes the generation of these gases.

XRD analysis was done on the residue from TG analysis. The results (Figure 34) showed that the peaks confirmed the substances that we mentioned above. The only exception would be the phase of Li_2CO_3 which is missing. A possible reason could be the lower crystallinity of that phase. Also, the graphite phase is missing, indicating that almost all of them were burned and released as gases.

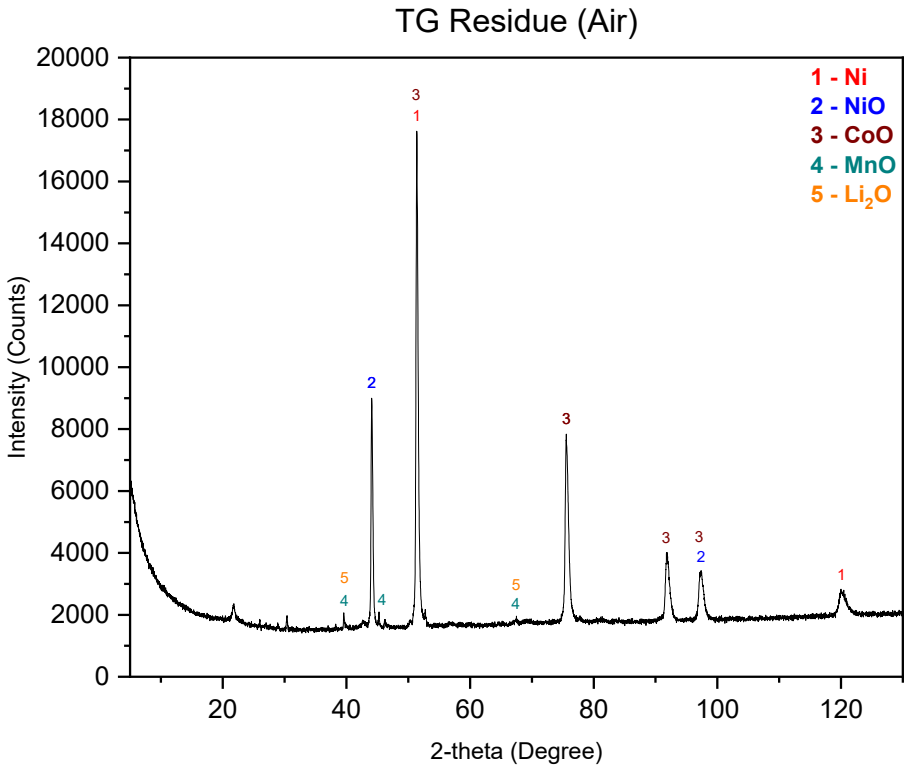

Figure 34: XRD results of the residue from TG analysis in air atmosphere.

SEM image gives us the morphological structure of the residual sample from the TG analysis. We can observe the breakdown of the cathodic structure into smaller agglomerations. The flake-like shape of graphite is missing from the image suggesting the release of graphite as gases after burning. However, from the elemental mapping, some traces of carbon can still be seen. Also,

the spectra figure contains a graphite peak along with manganese, cobalt, nickel, and oxygen. All the materials that were present in the raw sample are also present in the mapping diagram. However, their intensity is different. The same phenomenon with lithium happened here as well.

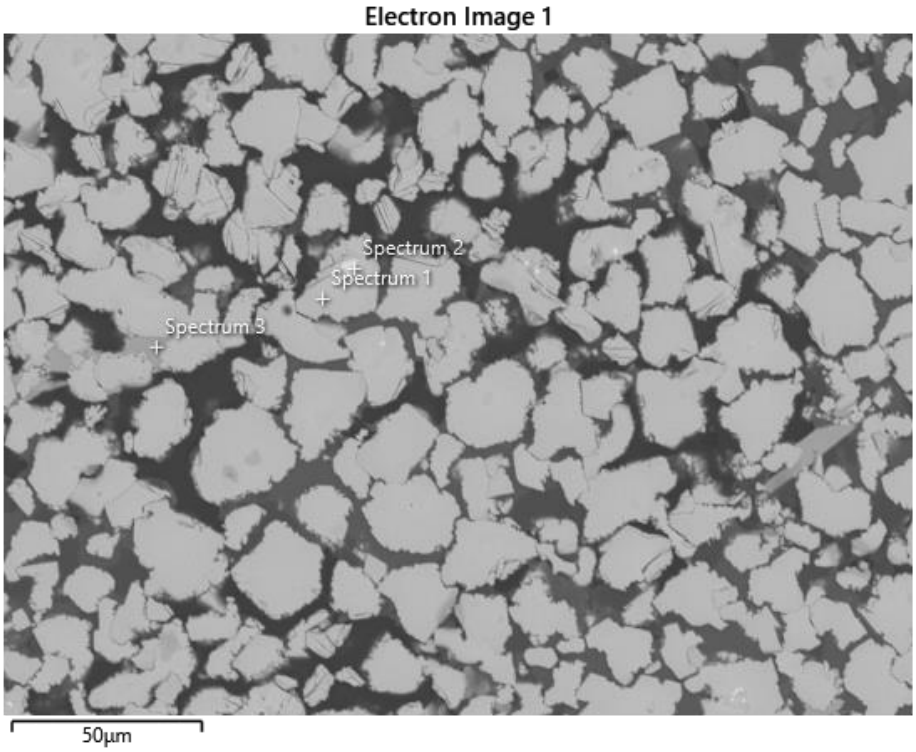

Figure 35: SEM image of TG residue from air atmosphere.

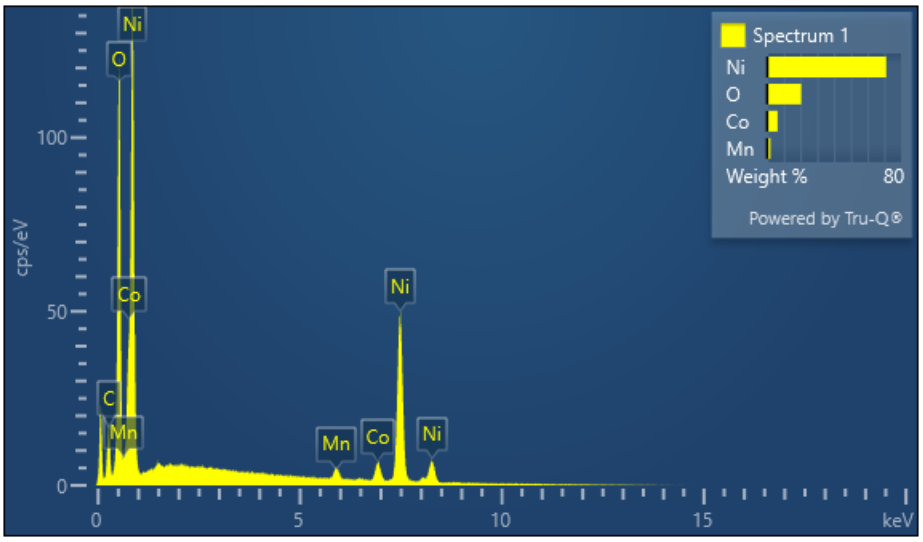

Figure 36: Spectra of TG residue from air atmosphere.

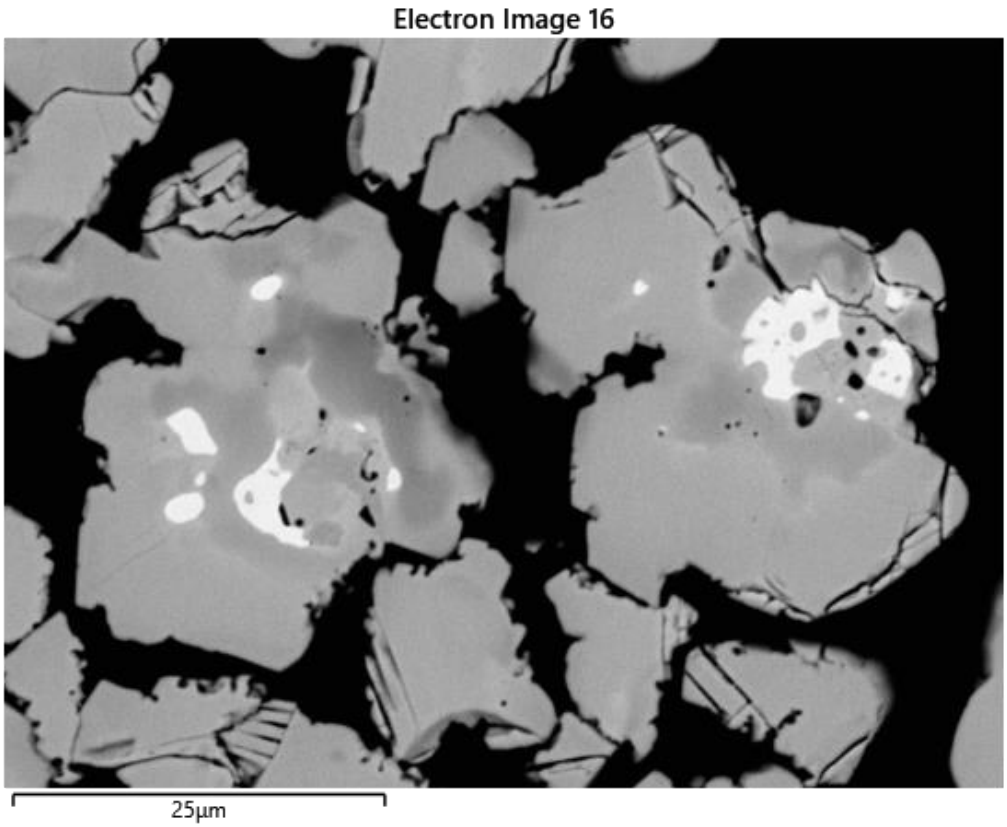

Figure 37: SEM image of TG residue from air atmosphere at 25 µm magnification.

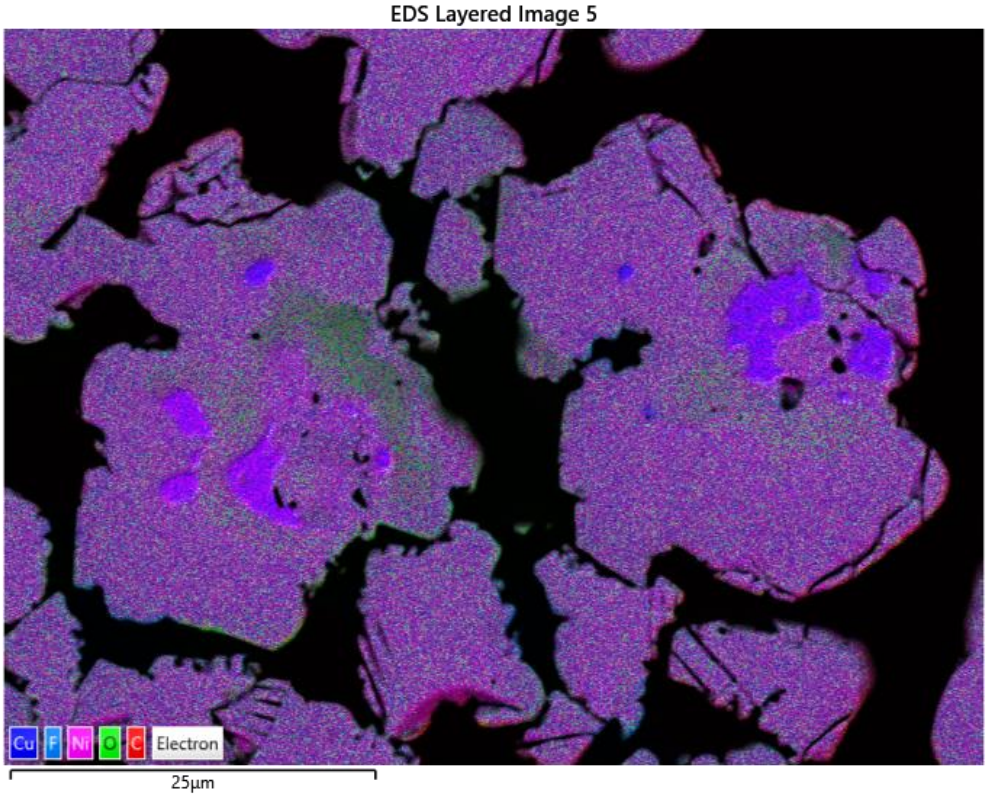

Figure 38: EDX layered image of the TG residue from air atmosphere.

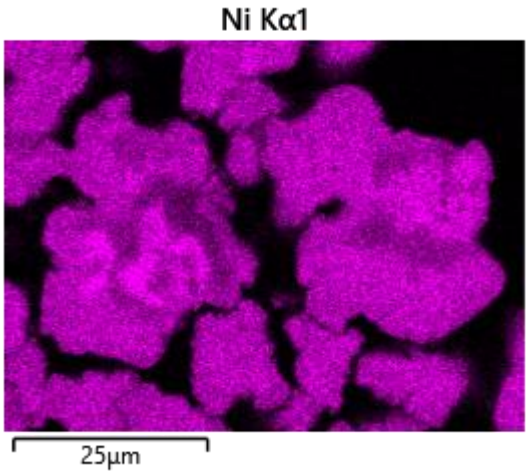

Figure 38 a: EDX mapping for nickel.

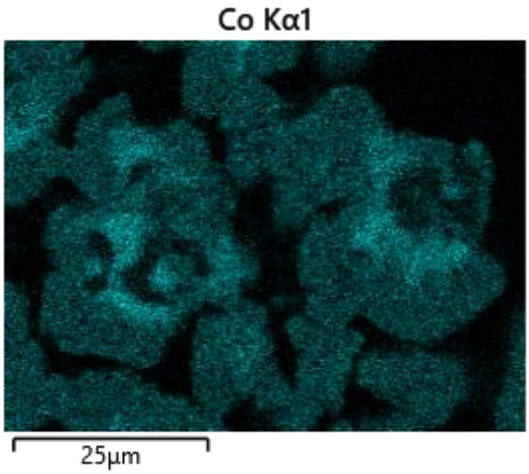

Figure 38 b: EDX mapping for cobalt.

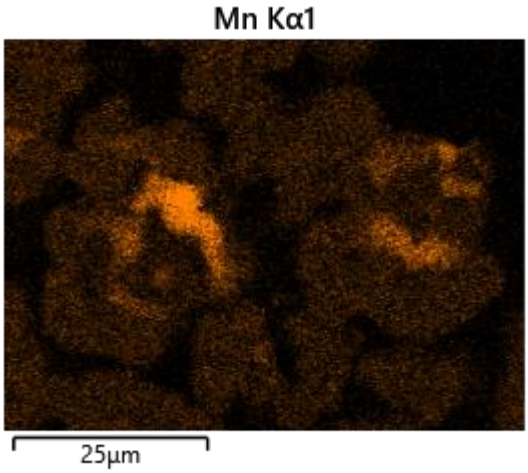

Figure 38 c: EDX mapping for manganese.

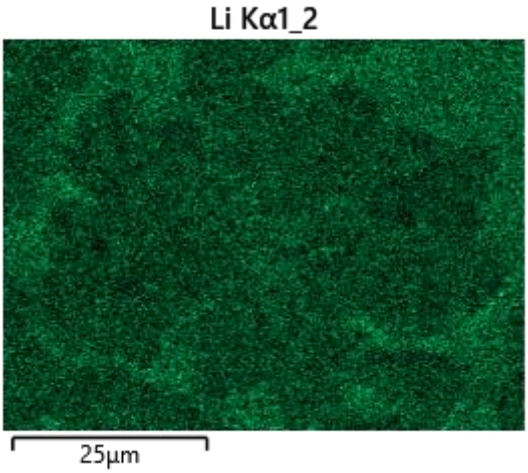

Figure 38 d: EDX mapping for lithium.

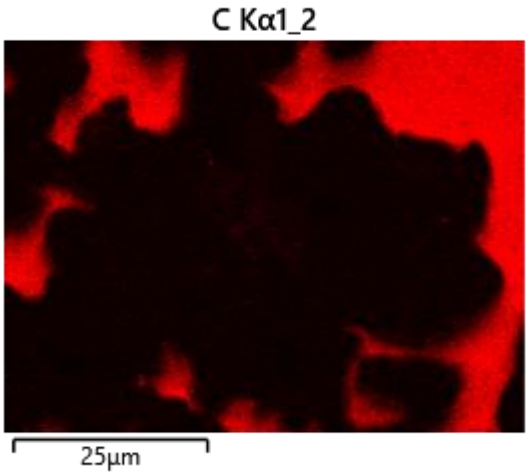

Figure 38 e: EDX mapping for carbon.

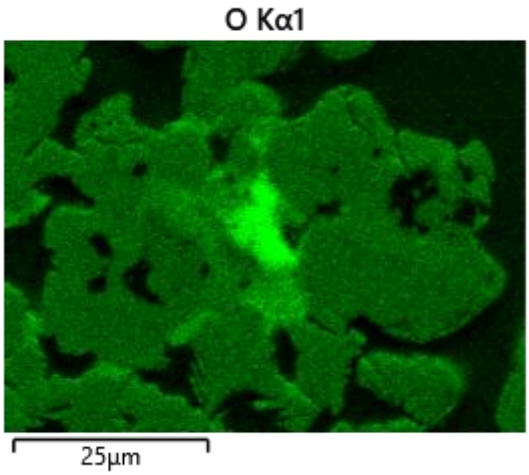

Figure 38 f: EDX mapping for oxygen.

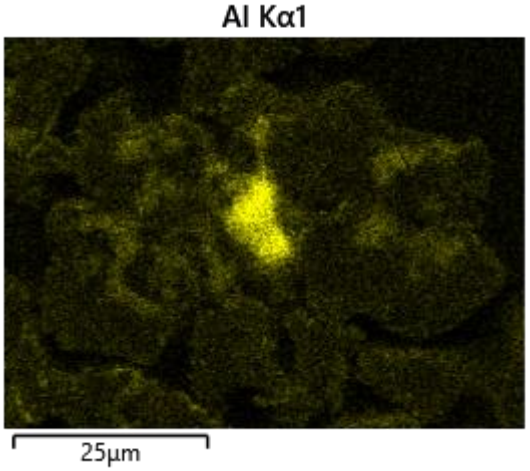

Figure 38 g: EDX mapping for aluminium.

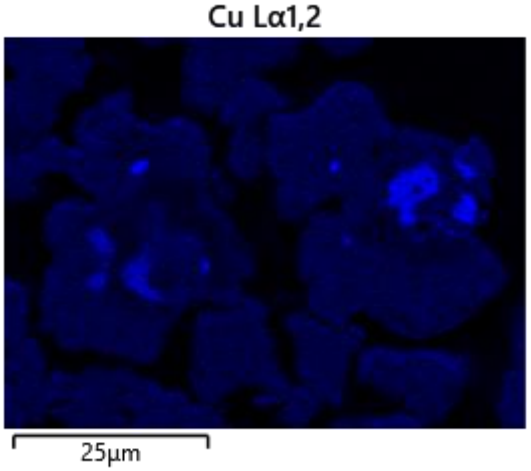

Figure 38 h: EDX mapping for copper.

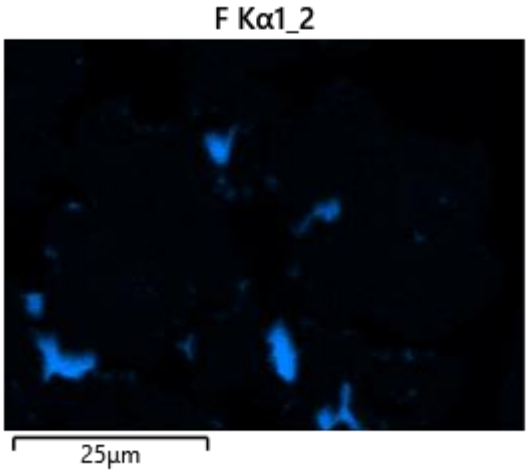

Figure 38 i: EDX mapping for fluorine.

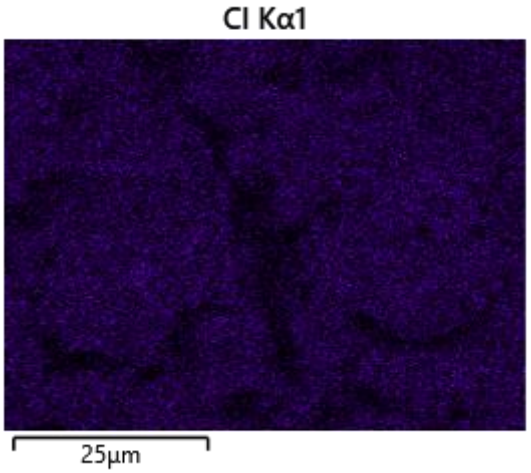

Figure 38 j: EDX mapping for chlorine.

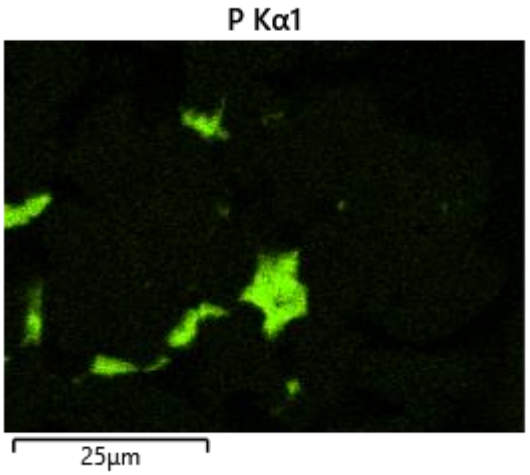

Figure 38 k: EDX mapping for phosphorus.

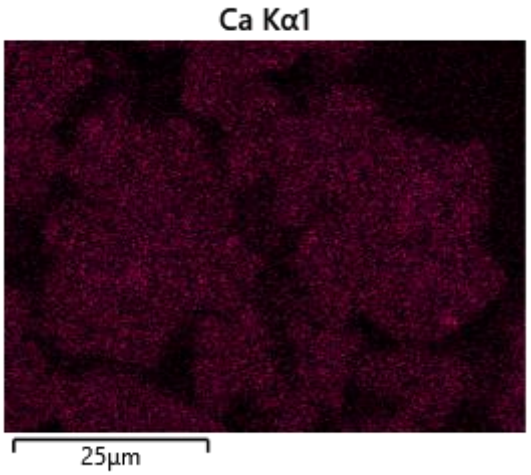

Figure 38 l: EDX mapping for calcium.

Li et al. also tried to analyse the thermal behaviour of lithium-ion batteries by TGA-DSC analysis in the air atmosphere. They used LCO cathode in their analysis with varying amounts of graphite. One sample, that contains 35.95 wt% of graphite can be compared to our results. The TG curve from their experiment looks like the graph that we found. The only difference would be the total mass loss, which is 40% of the total mass, slightly less than that of this work. From the heat flow curve, a huge exothermic peak is also visible. Another distinction is also realised here when there are some small endothermic peaks slightly before and after 1200 °C [53].

4.2.2 DSC-TG-MS Under Inert Atmosphere

Thermal treatment on black mass in an inert atmosphere has given some complex results compared to air atmospheric conditions. Figure 39 exhibits the mass change and heat flow rates during the thermal heating process. Like the air atmospheric conditions, a steady mass reduction (stage 1) can be seen which can be an indication of the evaporation of moisture in the sample. The quantity of the mass losses is also alike, as expected In the mass spectrometry graphs (Figure 39. c and 39. d) during that range of temperature activity of HO^+ (m/z = 17), and H_2O^+ (m/z = 18) can be visualised.

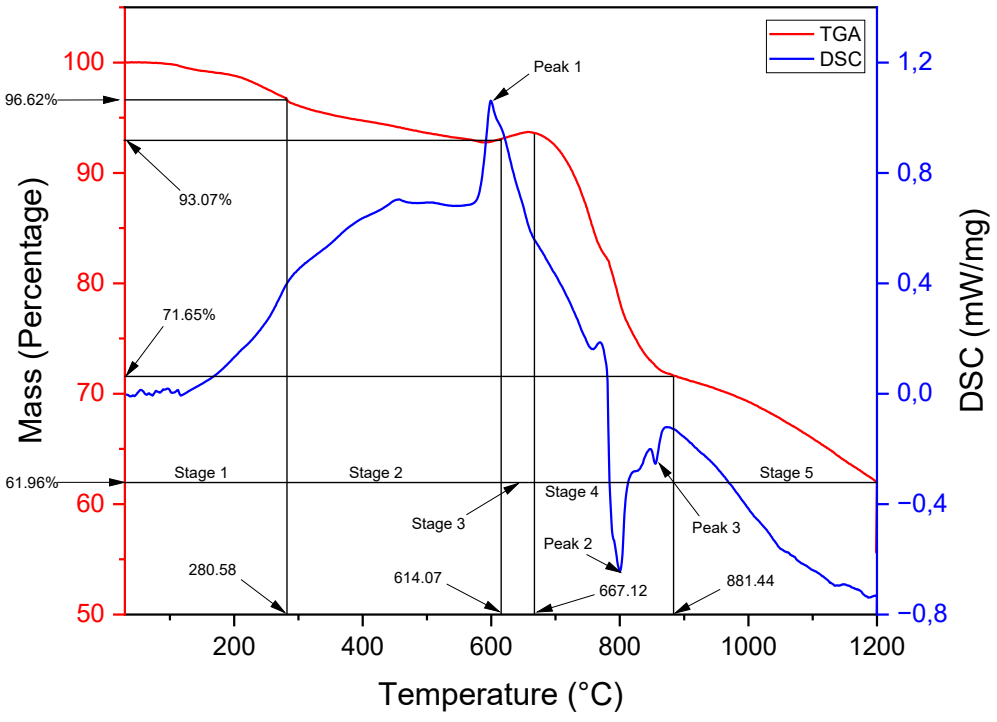

Figure 39: TGA and DSC curves of black mass in an inert atmosphere.

Again, same as the air atmospheric condition, volatile organic and inorganic materials would be volatized. From the mass spectrometry diagram (Figure 39. e), we can see that, fluorine starts to separate from the sample at around 200 ℃ and continues till around 500 ℃. In the air atmosphere, only a peak for fluorine in the MS graph is observed at 274 ℃. At 614.07 ℃ total remaining mass was 93.07%. An exothermic peak in the DSC curve and mass spectrometry curve (Figure 39. b and 39. g) indicate some formation of CO_2. Then, a little mass gain can be observed until 667.12 ℃ which could be because of the metallic elements forming oxides with the oxygen released from the cathode. During that time, the amount of CO_2 and O_2 decreased according to the mass spectrometry, which could be an indication of forming metal oxides.

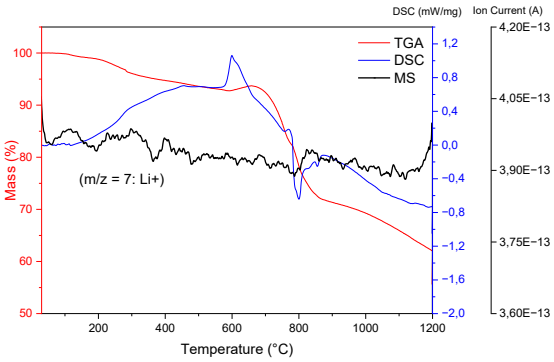

Figure 39. a: Mass spectrometry for lithium.

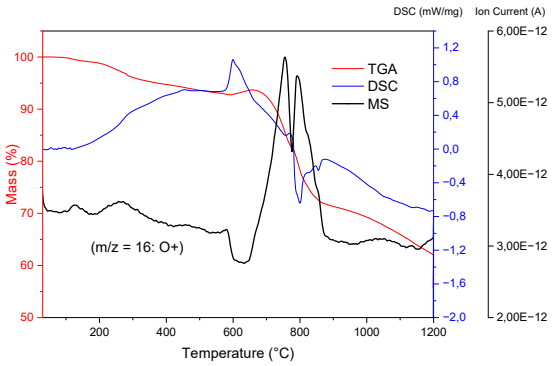

Figure 39. b: Mass spectrometry for oxygen.

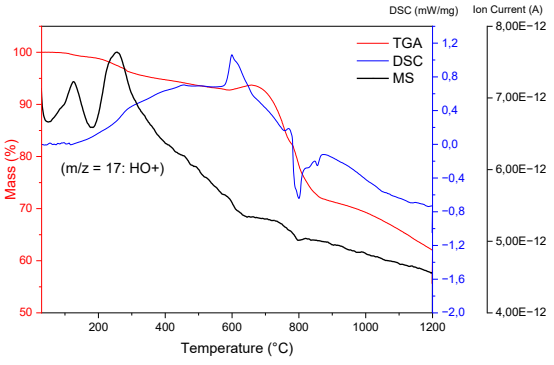

Figure 39. c: Mass spectrometry for HO.

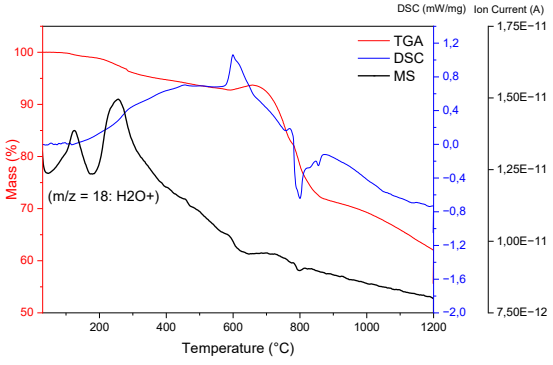

Figure 39. d: Mass spectrometry for H_2O.

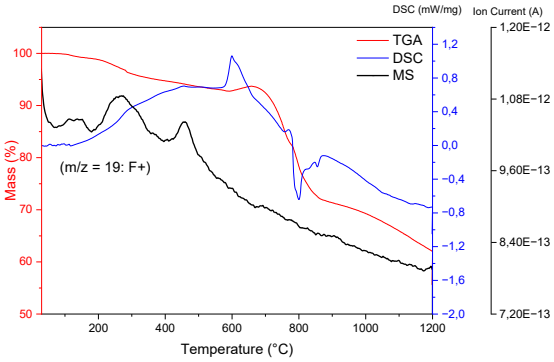

Figure 39. e: Mass spectrometry for fluorine.

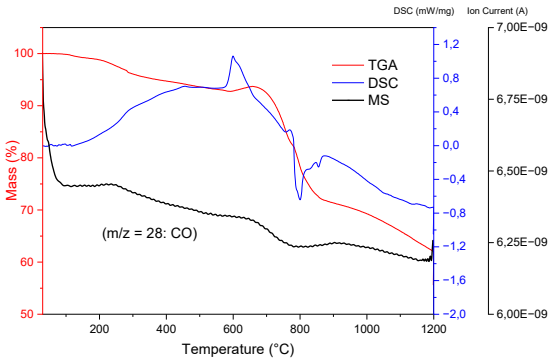

Figure 39. f: Mass spectrometry for CO.

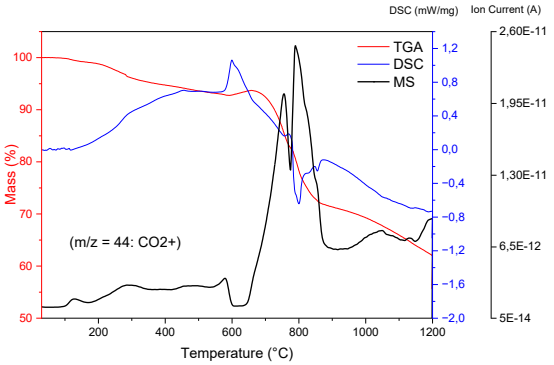

Figure 39. g: Mass spectrometry for CO_2.

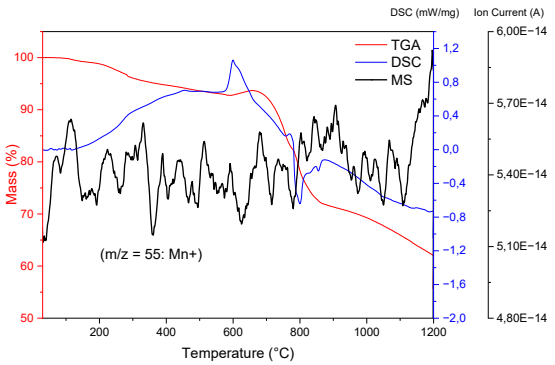

Figure 39. h: Mass spectrometry for manganese.

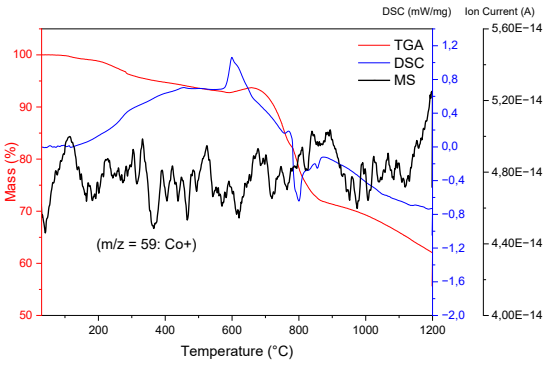

Figure 39. i: Mass spectrometry for cobalt.

Starting around 800 °C a series of endothermic peaks were produced in the DSC curve. Before that, another small exothermic peak can also be seen. At this point (stage 4) rapid mass loss is visible in the TG curve, implying the breakdown and reduction of the cathode structure and the formation of different metal oxides and metals along with the formation of CO_2. Finally, after

881.44 °C rate of mass decreases slightly, and another big endothermic peak appears. Possible reactions under the given conditions are:

$$LiNi_xMn_yCo_zO_2 \rightarrow Li_2O + CoO + Mn_3O_4 + NiO + O_2$$

$$C + O_2 \rightarrow CO_2$$

$$C + O_2 \rightarrow CO$$

$$Li_2O + CO_2 \rightarrow Li_2CO_3$$

$$Mn_3O_4 + C \rightarrow MnO + CO_2$$

$$Mn_3O_4 + C \rightarrow MnO + CO$$

$$Mn_3O_4 + CO \rightarrow MnO + CO_2$$

$$MnO + C \rightarrow Mn + CO_2$$

$$MnO + C \rightarrow Mn + CO$$

$$MnO + CO \rightarrow Mn + CO_2$$

$$CoO + C \rightarrow Co + CO_2$$

$$CoO + C \rightarrow Co + CO$$

$$CoO + CO \rightarrow Co + CO_2$$

$$NiO + C \rightarrow Ni + CO_2$$

$$NiO + C \rightarrow Ni + CO$$

$$NiO + CO \rightarrow Ni + CO_2$$

After the whole process, the total remaining mass was 61.96 %. More remaining mass in the residue could indicate that all graphite was burning in the presence of sufficient air atmosphere. More oxygen can significantly increase the burning of graphite present in the black mass mixture. However, in an inert atmosphere, due to insufficient oxygen, more metallic oxides can be reduced to their metallic form, which will be easier to separate from the mixture. More precision in the analysis would have been possible, if we could determine the amount of graphite present in each sample.

An experiment was conducted by Zhang et al. where they analysed the mass reduction and reaction peaks at a range of 50 ℃ to 1000 ℃ in an inert atmosphere. They worked with two types of samples, only cathode materials and cathode mixed with spent anode. In their results for the sample of mixed electrodes, there were also two exothermic peaks (at 670℃ and 708 ℃) and one endothermic peak (at 969 ℃). Even though the reaction peak's locations differ from our work, the similarity between the mass reduction can be observed. In both cases, a steep downward trend can be seen when the temperature is around 700 ℃ to 800 ℃. Total mass loss after 1000 ℃ can also be considered alike [127]

From the XRD analysis (Figure 40), we could identify the presence of metallic cobalt, nickel, and manganese which have overlapping peaks. Also, their oxides remained within the sample along with lithium oxides. Another compound of lithium, LiF and a peak indicating graphite is also visible.

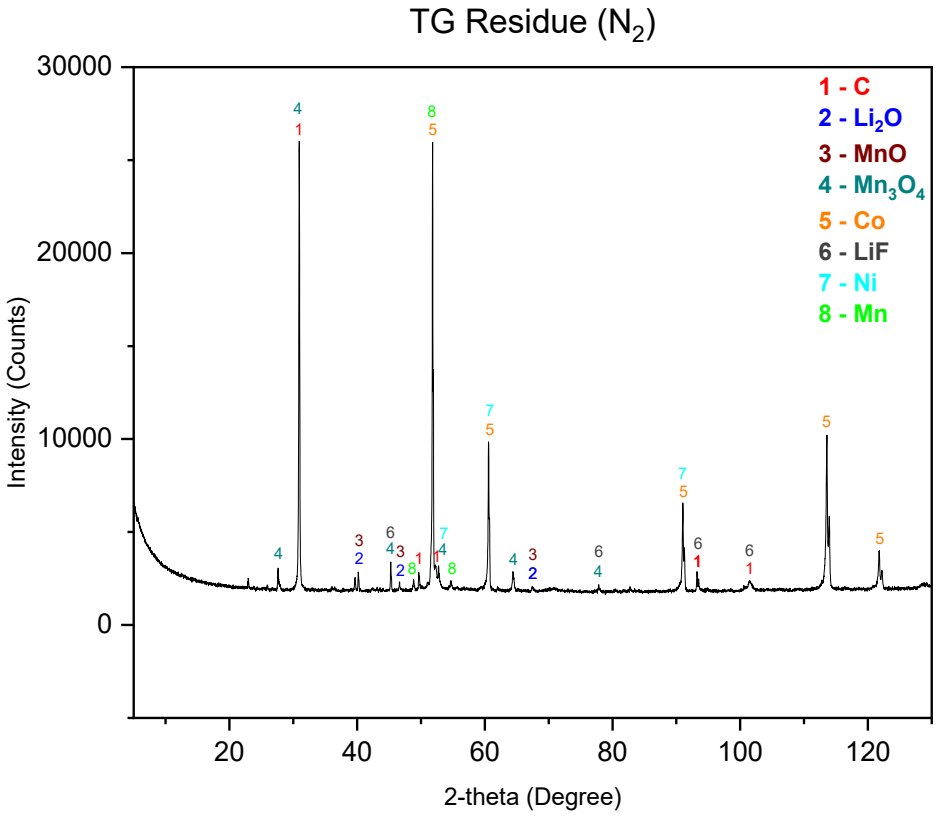

Figure 40: XRD results of the residue from TG analysis in an inert atmosphere.

SEM image (Figure 41) showed that more metallic elements were grouped in an inert atmosphere compared to an air atmosphere. Another difference from the residue taken from the air

atmosphere could be the presence of graphite. We already mentioned that the burning of graphite is less since not enough oxygen is available. The existence of graphite is also established from the EDX graph (figure 42). Peaks of nickel, cobalt, and manganese were perceivable from the spectrum. Other elements such as chlorine, aluminium, phosphorus, and oxygen were detectable as well.

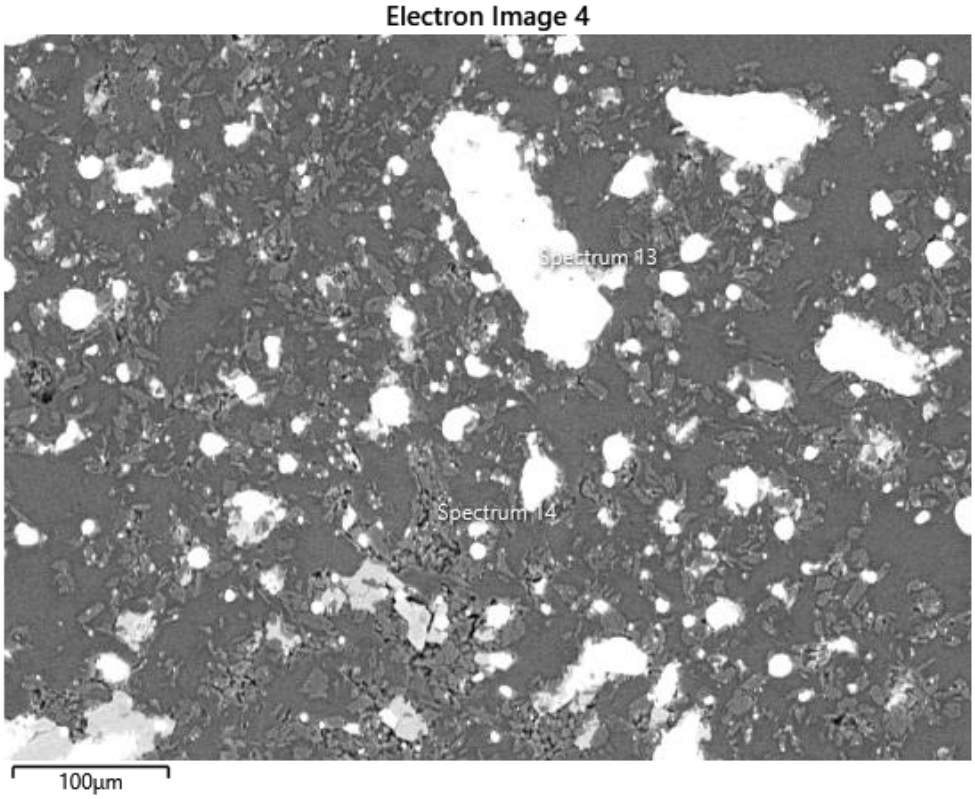

Figure 41: SEM image of TG residue from inert atmosphere.

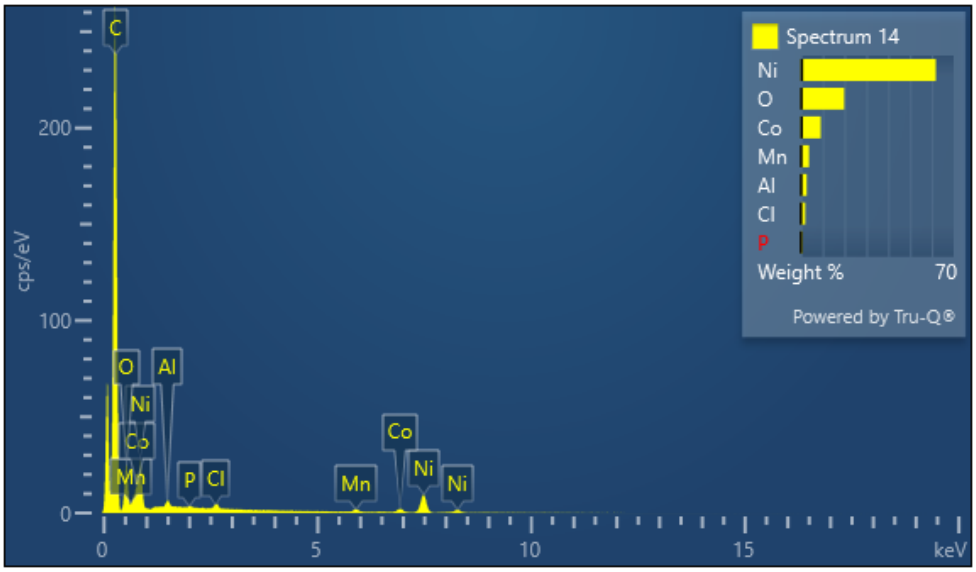

Figure 42: Spectra of TG residue from inert atmosphere.

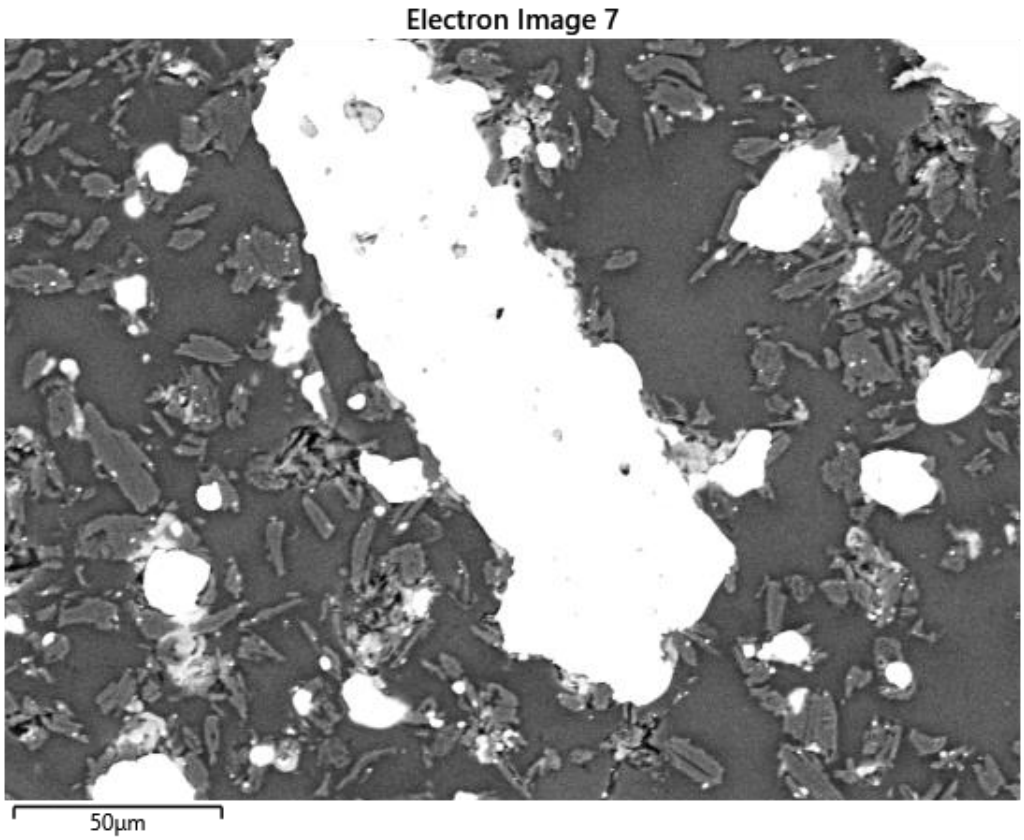

Figure 43: SEM image of TG residue from inert atmosphere at 50 µm magnification.

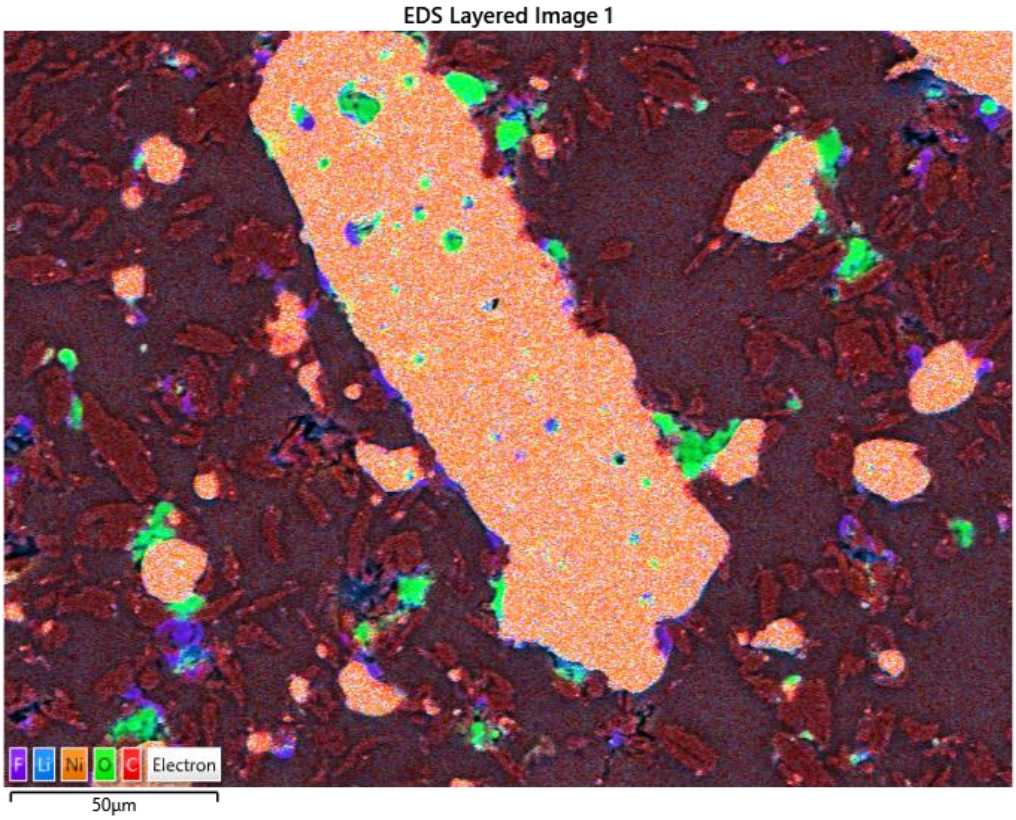

Figure 44: EDX layered image of the TG residue from the inert atmosphere.

Although lithium was not apparent in the EDX analysis, we can figure out the evidence of them being in the sample via elemental mapping (Figure 44. d). Along with lithium, fluorine was also noticed from the mapping results.

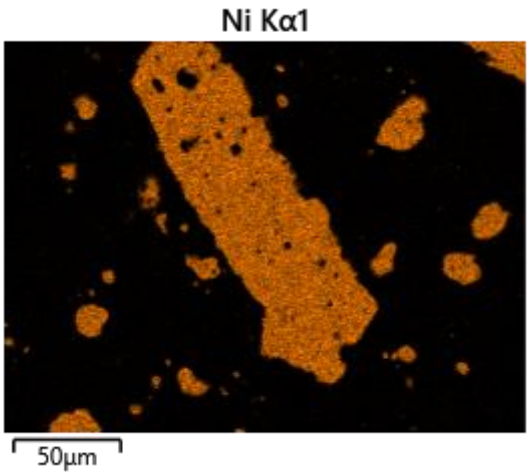

Figure 44. a: EDX mapping of nickel.

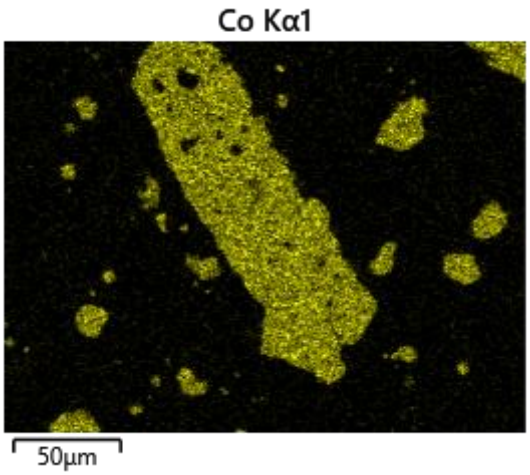

Figure 44. b: EDX mapping of cobalt.

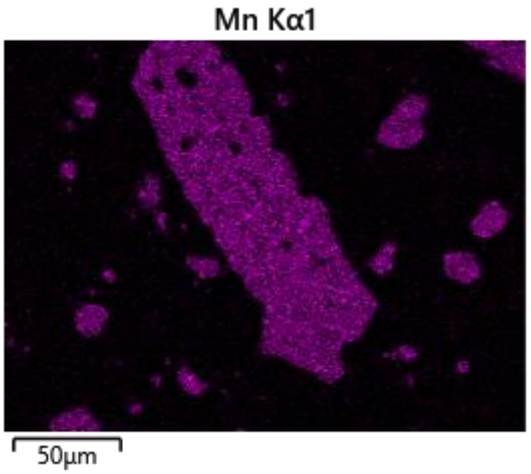

Figure 44. c: EDX mapping of manganese.

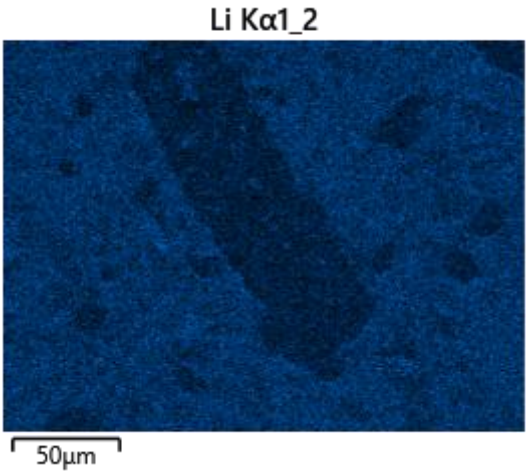

Figure 44. d: EDX mapping of lithium.

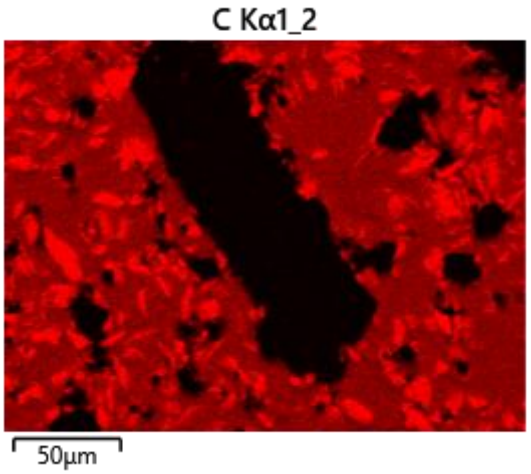

Figure 44. e: EDX mapping of carbon.

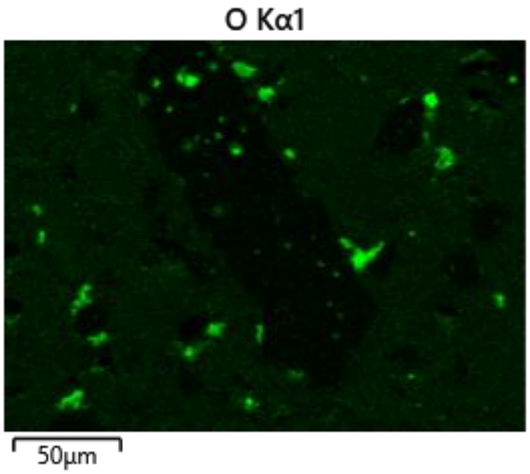

Figure 44. f: EDX mapping of oxygen.

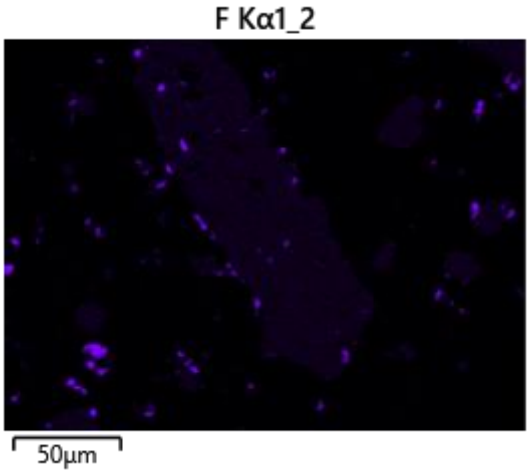

Figure 44. g: EDX mapping of fluorine.

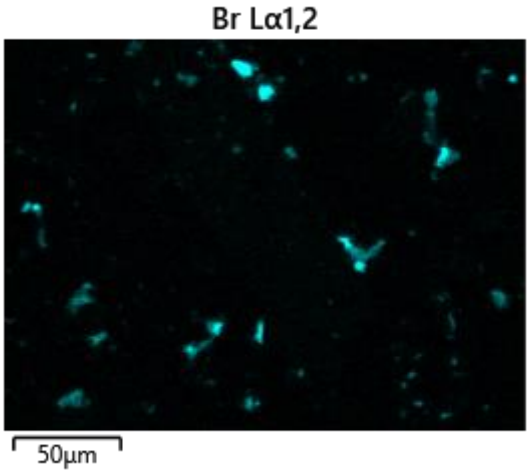

Figure 44. h: EDX mapping of bromine.

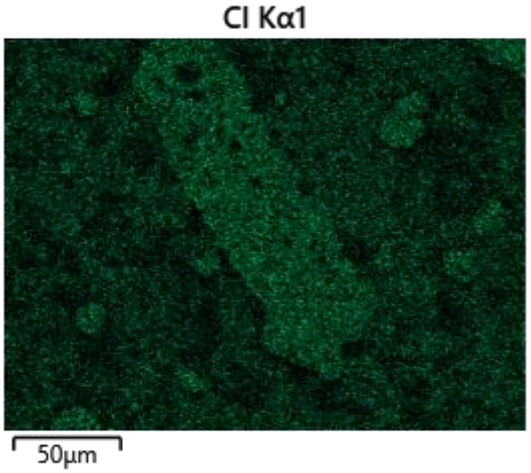

Figure 44. i: EDX mapping of chlorine.

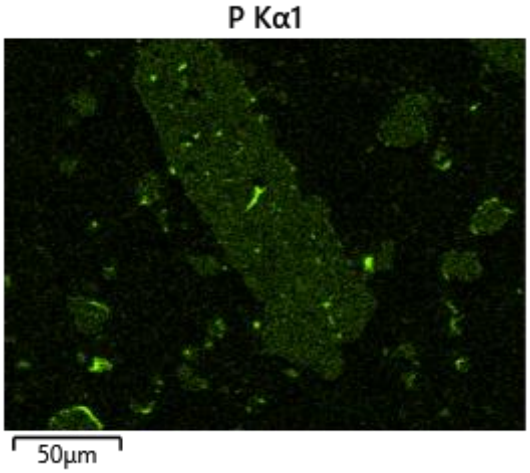

Figure 44. j: EDX mapping of phosphorus.

4.3 Microwave Processing of Black Mass

4.3.1 Behaviour of The Black Mass under Microwave Energy

The temperature profile of the black mass sample concerning time is provided (figure 45). To reach 1200 ℃ it takes just over five minutes. Hence, the heating is very rapid compared to conventional heating. The good microwave absorbing properties of the black mass sample is due to high graphite content, as graphite is classified as excellent microwave absorbers. The profile looks mostly linear apart from some small curves, which means that the microwave-absorbing properties of the materials are mostly unchanged within the varied range of temperatures. Since high temperatures can be achieved using microwave radiation, the required energy would be less compared to other pyrometallurgical heating equipment. We already discussed the microwave heating mechanism and how the materials are heated from the inside to the outside. Thus, volumetric, and selective materials heating can be done which would make the thermal breakdown of the compounds easier. Therefore, the formation of low valence metal oxides and metals from the black mass mixture would be convenient.

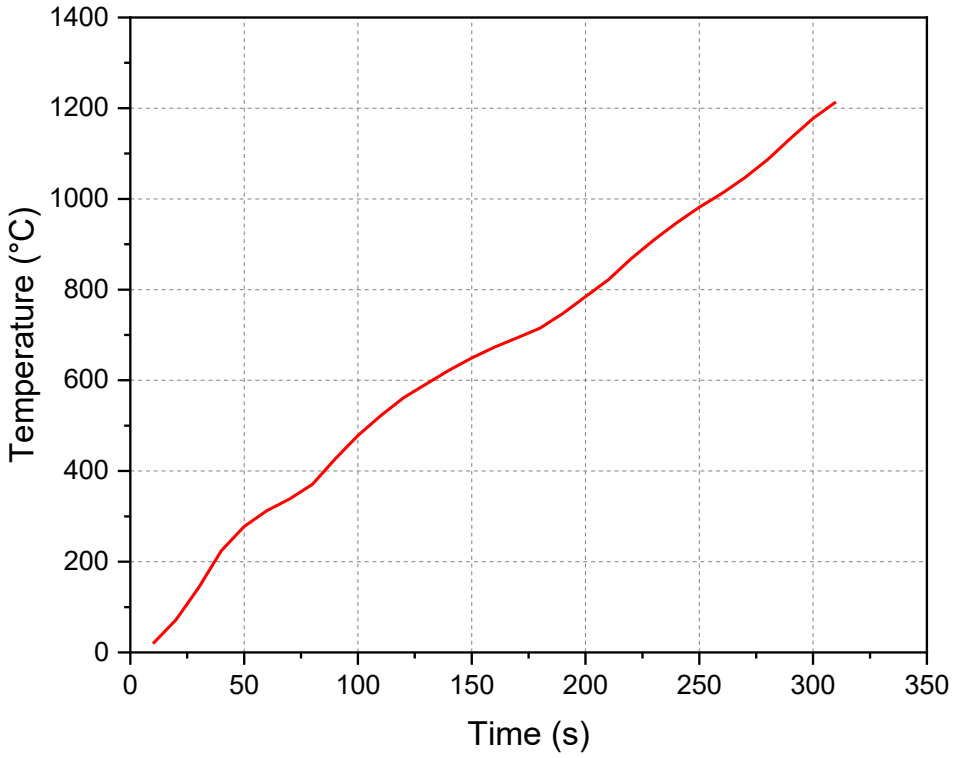

Figure 45: Temperature profile of black mass under microwave radiation at 4 kW.

4.3.2 Effect of Microwave Radiation on The Cathode/Anode Structure

4.3.2.1 Microwave Treatment at 400 ℃

The remainder of the sample after the treatment has some number of small clusters (Figure 46) unlike the raw sample which was finer. In the XRD results (Figure 47), the metallic peaks are distinguishable. The peaks at 52.16º, 61º, 91.7º, 114,6º, and 122.88º of the 2-theta value indicate the formation of nickel and cobalt even at that low-temperature treatment as compared to conventional thermal treatment. Also, some metal oxides were formed, such as NiO and Mn_3O_4. Significant amounts of graphite were present in the sample as well as lithium carbonate.

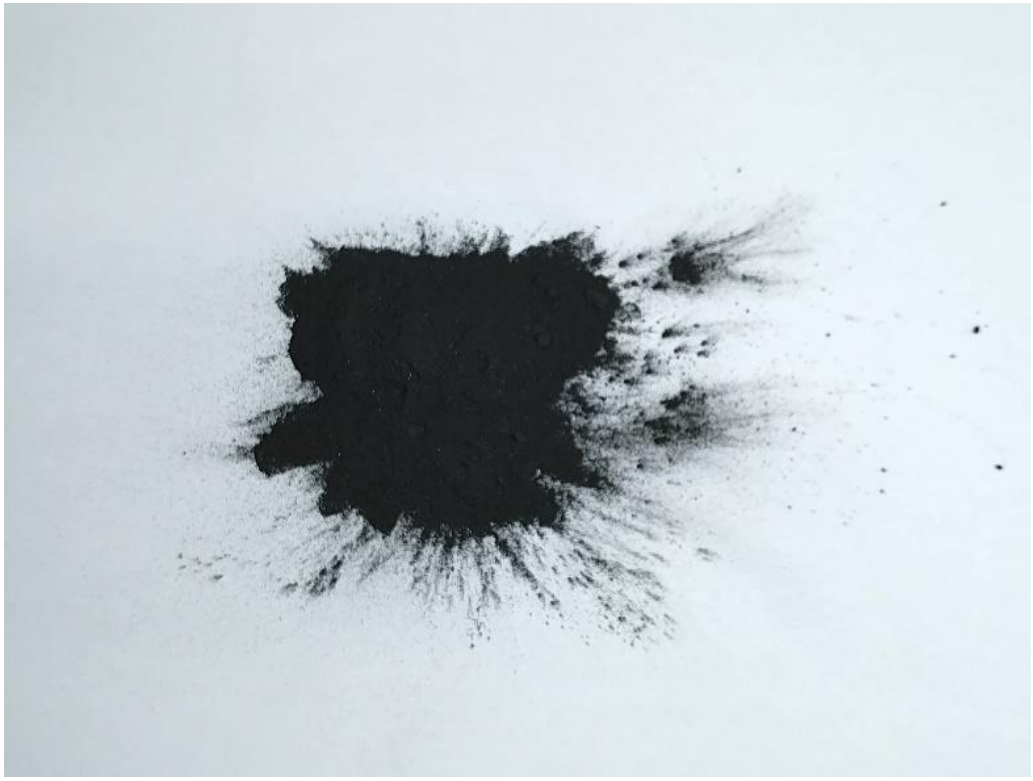

Figure 46: Sample's image after microwave treatment at 400 ℃.

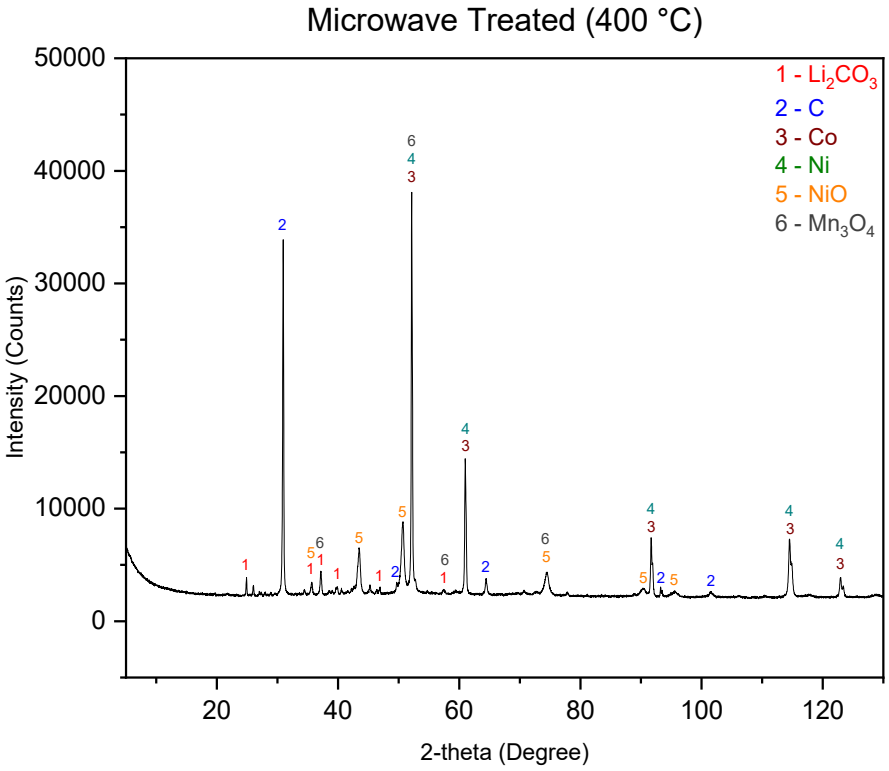

Figure 47: XRD graph of the sample after microwave treatment at 400 ℃.

From the SEM image (figure 48), we can understand that the flakes-like graphite structure was also present with bright spots, indicating metallic elements have increased compared to the untreated sample. EDX results (Figure X) give us the elements present in the sample which is mostly like the raw sample. From the spectrum, we can see the presence of nickel, cobalt, manganese, graphite, aluminium, phosphorus, calcium, and oxygen.

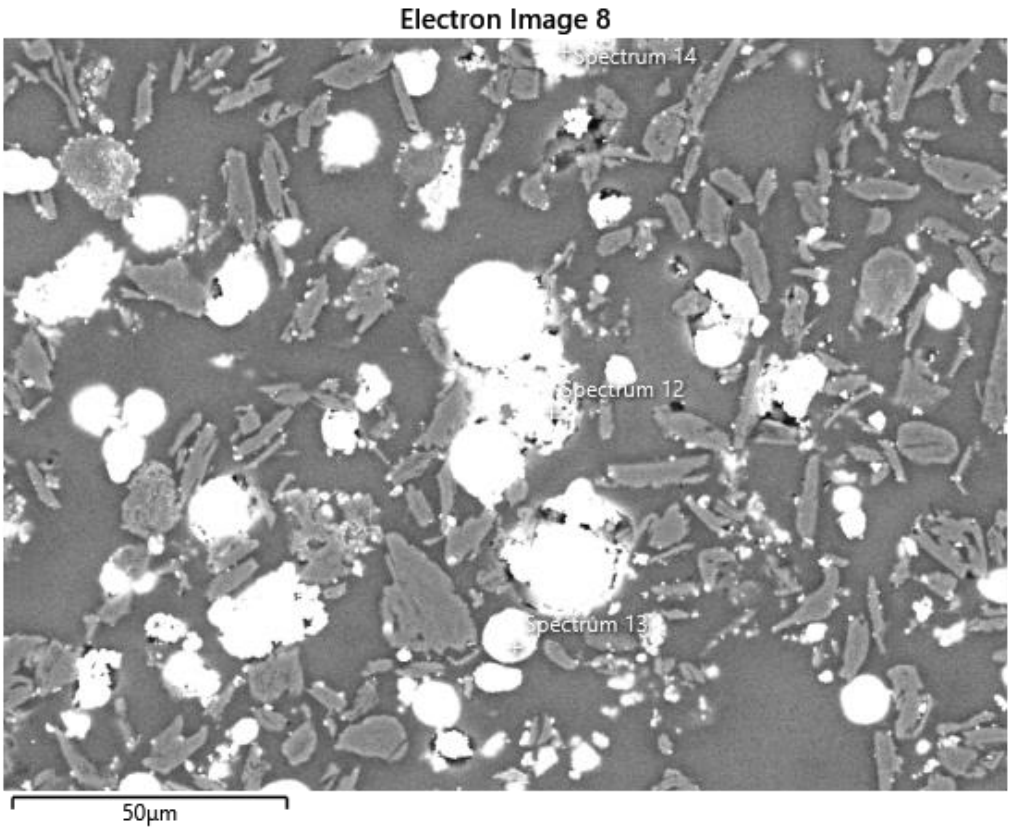

Figure 48: SEM image of the sample after microwave treatment at 400 ℃.

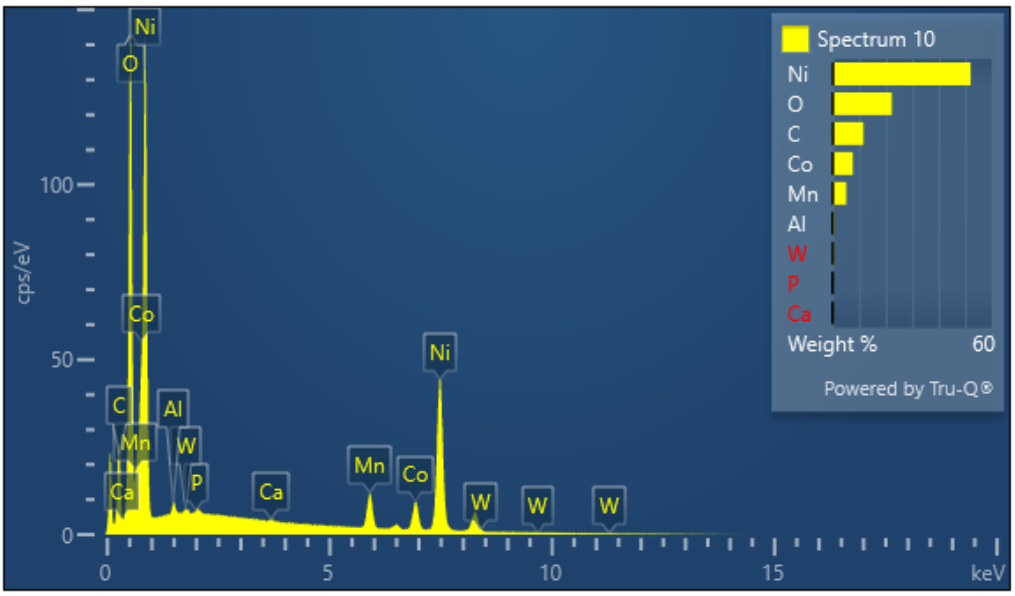

Figure 49: EDX spectra of the sample after microwave treatment at 400 ℃.

Mapping also shows the distribution of graphite. Also, we can understand that there are several metal oxides present in the residue by looking at position of oxygen and metals. We can also see that some fluorine and chlorine remained after roasting at 400 ℃.

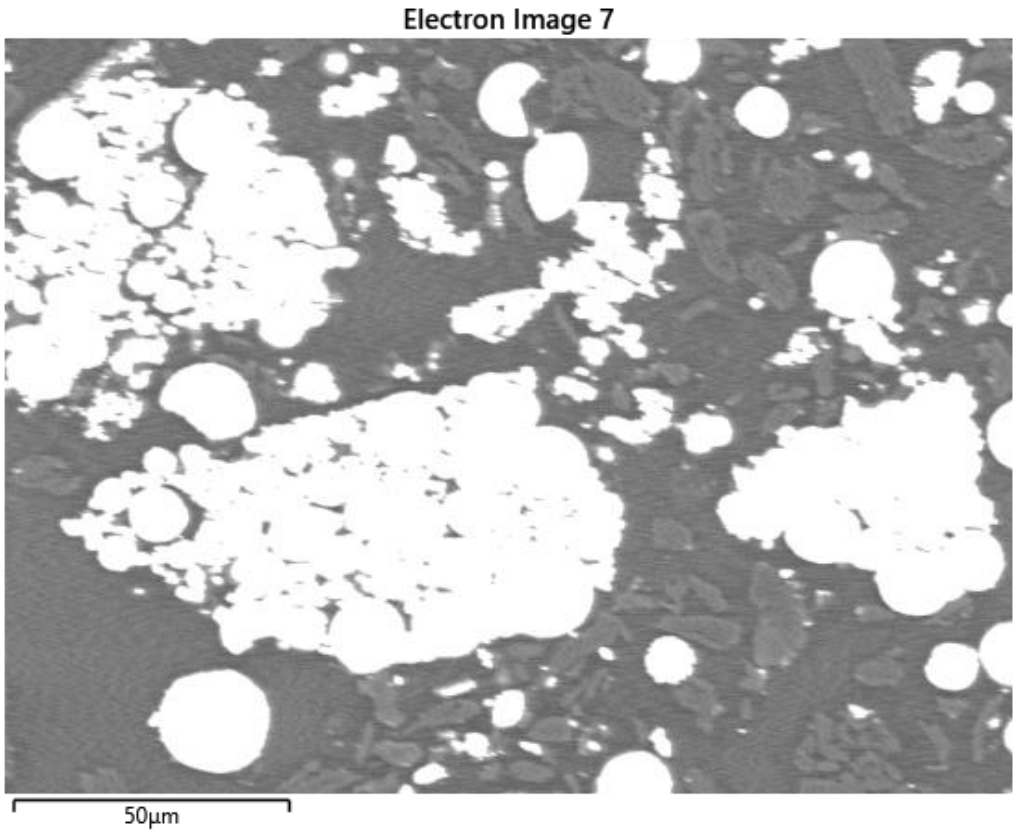

Figure 50: SEM image of the sample after microwave treatment at 400 ℃ at 50 µm magnification.

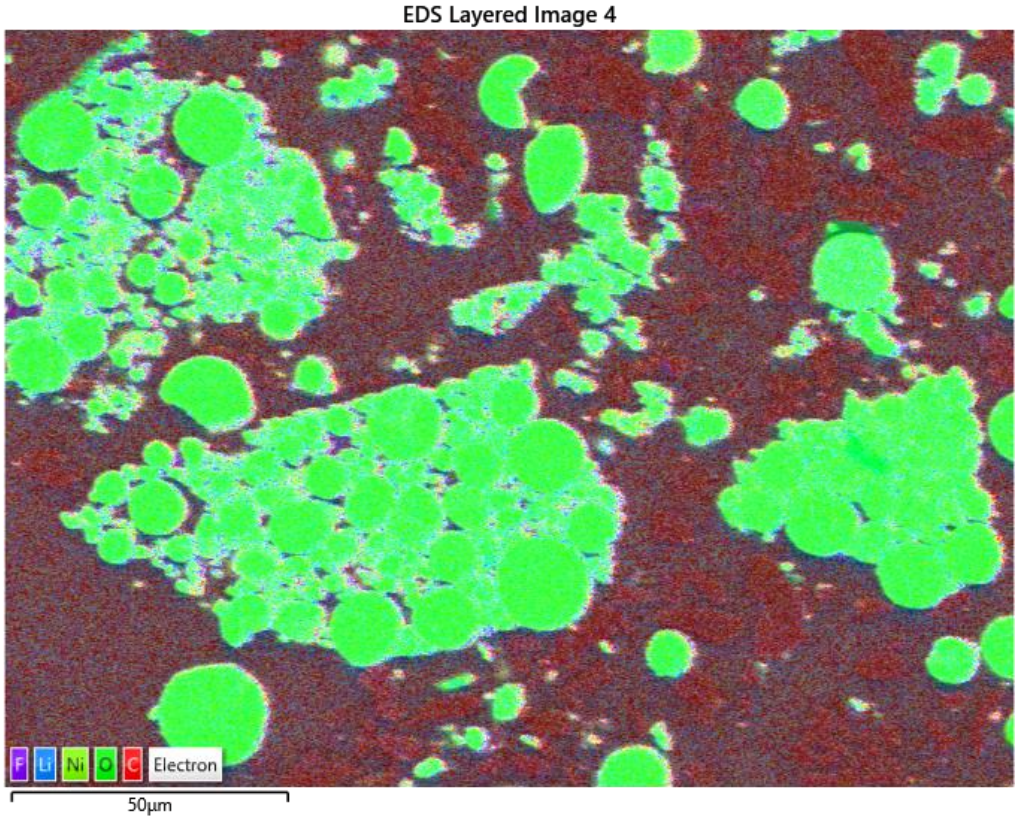

Figure 51: EDX layered image of the sample after microwave treatment at 400 ℃.

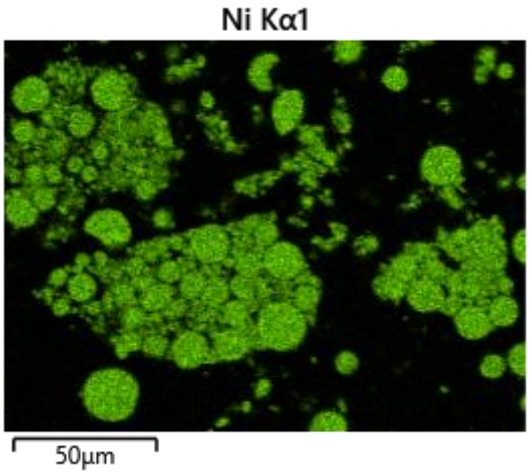

Figure 51. a: EDX mapping for nickel.

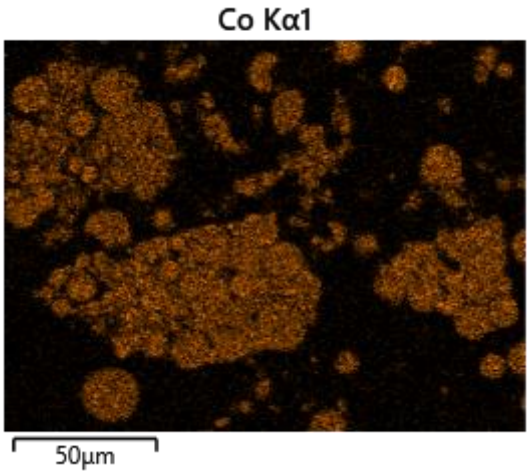

Figure 51. b: EDX mapping for cobalt.

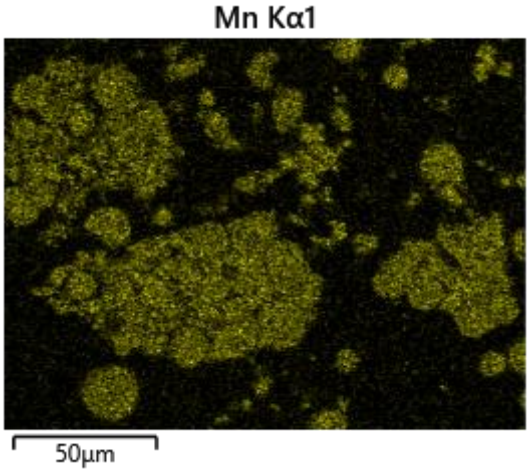

Figure 51. c: EDX mapping for manganese.

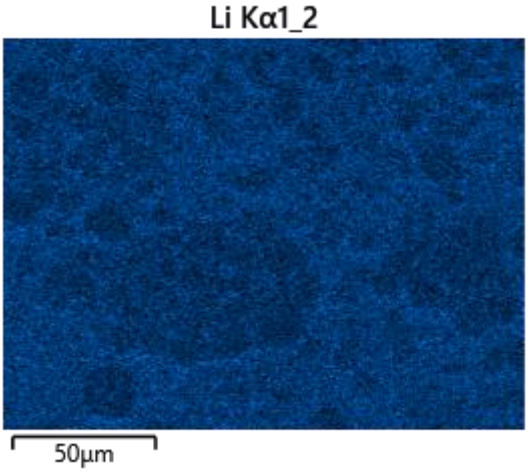

Figure 51. d: EDX mapping for lithium.

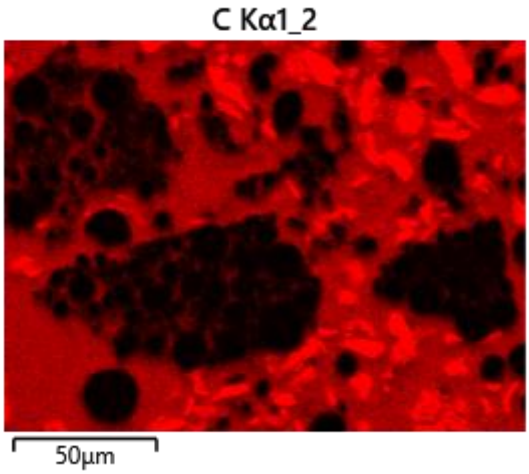

Figure 51. e: EDX mapping for carbon.

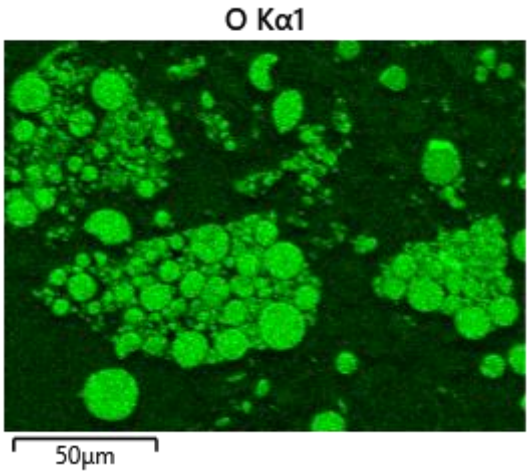

Figure 51. f: EDX mapping for oxygen.

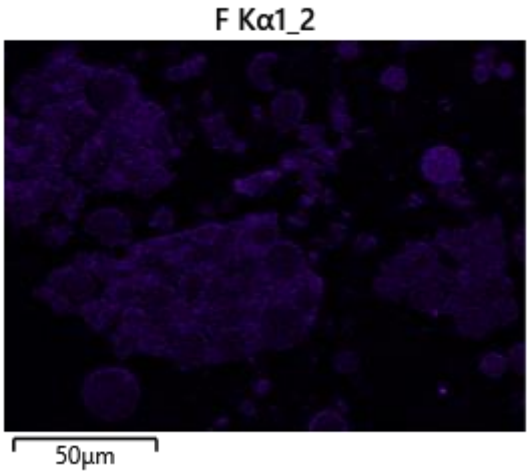

Figure 51. g: EDX mapping for fluorine.

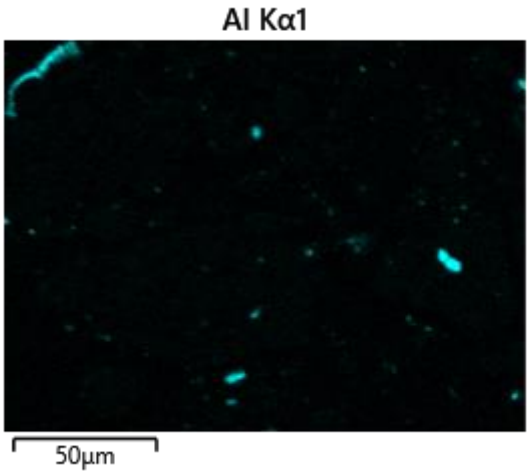

Figure 51. h: EDX mapping for aluminium.

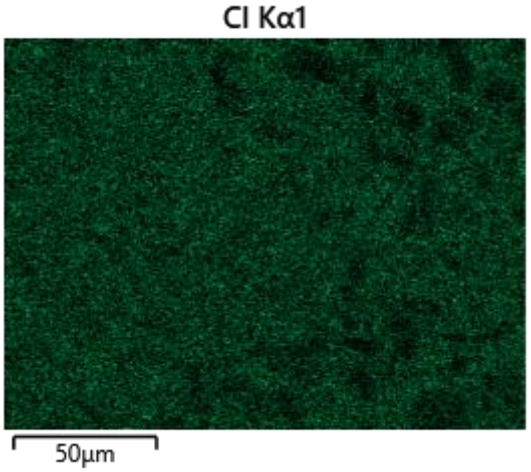

Figure 51. i: EDX mapping for chlorine.

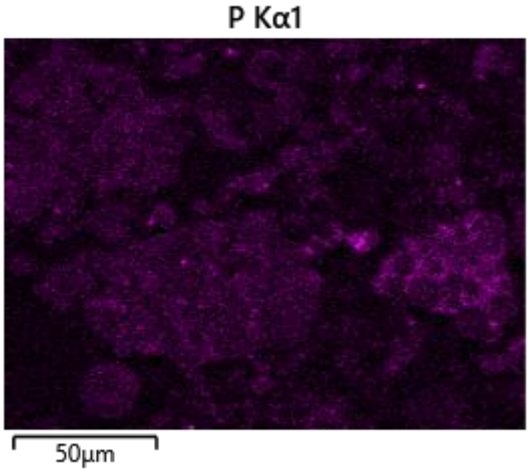

Figure 51. j: EDX mapping for phosphorus.

4.3.2.2 Microwave Treatment at 600 ℃

The number of agglomerations increased after this stage (figure 52). Similar to the previous experiment at 400 °C, the metallic phases of nickel and cobalt are visible from the XRD graph (figure 53), but with higher intensity. No significant shift in the phase of graphite can be observed and the phase of lithium carbonate is present. Along with nickel oxide, the formation of cobalt oxide happens during this temperature range. Though peaks of Mn_3O_4 can be seen, a transformation to MnO_2 also occurred.

Figure 52: Sample's image after microwave treatment at 600 ℃.

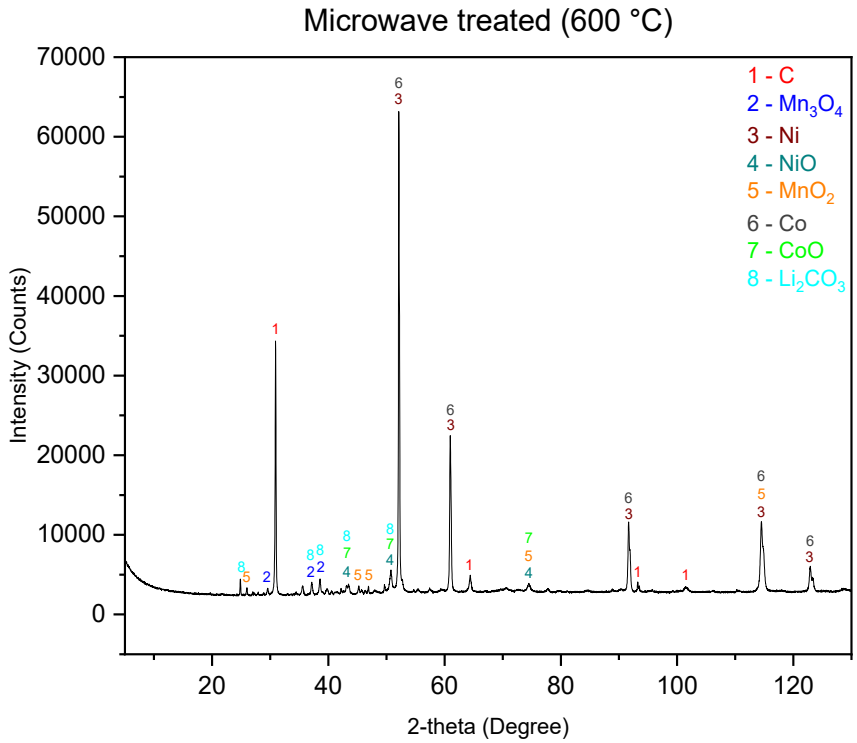

Figure 53: XRD graph of the sample after microwave treatment at 600 ℃.

Again, in the SEM image (Figure 54), we can see the amount of graphite is reducing, suggesting the formation of carbon dioxide and carbon monoxide gases while the breaking down of the cathodic structure is going on. Bigger clusters of bright spots are visible from that image, indicating the formation of metallic compounds. The EDX graph (Figure 55) also confirms the present elements within the treated sample. Other metallic elements, such as Co, Ni, and Mn could be located. Sulphur, phosphorus, oxygen, and graphite were traced via an EDX graph.

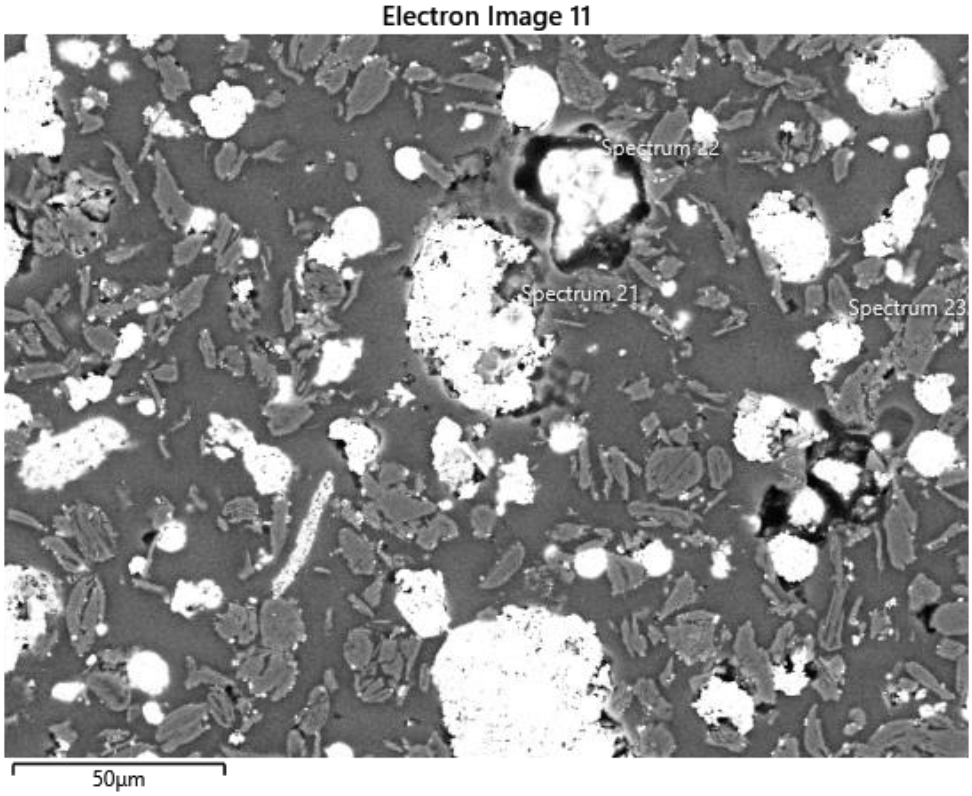

Figure 54: SEM image of the sample after microwave treatment at 600 ℃.

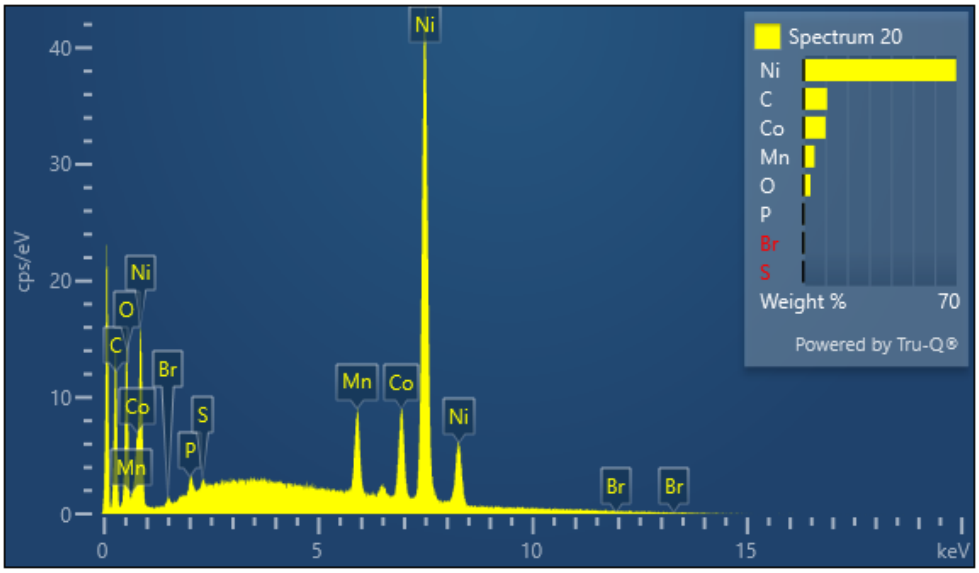

Figure 55: EDX spectra of the sample after microwave treatment at 600 ℃.

To find out the missing elements, we investigated the elemental mapping again. Here, lithium could be observed. Some elements that were not noted in the EDX graph was also observed in the elemental mapping. Hence, aluminium, fluorine, chlorine, and copper were noticeable in the mapping images which was also present in the raw sample.

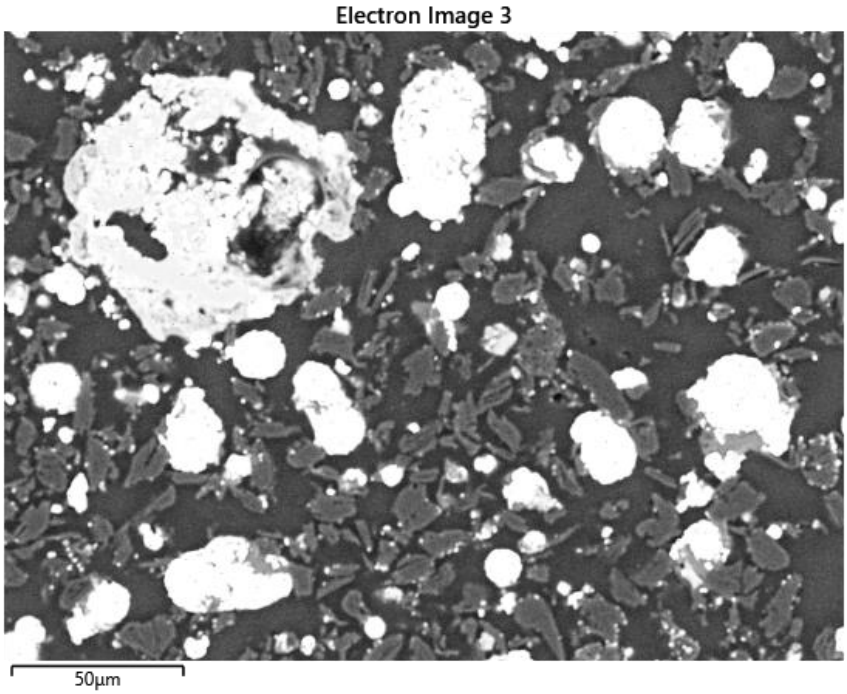

Figure 56: SEM image of the sample after microwave treatment at 600 ℃ at 50 µm magnification.

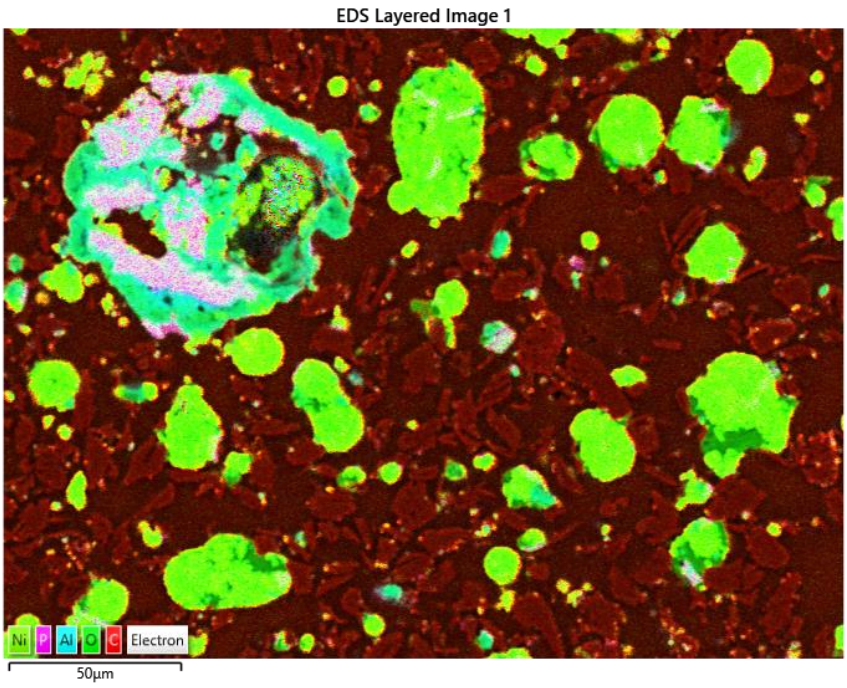

Figure 57: EDX layered image of the sample after microwave treatment at 600 ℃.

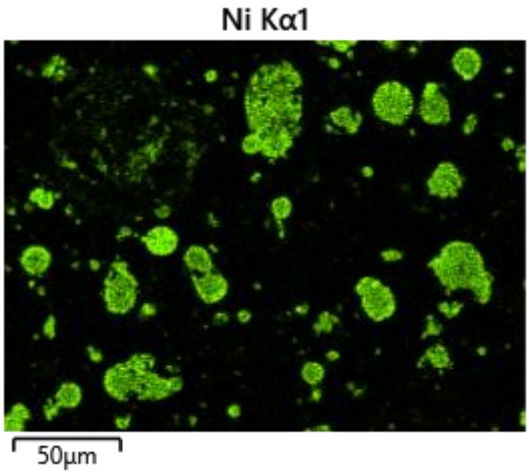

Figure 57. a: EDX mapping for nickel.

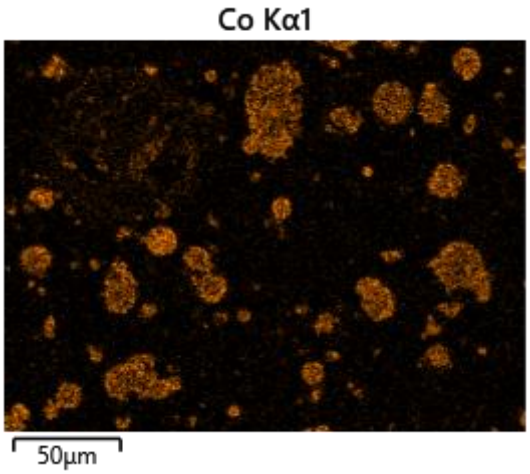

Figure 57. b: EDX mapping for cobalt.

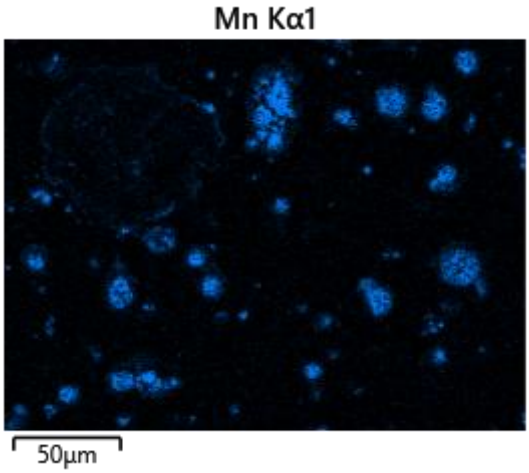

Figure 57. c: EDX mapping for manganese.

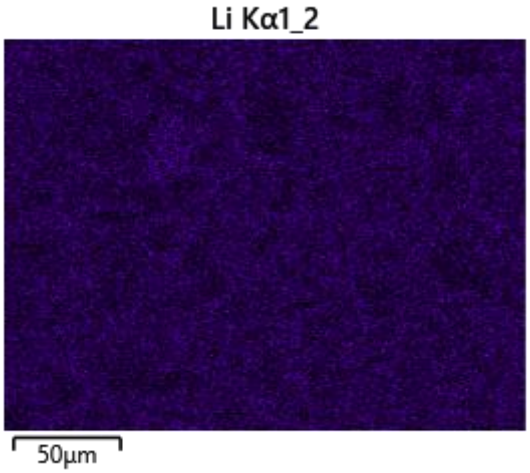

Figure 57. d: EDX mapping for lithium.

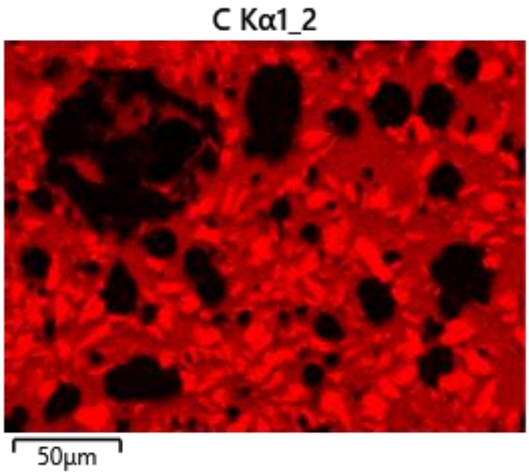

Figure 57. e: EDX mapping for carbon.

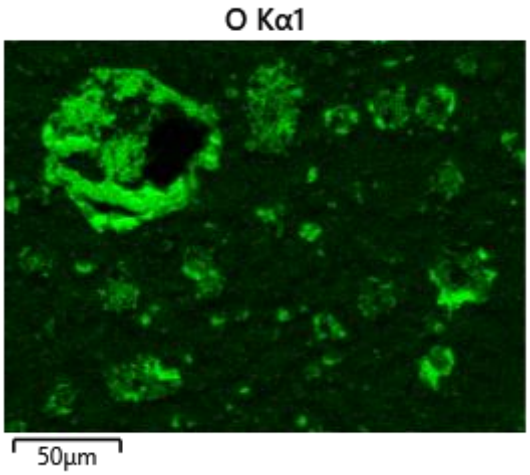

Figure 57. f: EDX mapping for oxygen.

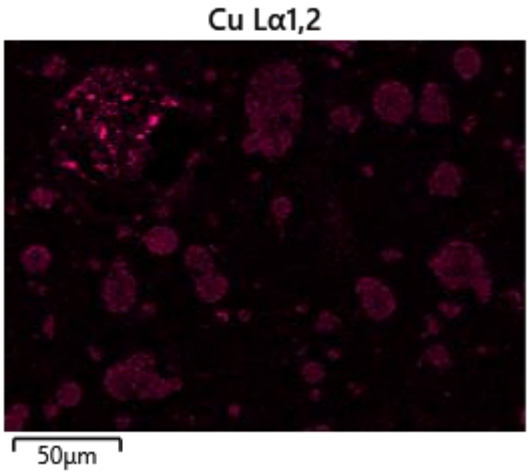

Figure 57. g: EDX mapping for copper.

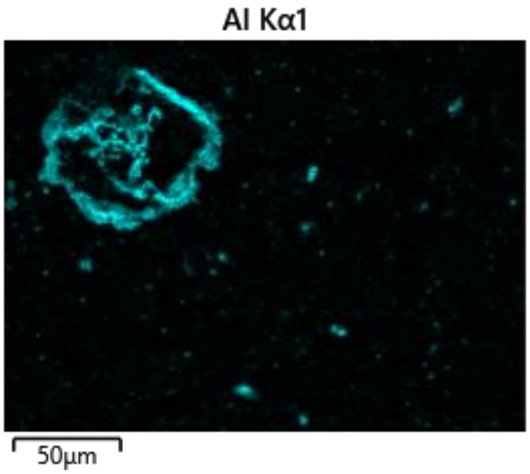

Figure 57. h: EDX mapping for aluminium.

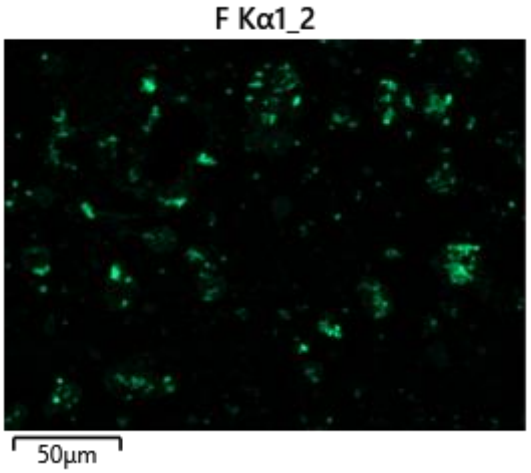

Figure 57. i: EDX mapping for fluorine.

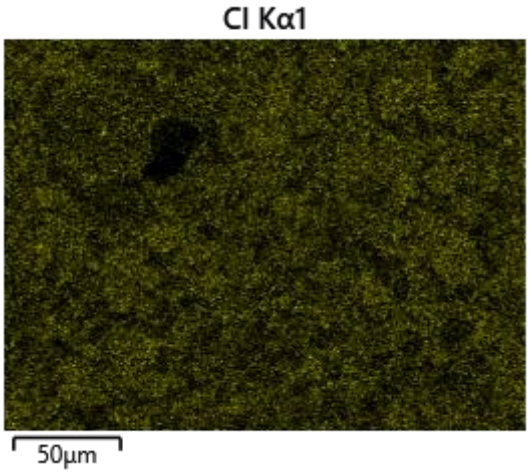

Figure 57. j: EDX mapping for chlorine.

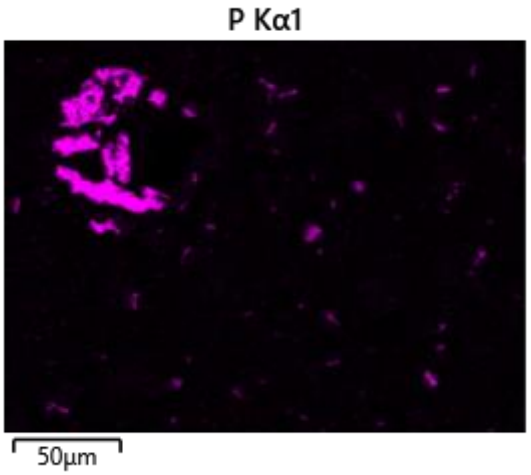

Figure 57. k: EDX mapping for phosphorus.

4.3.2.3 Microwave Treatment at 800 ℃

The sample after the treatment shows increased agglomeration in comparison to lower temperature (Figure 58). So far it signifies that the higher temperature increases the reaction between the elements and the metallic cluster formation increases because of that phenomenon. The XRD graph (Figure 59) also depicts similar results as the previous two treatments. Compared to the samples from 600 ℃ treatments, here, the intensity of the metal phases is slightly reduced. Graphite peaks are almost identical and small peaks of lithium carbonate are visible too. The formation of manganese metal took place while the vanishing of the Mn_3O_4 phase was a significant change. However, two other phases of manganese oxides namely MnO, and MnO_2 are available. Apart from metallic nickel, and cobalt, peaks of their oxides also emerged.

Figure 58: XRD graph of the sample after microwave treatment at 800 ℃.

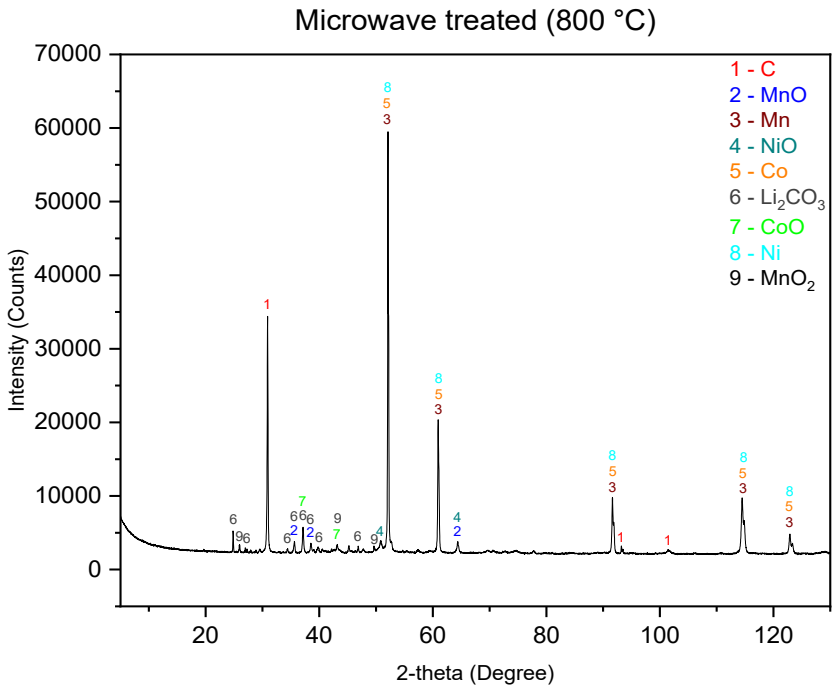

Figure 59: XRD graph of the sample after microwave treatment at 800 ℃.

SEM image (Figure 60) shows the scenario after microwave treatment at 800 ℃. The area covering the metals and metallic compounds has increased while the portion of graphite decreased slightly. We can also observe this situation from the elemental mapping images (Figure 63. a to 63. j). The EDX graph (Figure 61) shows the peaks of nickel, cobalt, oxygen, graphite, and manganese.

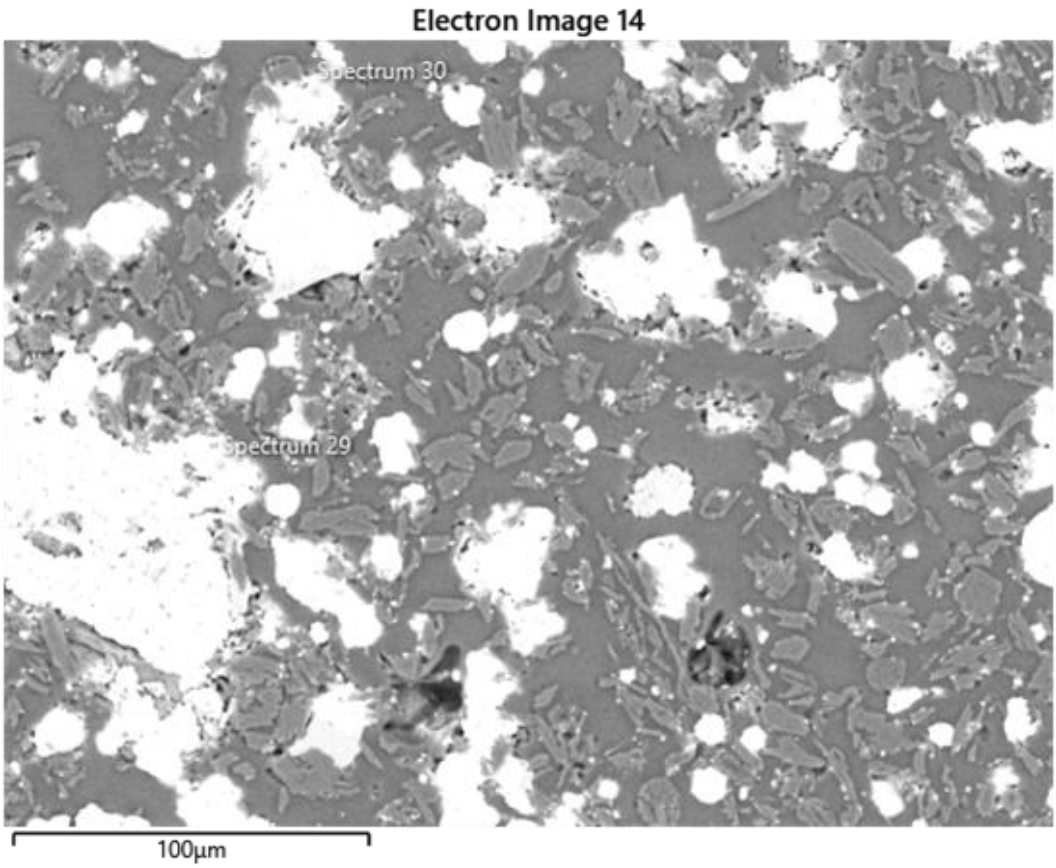

Figure 60: SEM image of the sample after microwave treatment at 800 ℃.

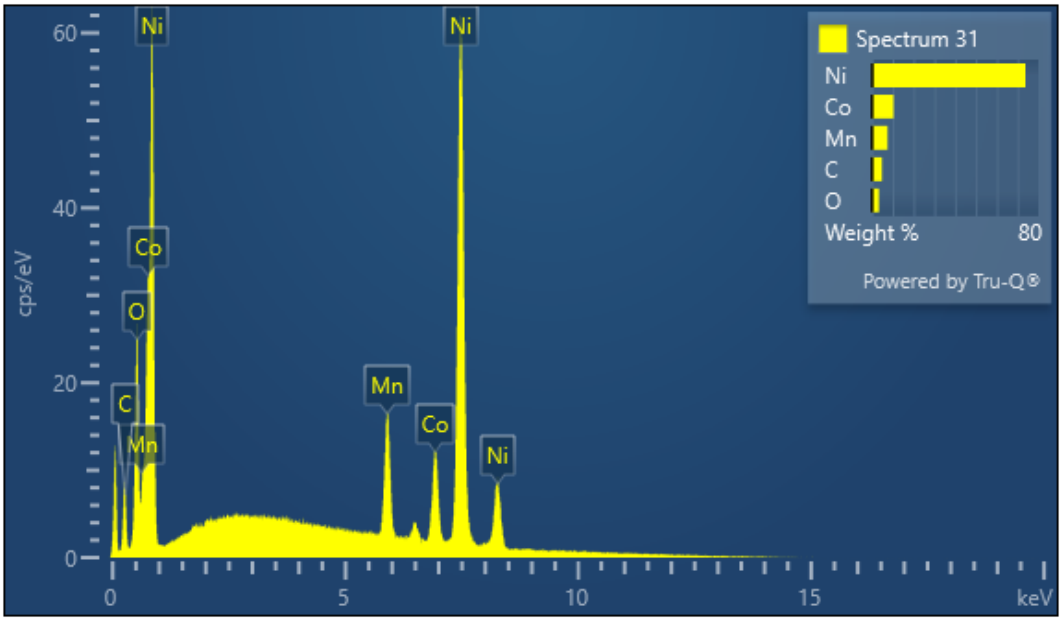

Figure 61: EDX spectra of the sample after microwave treatment at 800 ℃.

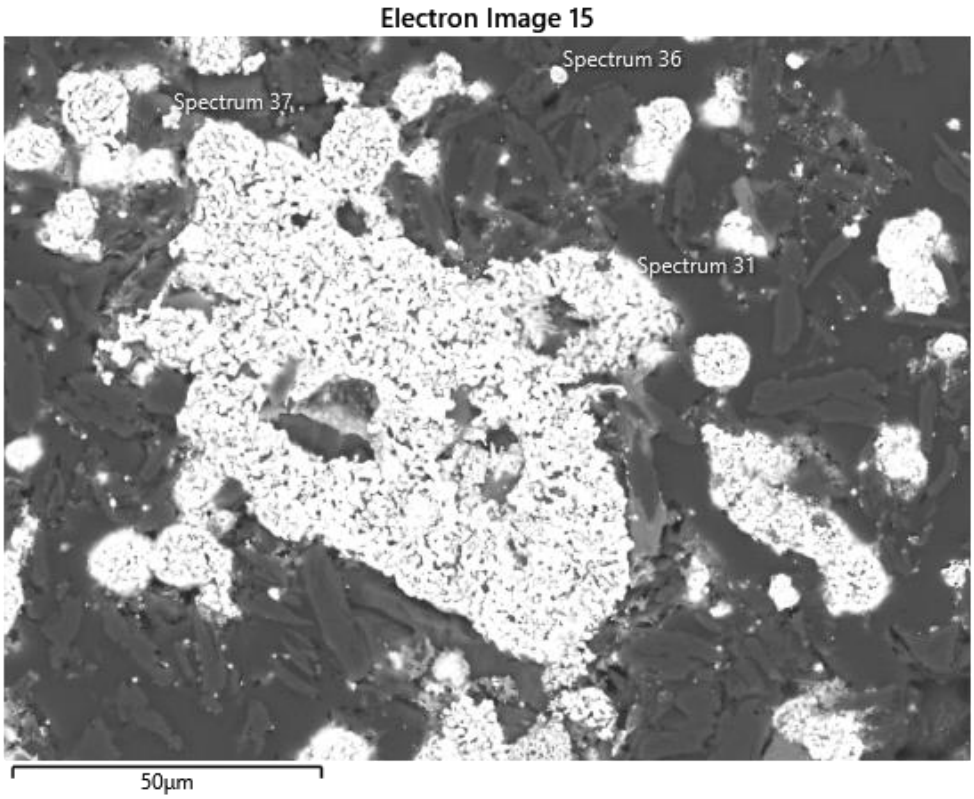

Figure 62: SEM image of the sample after microwave treatment at 800 ℃ at 50 µm magnification.

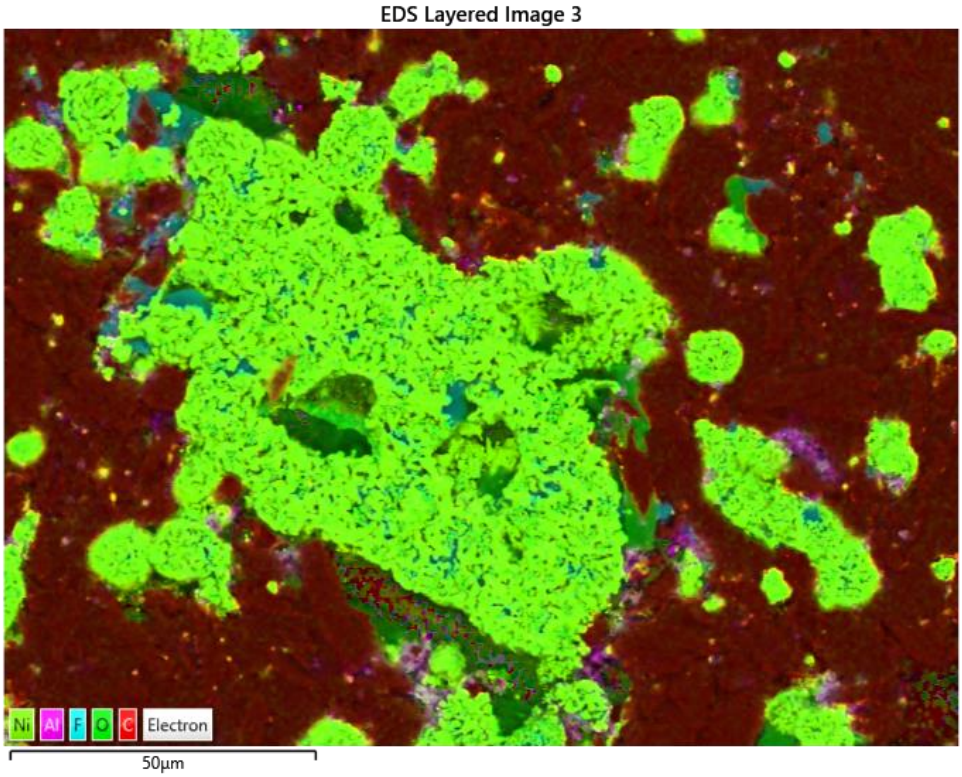

Figure 63: EDX layered image of the sample after microwave treatment at 800 ℃.

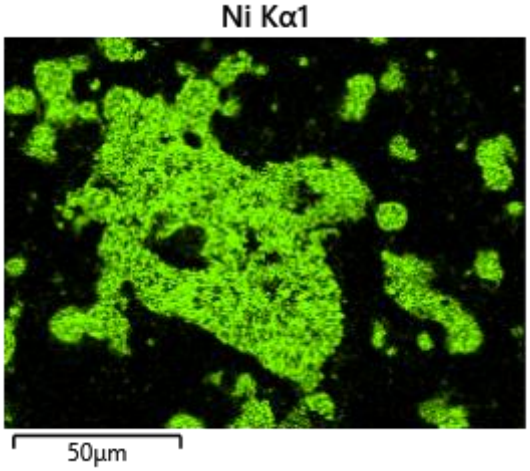

Figure 63. a: EDX mapping for nickel.

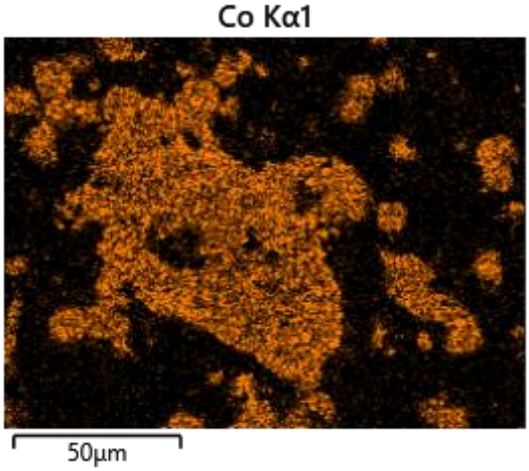

Figure 63. b: EDX mapping for cobalt.

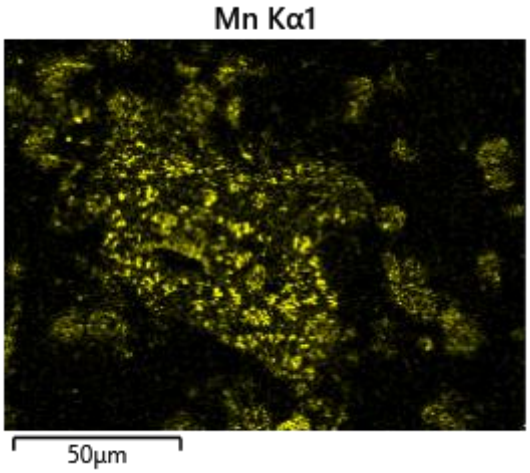

Figure 63. c: EDX mapping for manganese.

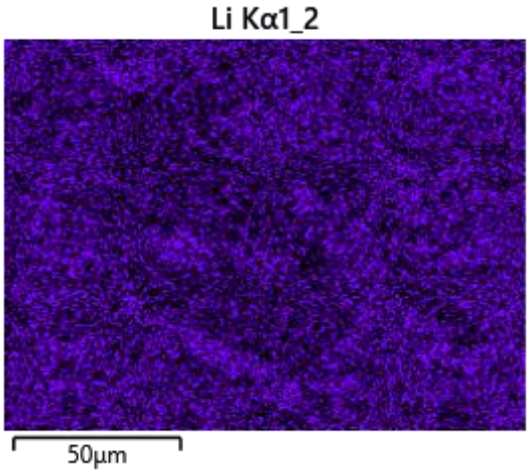

Figure 63. d: EDX mapping for lithium.

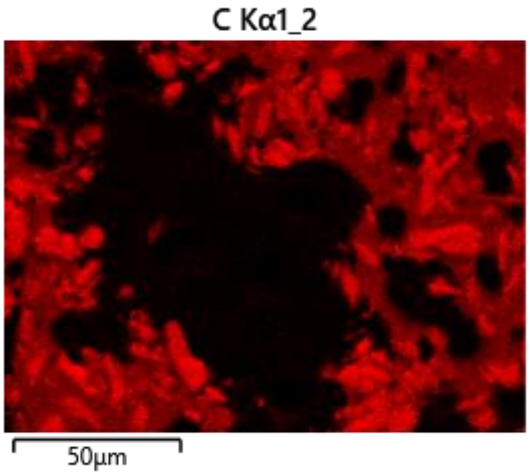

Figure 63. e: EDX mapping for carbon.

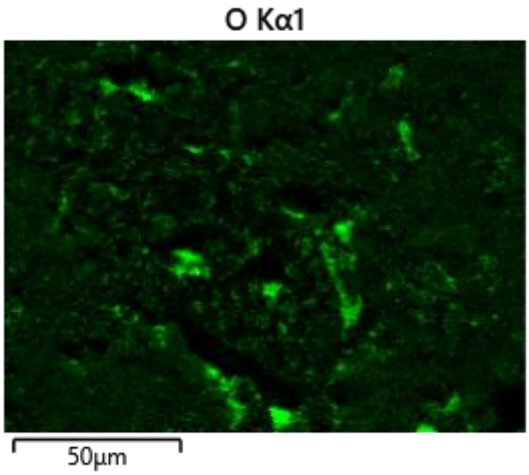

Figure 63. f: EDX mapping for oxygen.

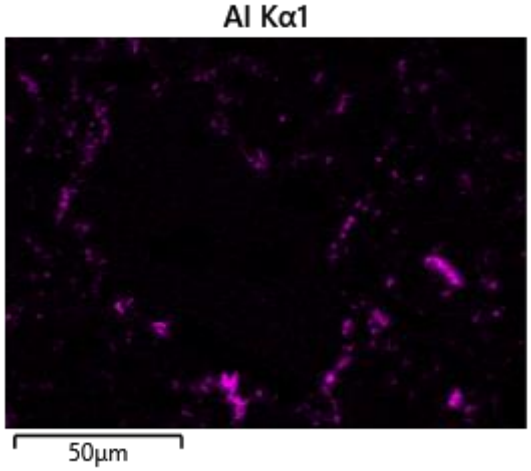

Figure 63. g: EDX mapping for aluminium.

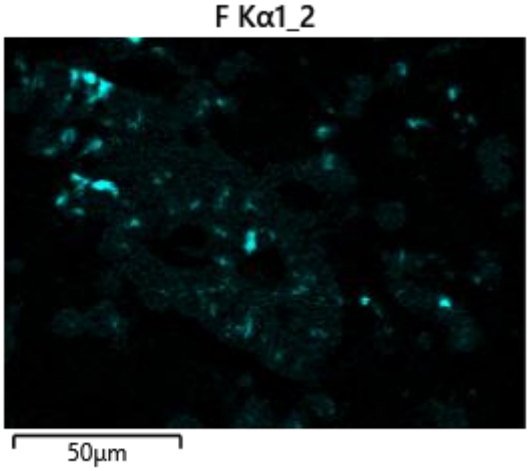

Figure 63. h: EDX mapping for fluorine.

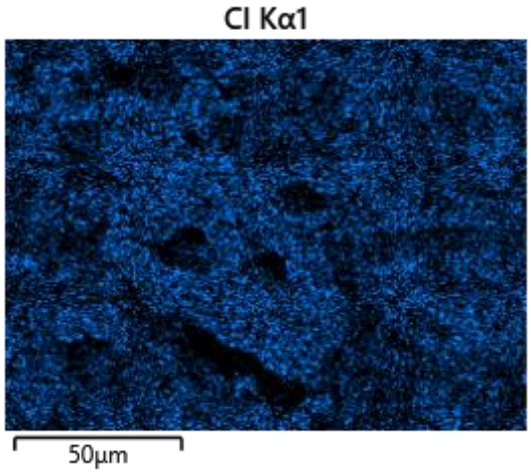

Figure 63. i: EDX mapping for chlorine.

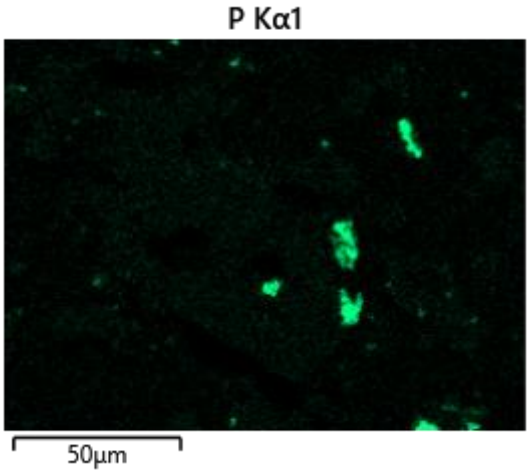

Figure 63. j: EDX mapping for phosphorus.

From the first image, we can see that graphite flakes they were situated around a relatively big metallic cluster. Lithium is distributed evenly throughout the sample and bright spots of oxygen can be seen in between the metallic cluster which can be the metallic oxides of cobalt, nickel, and manganese. Traces of aluminium, fluorine, chlorine, and phosphorus are still present which may have remained even after being treated at this temperature.

4.3.2.4 Microwave Treatment at 1000 ℃

The clump has again increased after this stage of treatment which can be seen from the image of the sample (Figure 64). Little change can be observed from the XRD graphs (figure 65). Phases of graphite and lithium carbonate are quite unchanged. Only lower valance metal oxides have detectable peaks along with their metallic phases.

Figure 64: Sample's image after microwave treatment at 1000 ℃.

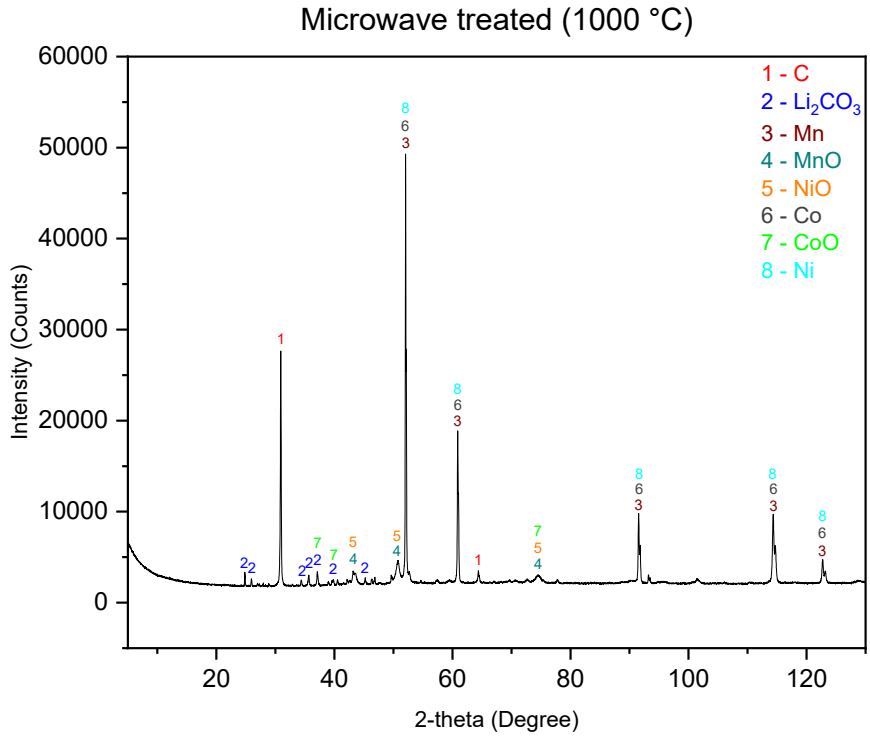

Figure 65: XRD graph of the sample after microwave treatment at 1000 ℃.

SEM image (Figure 66) shows a bigger agglomeration of metallic elements after being treated at 1000 ℃. Like the previous experiment, flakes-shaped graphite particles are resting at the surroundings of that cluster. However, there are some visible dark spots and boundaries inside the cluster. The main elements graphite, oxygen, manganese, cobalt, and nickel were detected from the EDX graph (Figure 67).

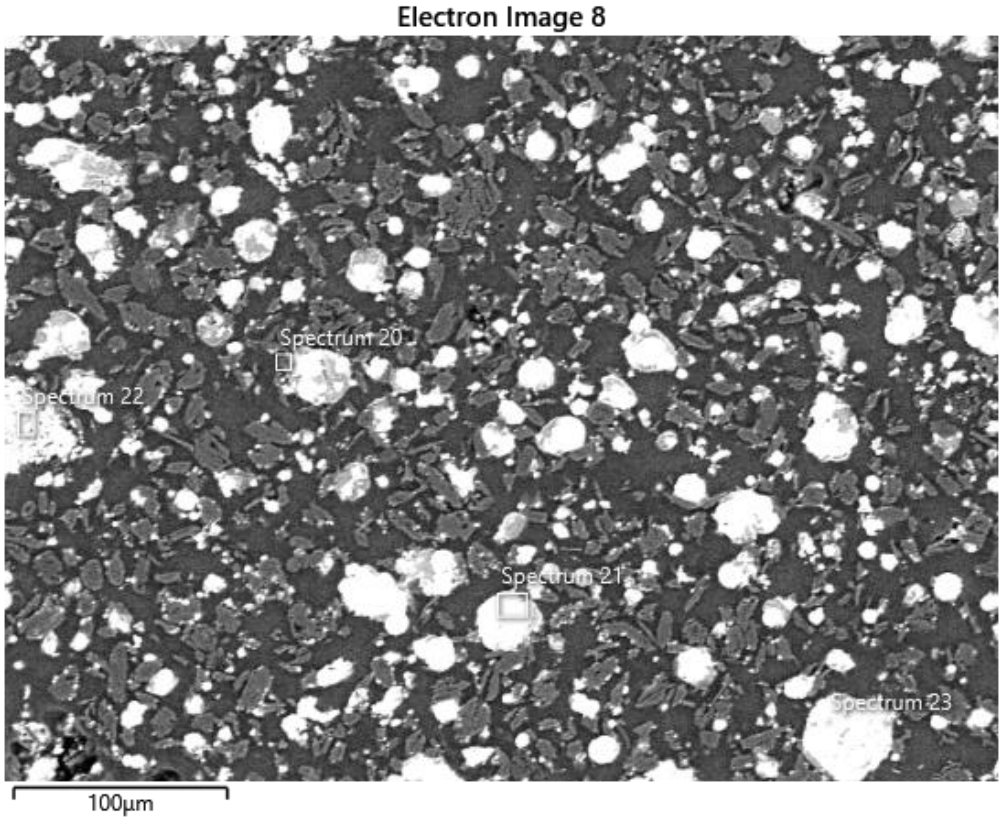

Figure 66: SEM image of the sample after microwave treatment at 1000 ℃.

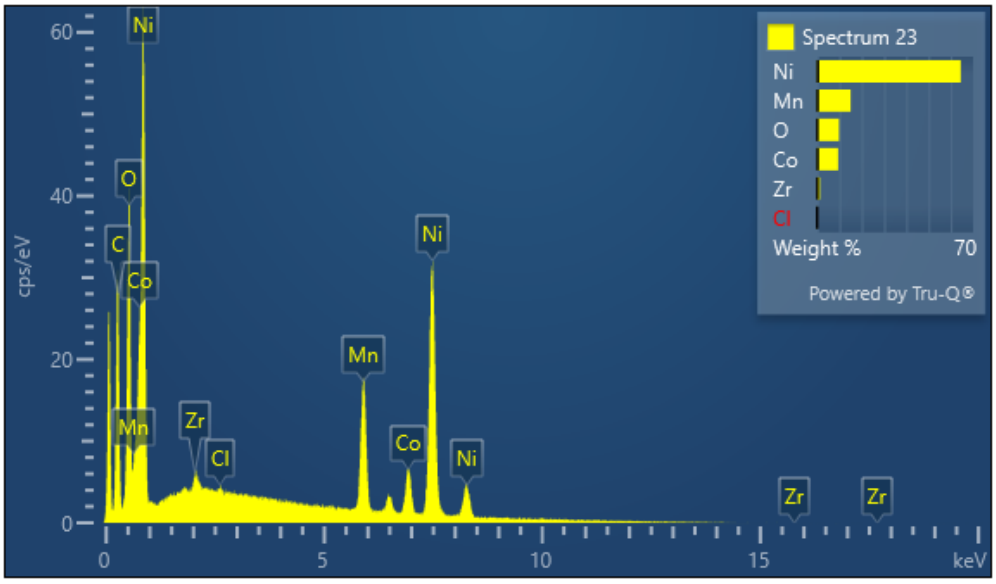

Figure 67: EDX spectra of the sample after microwave treatment at 1000 ℃.

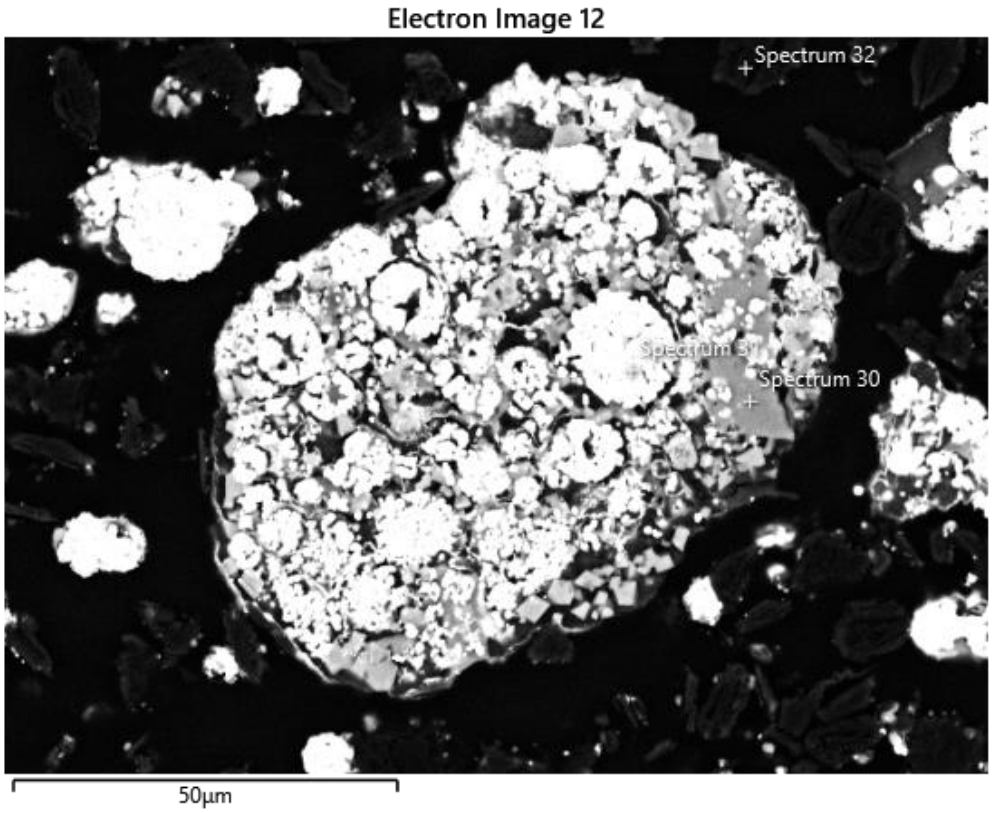

Figure 68: SEM image of the sample after microwave treatment at 1000 ℃ at 50 µm magnification.

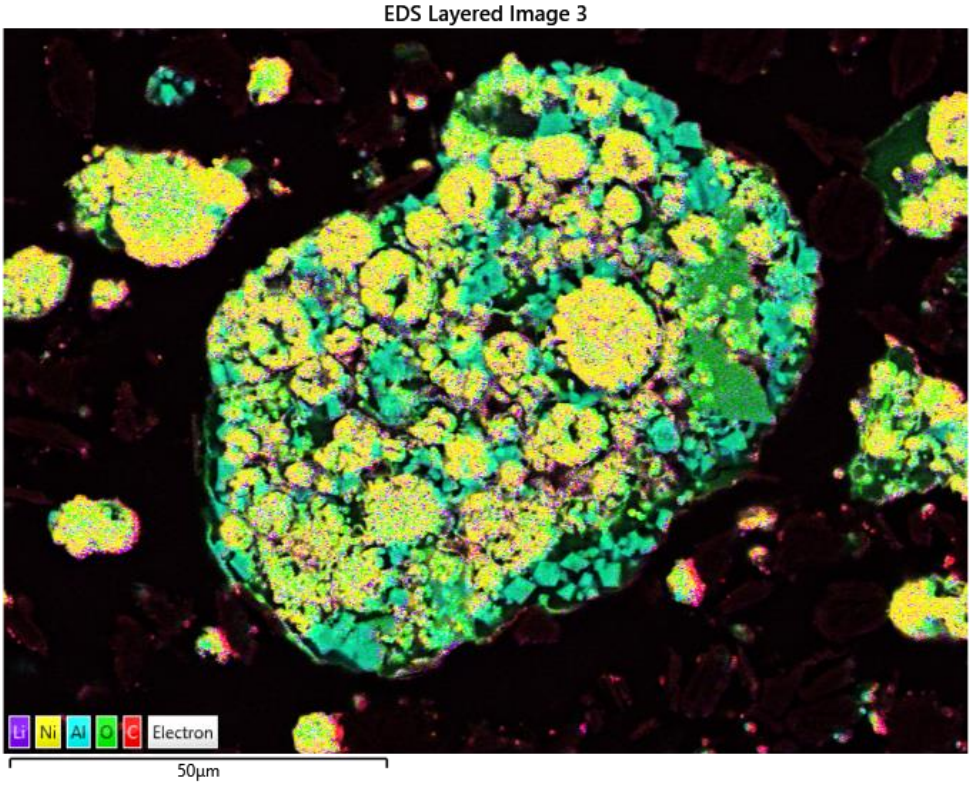

Figure X: EDX layered image of the sample after microwave treatment at 1000 ℃.

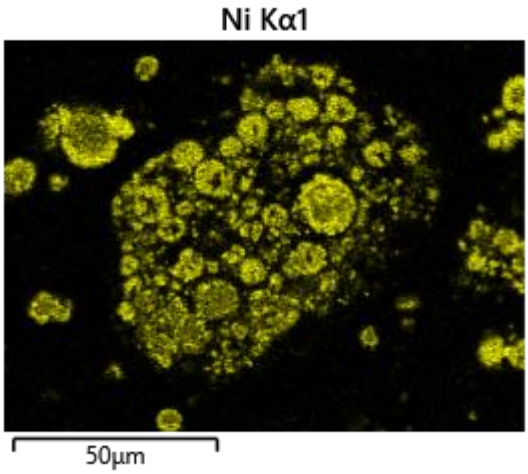

Figure 68. a: EDX mapping for nickel.

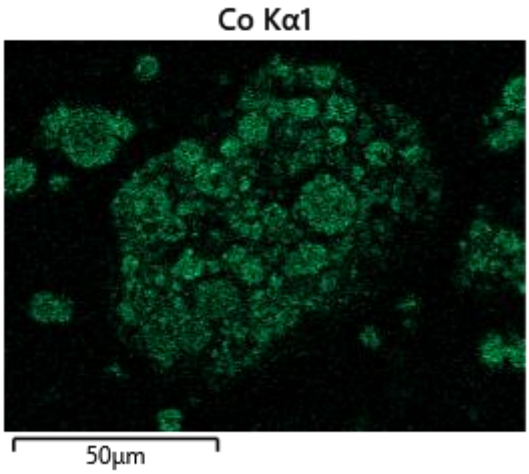

Figure 68. b: EDX mapping for cobalt.

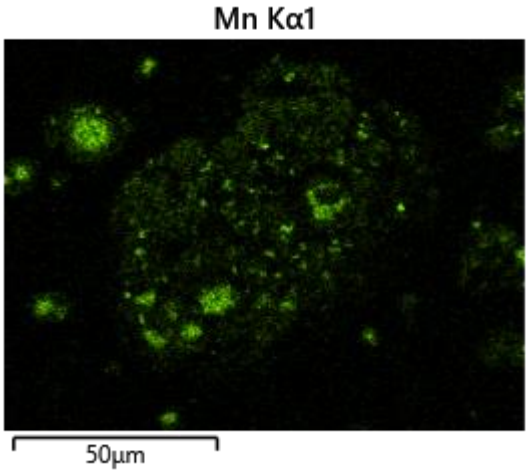

Figure 68. c: EDX mapping for manganese.

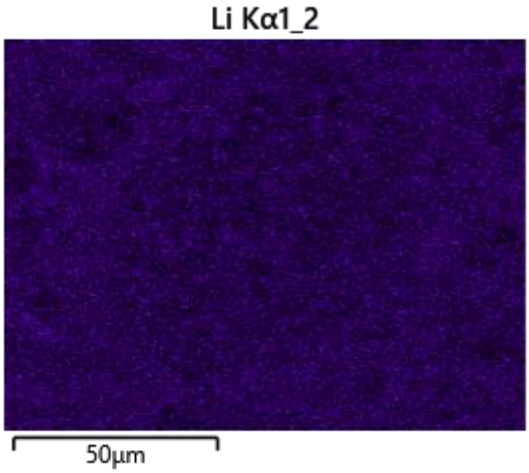

Figure 68. d:EDX mapping for lithium.

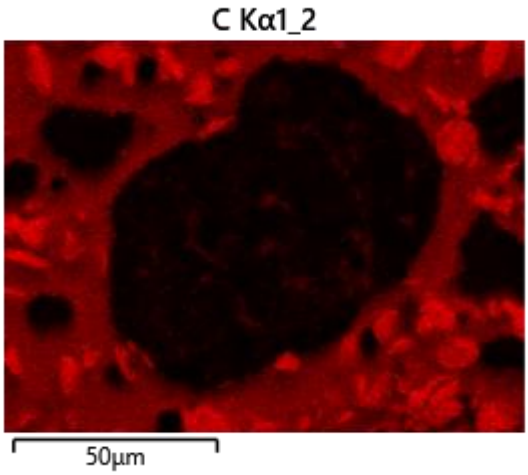

Figure 68. e: EDX mapping for carbon.

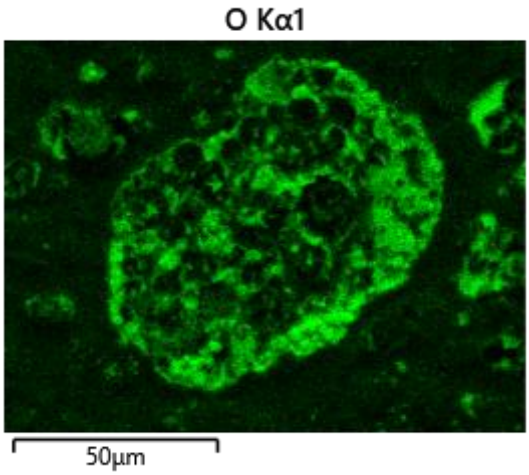

Figure 68. f: EDX mapping for oxygen.

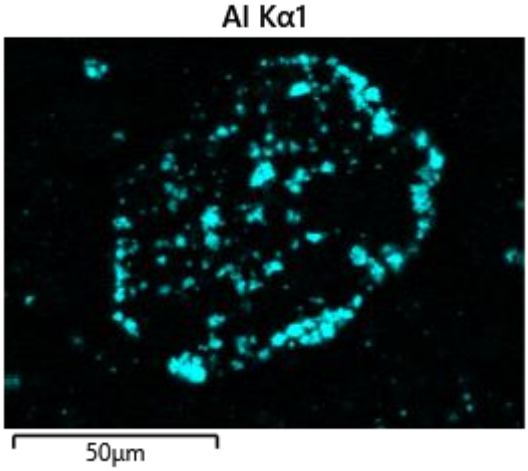

Figure 68. g: EDX mapping for aluminium.

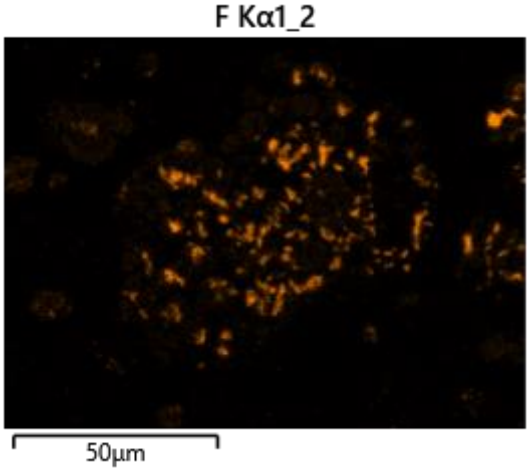

Figure 68. h: EDX mapping for fluorine.

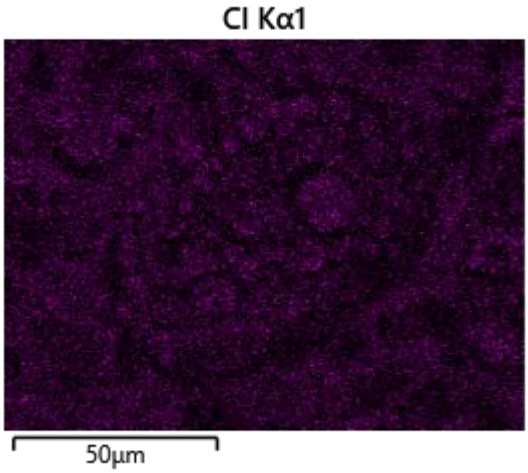

Figure 68. i: EDX mapping for chlorine.

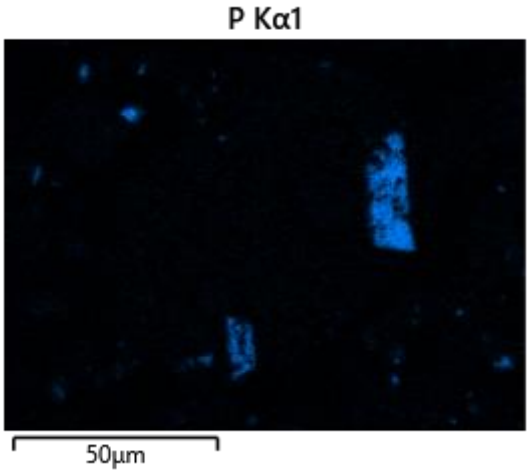

Figure 68. j: EDX mapping for phosphorus.

Records of phosphorus, fluorine, chlorine, and aluminium can be found in the mapping diagram as well. Expectedly, Ni, Co, and Mn were perceptible from this analysis.

4.3.2.5 Microwave Treatment at 1200 ℃

Finally, at 1200 ℃ more elements in their metallic form were found as shown by the XRD graph (Figure 70). Cobalt, manganese, and nickel all their phases were visible. A peak at 30.96º (2-theta value) shows the intensity of the graphite phase. Hence, even after roasting at 1200 ℃ in a microwave, some graphite from the sample remained. Also, bigger conglomeration can be seen within the residue (Figure 69) compared to other experiments.

Figure 69: Sample's image after microwave treatment at 1200 ℃.

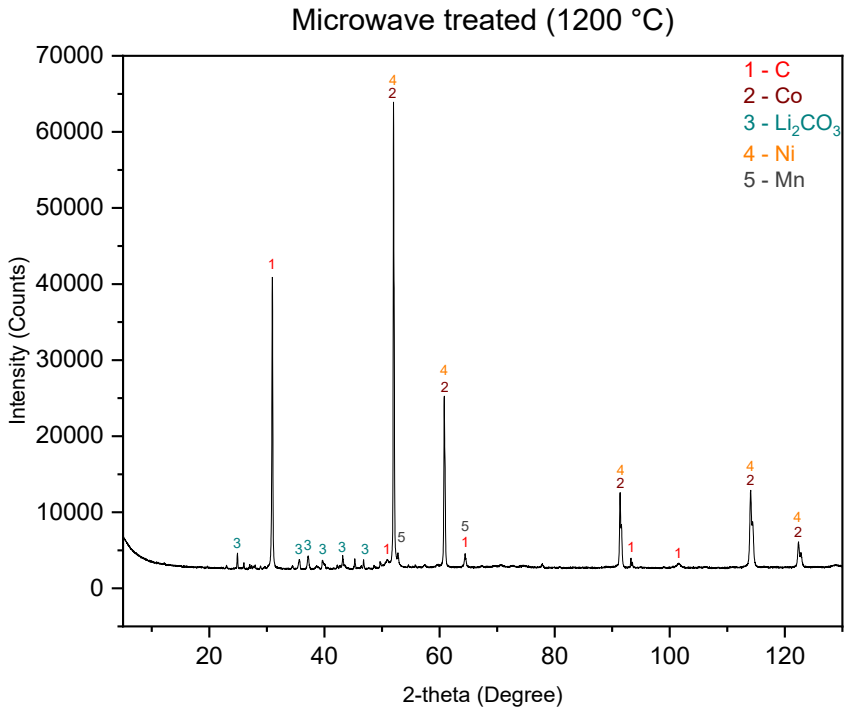

Figure 70: XRD graph of the sample after microwave treatment at 1200 ℃.

The structure of the sample viewed from an SEM image (Figure 71) is almost like the previous one. However, there are fewer dark spots within the bright region. Probably that could be an indication of the formation of more metallic materials. A large peak of nickel was visible from the EDX (Figure 72) spectrum. The elements that we previously encountered are also present within the treated sample.

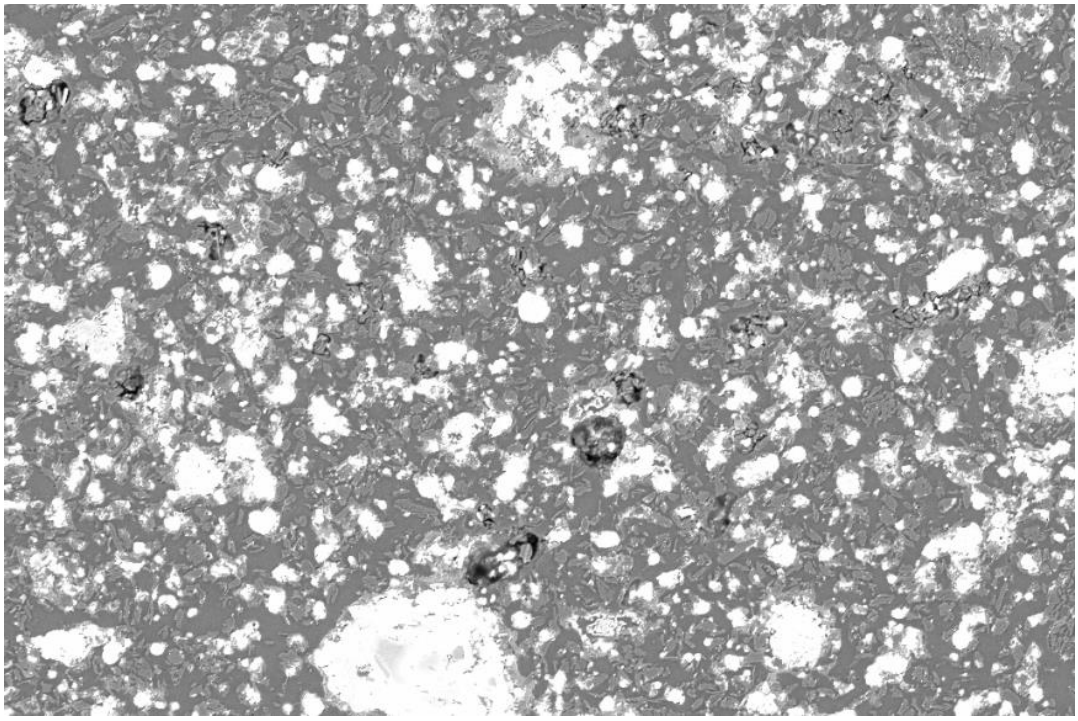

Figure 71: SEM image of the sample after microwave treatment at 1200 ℃.

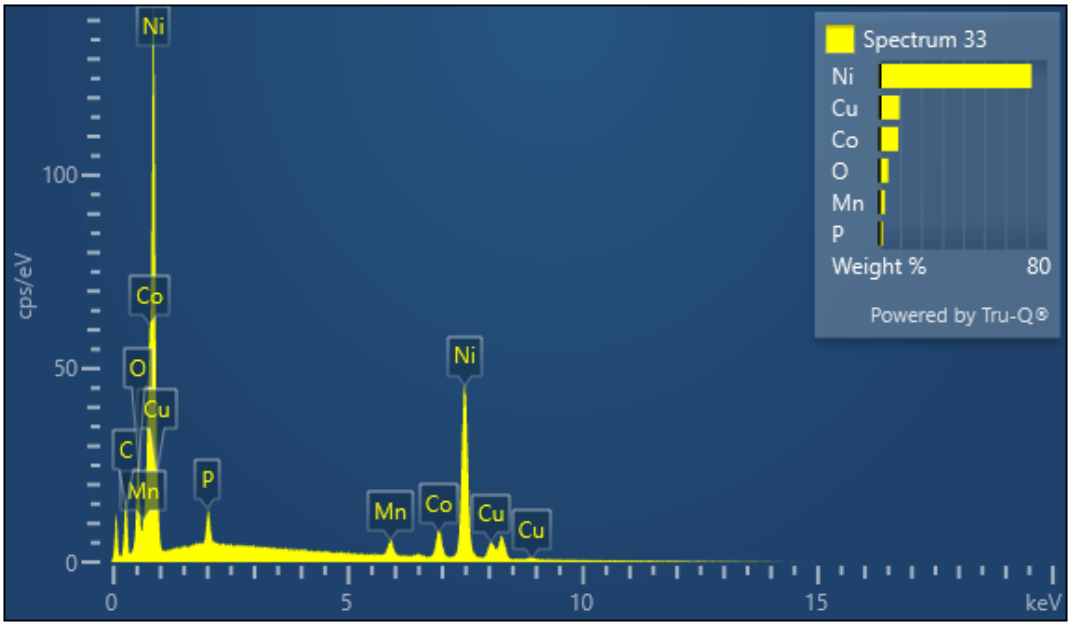

Figure 72: EDX spectra of the sample after microwave treatment at 1200 ℃.

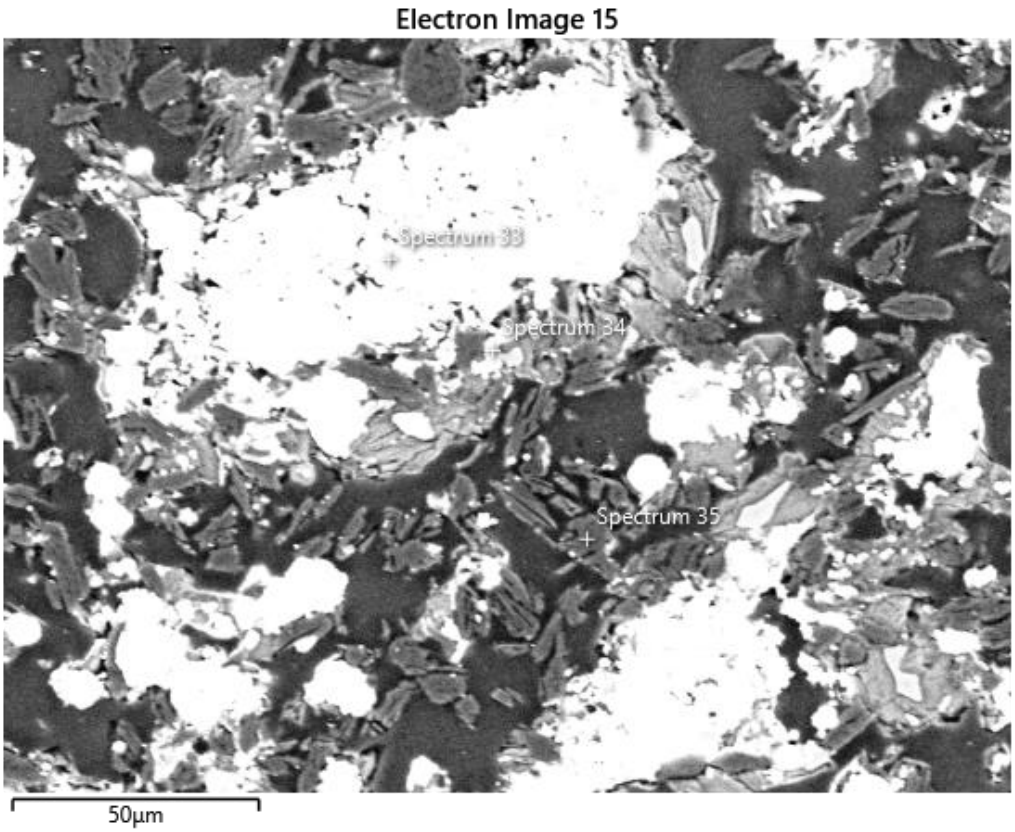

Figure 73: SEM image of the sample after microwave treatment at 1200 ℃ at 50 µm magnification.

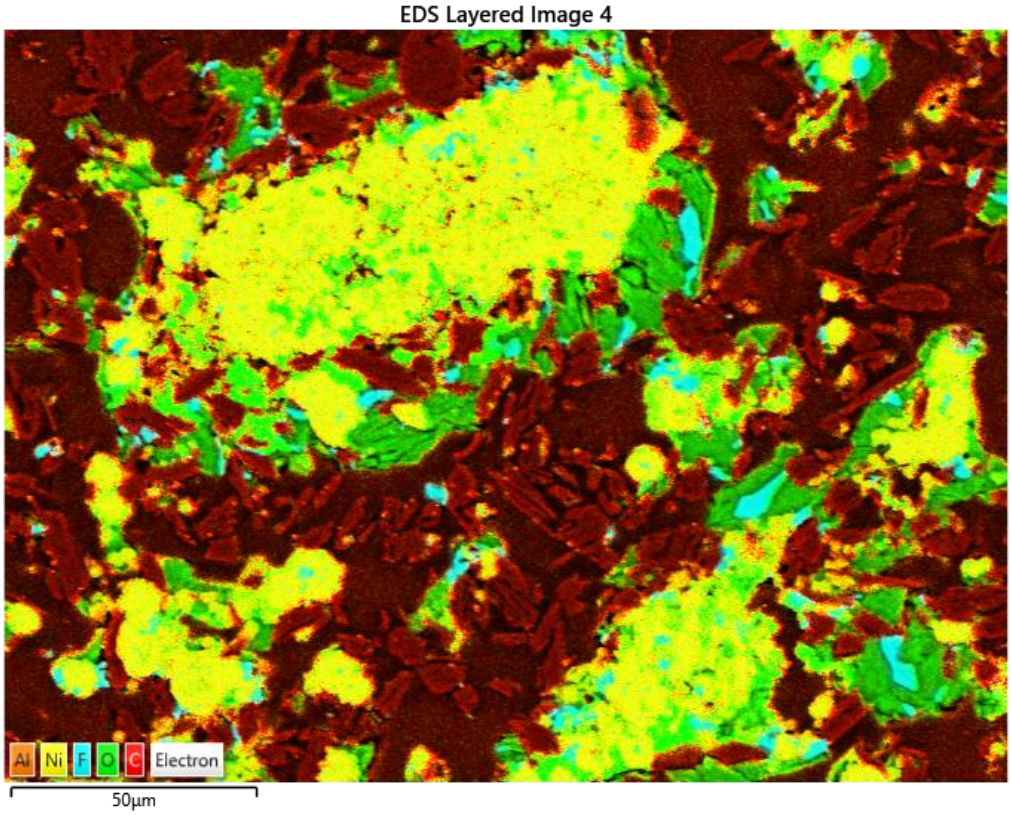

Figure 74: EDX layered image of the sample after microwave treatment at 1200 ℃.

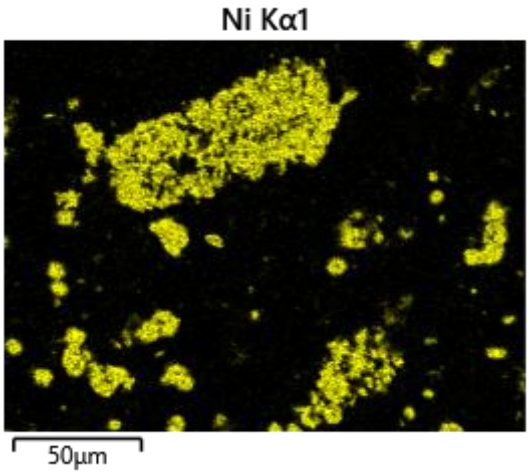

Figure 74. a: EDX mapping for nickel.

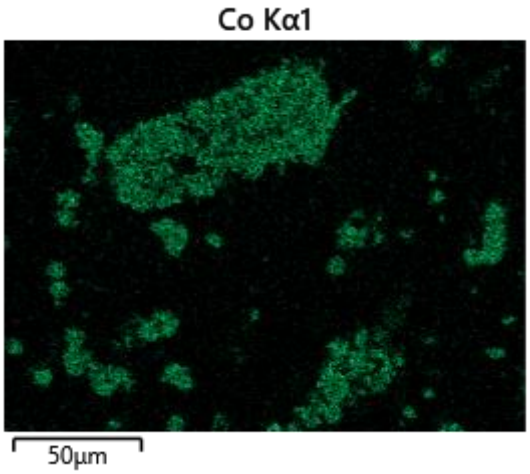

Figure 74. b: EDX mapping for cobalt.

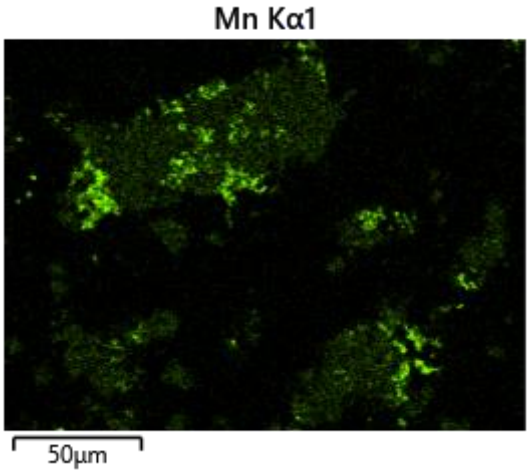

Figure 74. c: EDX mapping for manganese.

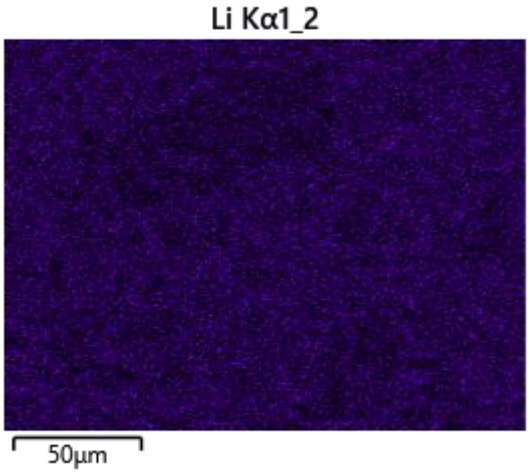

Figure 74. d: EDX mapping for lithium.

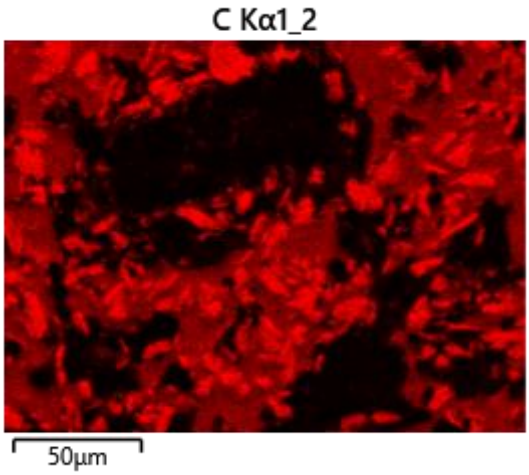

Figure 74. e: EDX mapping for carbon.

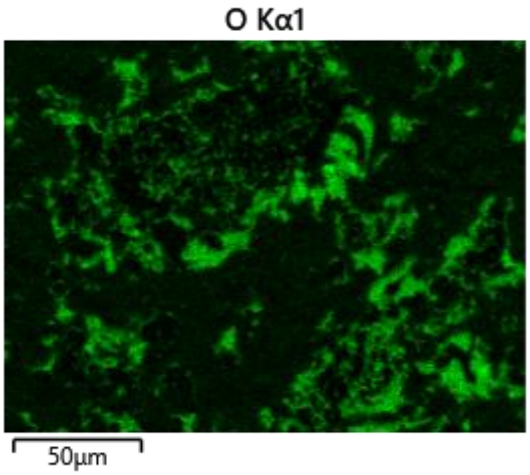

Figure 74. f: EDX mapping for oxygen.

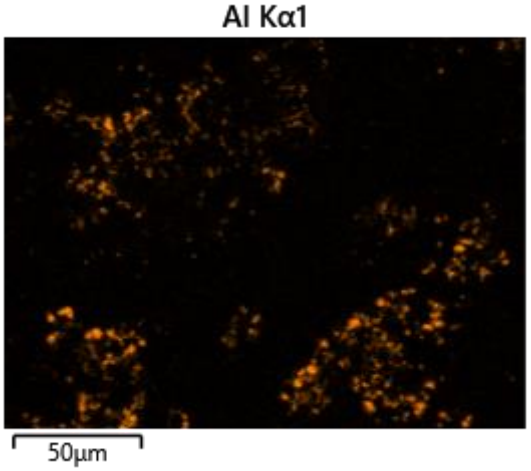

Figure 74. g: EDX mapping for aluminium.

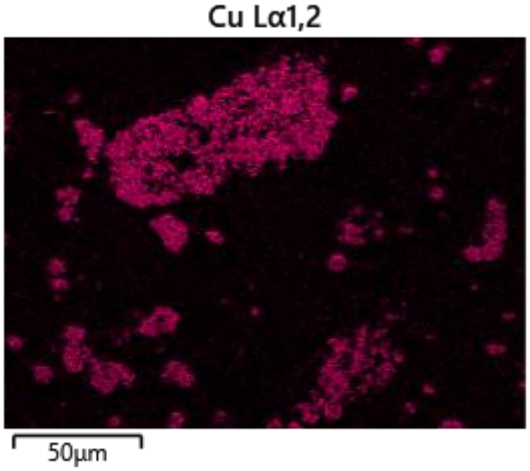

Figure 74. h: EDX mapping for copper.

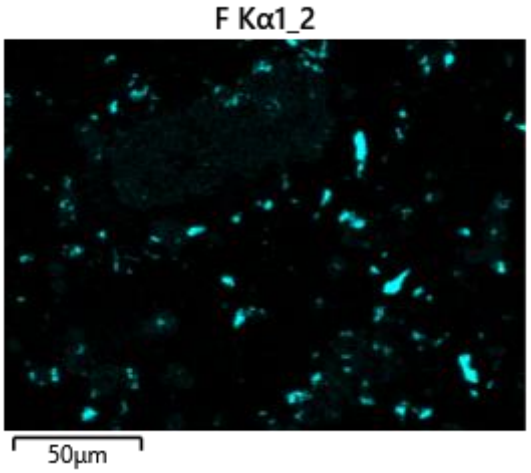

Figure 74. i: EDX mapping for fluorine.

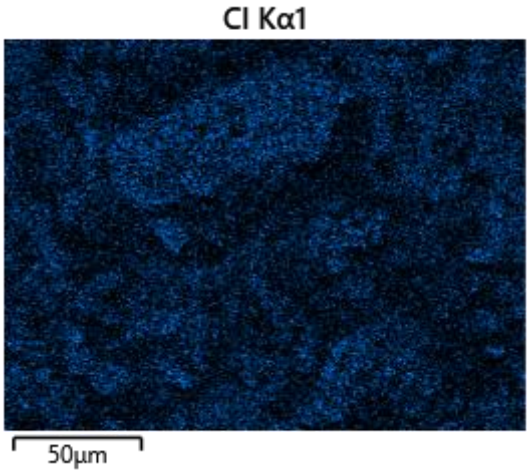

Figure 74. j: EDX mapping for chlorine.

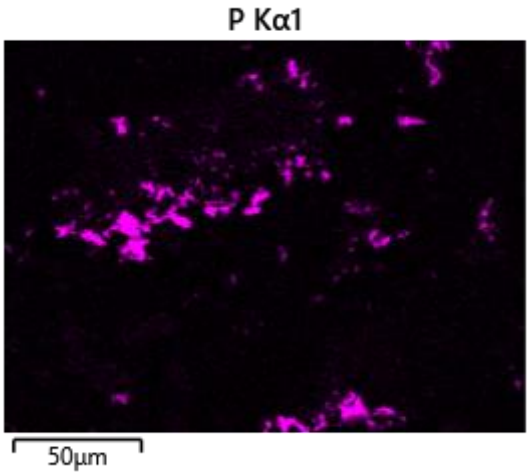

Figure 74. k: EDX mapping for phosphorus.

The orientations of graphite and metals were almost alike compared to the previous experiment. Traces of aluminium and copper can be found along with other impurities that remained in the raw material after pre-treatment. Since, cobalt, nickel, and lithium can be transformed into their metallic form, roasting under microwave radiation at 1200 ℃ could make their recovery by hydrometallurgical process easier.

A closely related work has been done by Pinder et al. where they managed to find good microwave absorption properties within electrode materials. First, they collected spent batteries from a registered recycler followed by discharging. Then, they removed the steel sheets manually and crushed the electrode sheets in a centrifugal mill. Then, sieving was done to separate Cu and Al (above 53 micron) from electrode materials (below 53 micron). They also reduced the amount of graphite present in the mixture of electrode material by froth floatation. Finally, after processing, they concluded that the microwave treatment increased the dissolution of the metallic values, which matches our conclusion. A significant difference their work and our can be noticed as they compared two kinds of samples, namely ‘as such’ and ‘separated’. In case of first one the treated the mixture of anode and cathode active materials without separating and for the later one, the separated them before processing with microwave. After leaching with sulfuric acid, they recovered 93% Li, 75% Co, 98% Mn, and 79% Ni from separated samples which seemed to be the better approach. Their results showed the optimum conditions for magnetic element formation was 850 ℃ temperature while roasting under microwave for 10 minutes with 30% graphite. They used SEM and XRD for characterization along with thermogravimetric analysis. Economic analysis of that project revealed a net positive cash flow as well [113].

4.3.3 Phase Comparison

The peak at 21.78º is not visible after thermal processing (Figure 75). Hence, we can estimate that the breakdown of the complex cathodic structure is possible with roasting under microwave radiation, even in low temperatures like 400 ℃ while higher temperatures would have been required in the case of conventional heating. After that, the graphite phase at 32.92º remains visible except for TG residue in the air atmosphere. Then, another smaller peak of Lithium-Cobalt-Manganese-Nickel-Oxide vanished. However, around that region, one peak in each sample (TG residue in air atmosphere and microwave treatment at 400 ℃) was present and showed some oxide phases. The next peak at 52.1º and all the larger peaks after that indicate the occupancy of metals such as nickel, cobalt, manganese, and lithium.

Fahimi et al. conducted similar kind of experiments with microwave on spent lithium-ion batteries to extract valuable metals. In their work, heat treatment was done at maximum 900 ℃ on black mass sample collected from recycling facilities. The facility process spent lithium-ion batteries with a series of preprocessing methods. First, a dry mechanical process was employed. Then sorting stage is introduced where the raw materials are sorted according to the chemical composition and metal content using semiautomatic sorting system. Then a mechanically automated machine crushes them. After that, another separation process is done either mechanically or magnetically followed by sieving. Chemical analysis revealed that the mixture contained two types of lithium-ion batteries, NMC-442 and NMC-532. We can observe similarities in the XRD pattern of their work (Figure 76) with our work. The intensity of the peaks indicating cathodic materials and graphite from the black mass reduced with the increasing of the temperature, while the intensities of the metallic oxides, such as Mn_3O_4, CoO, and NiO *etc*. were increased gradually. Unlike our results, phases of metals, for instance Co, Ni, and Mn are missing from the XRD pattern, another interesting assumption can be drawn here, which is the formation of pure metallic elements requires even higher temperatures. Their XRD pattern also shows the presence of graphite even after treatment at 900 ℃ [114]. This same phenomenon has been observed in our results.

Overall, there have been several changes occurred within black mass sample after each stage of microwave processing. Agglomeration of materials formed after each experiment and the amount of aggregate increased with higher temperature. SEM and EDX results also transformed where we could see the flakes like shape of graphite decreased and the area covering metallic elements increased. Traces of impurities that were present within the raw black mass such as Cu, Al, P, and F also remained in the treated sample. Since, the preprocessing of these black mass was done by different facilities, it was very difficult to find possible sources of those materials. However, some of them can come from the battery itself, for instance Al, Cu, and F since they are essential elements of LIBs.

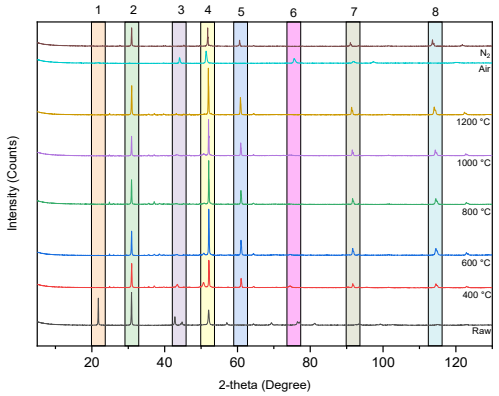

Figure 75: XRD curve comparison from all the samples.

XRD results: Different phases are marked with numbers (1: cathode, 2: graphite, 3: oxides, 4: metals (Co, Ni, and Mn), 5: metals (Co, and Ni), 6: oxides, 7: metals (Co, and Ni), 8: metals (Co, and Ni).

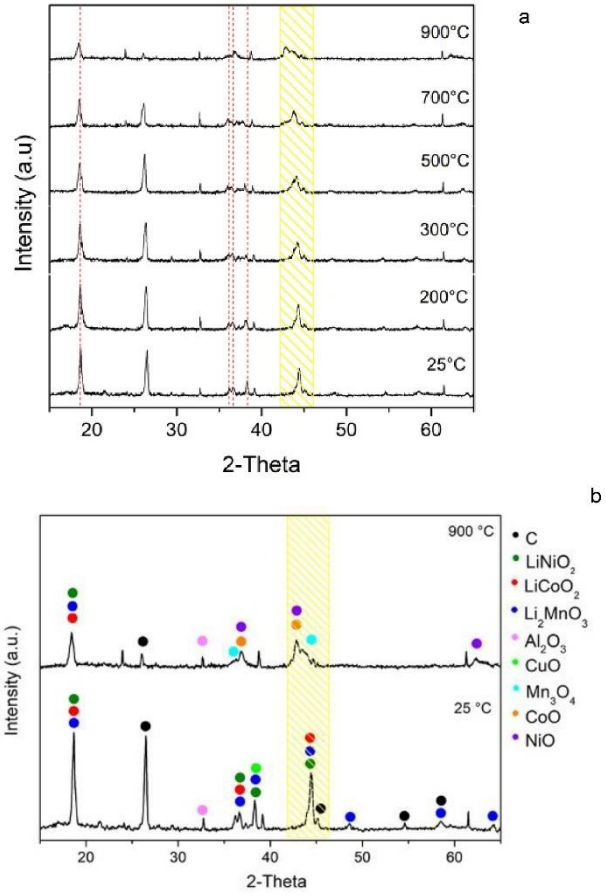

Figure 76: XRD pattern at different temperature on black mass. a) the evaluation of XRD pattern from 25 ℃ to 900 ℃, b) detailed phases attribution of XRD pattern collected at 25 ℃ and 900 ℃. Reused under CC BY-NC-ND 4.0 from ref [114].

5 Summary & Conclusion

The effect of microwave radiation on the decomposition of electrode materials was tested to find an environmentally friendly, cost-effective, and energy-efficient spent lithium-ion battery recycling technique. Since higher heating can be achieved within a short period while using less energy via the microwave route, the whole metal recovery process would become cheaper when using the microwave as a heating source compared to conventional heating.

Thermogravimetric analysis (TGA), and differential scanning calorimetry (DSC) coupled with mass spectrometry revealed the thermal behaviour of black mass and possible reactions between the cathode and graphite anode materials recovered from the spent lithium-ion batteries. TGA curve showed the mass loss of the mixture in two different atmospheres, where the remaining mass in the inert atmosphere was greater than in the air atmosphere. Combining the DSC and MS curves with the TGA curve gave us the possible reactions that happened in the chamber. Finally, the SEM and XRD analysis from the remainder of the sample showed us the materials left within the residue. In the air atmosphere, almost no graphite was found, and mostly metallic oxides were formed. On the other hand, inert atmospheric conditions were better for the transformation into metals. Both can be easily recoverable. in the case of oxides, leaching would be required, and metals can be magnetically separated.

Microwave radiation can easily break down complex cathodic structures into single metallic elements like oxides or carbonates in the presence of graphite. Roasting at low temperatures like 400 °C was enough for the formation of cobalt oxide, nickel oxide, and manganese oxides etc. However, increasing the temperature was beneficial as it promoted the formation of lower valance oxides and metals of nickel, cobalt, and manganese. After roasting for 10 minutes at 1200 °C, we could see more metallic peaks from the XRD results. After this process, materials could be recovered with the application of a hydrometallurgical process. However, the amount of required solvent would be smaller, and the cost of materials could be saved, making the process cost-effective. We also evaluated the temperature profile of the black mass sample under microwave radiation. The power setting of the microwave device was at 4 kW, and it took just over 5 minutes to reach the temperature of 1200 °C. Hence, the process becomes energy efficient. Since microwave is operated by electrical energy, renewable sources can be equipped with the device, which would make it environmentally friendly.

5.1 Limitations and Future Research

Quantifying the number of recovered products was out of the scope of this work. Getting a value would give a more precise conclusion. Securing the black mass from the crucible after the treatment was difficult, especially after high-temperature treatment. Even though the alumina crucible can withstand very high temperatures, such as 2000 ℃, our crucible broke after the 1200 ℃ treatment stage. Also, taking out those materials from the crucible needs to be done carefully, otherwise, it can get contaminated. Avoiding agglomeration during the microwave process would increase the leaching efficiency. Hence, that should be taken into consideration. Furthermore, the lesser the energy consumption during the processing the better.

The characterisation tools that we used have some limitations as well. Light materials, such as lithium cannot be detected using SEM-EDX. Additionally, identifying amorphous materials is not possible by XRD. However, our sample does not contain many light materials other than lithium and showed good crystallinity.

Different thermal treatment times with varying material compositions could be tested. Hence, there are more opportunities to work with this method. Some other characterisation techniques could also be used. LECO test could provide us with the amount of graphite that remains within the sample after each process. Also, an elemental analysis could have been conducted using the ICP-OES technique.

Finally, our results were compared with two of the previous works [113,114]. The comparison shows significant similarities. Hence, even though we had some limitations we can be satisfied with our results.

References

[1] J. Brady, M. O'Mahony, Travel to work in Dublin. The potential impacts of electric vehicles on climate change and urban air quality, Transp Res D Transp Environ 16 (2011) 188–193. https://doi.org/10.1016/J.TRD.2010.09.006.

[2] IEA, Trends in electric light-duty vehicles – Global EV Outlook 2023 – Analysis, Paris, 2023. https://www.iea.org/reports/global-ev-outlook-2023/trends-in-electric-light-duty-vehicles (accessed October 20, 2023).

[3] S. Statharas, Y. Moysoglou, P. Siskos, G. Zazias, P. Capros, Factors Influencing Electric Vehicle Penetration in the EU by 2030: A Model-Based Policy Assessment, Energies 2019, Vol. 12, Page 2739 12 (2019) 2739. https://doi.org/10.3390/EN12142739.

[4] Eurostat, Renewable energy on the rise: 37% of EU's electricity, Products Eurostat News (2022). https://ec.europa.eu/eurostat/web/products-eurostat-news/-/ddn-20220126-1 (accessed October 23, 2023).

[5] S. Ould Amrouche, D. Rekioua, T. Rekioua, S. Bacha, Overview of energy storage in renewable energy systems, Int J Hydrogen Energy 41 (2016) 20914–20927. https://doi.org/10.1016/J.IJHYDENE.2016.06.243.

[6] H.A. Behabtu, M. Messagie, T. Coosemans, M. Berecibar, K.A. Fante, A.A. Kebede, J. Van Mierlo, A Review of Energy Storage Technologies' Application Potentials in Renewable Energy Sources Grid Integration, Sustainability 2020, Vol. 12, Page 10511 12 (2020) 10511. https://doi.org/10.3390/SU122410511.

[7] H. Bae, Y. Kim, Technologies of lithium recycling from waste lithium ion batteries: a review, Mater Adv 2 (2021) 3234–3250. https://doi.org/10.1039/D1MA00216C.

[8] M. Li, J. Lu, Z. Chen, K. Amine, 30 Years of Lithium-Ion Batteries, Advanced Materials 30 (2018) 1800561. https://doi.org/10.1002/ADMA.201800561.

[9] R. Korthauer, Lithium-Ion Batteries: Basics and Applications, 2018. https://books.google.fi/books?hl=fi&lr=&id=ll1oD-wAAQBAJ&oi=fnd&pg=PA4&dq=applications+of+lithium+ion+batteries+in+energy+storage&ots=s2VRyBwRM6&sig=riIJfYML9oe4-VXgWnwxXAaYAao&redir_esc=y#v=onepage&q=applications%20of%20lithium%20ion%20batteries%20in%20energy%20storage&f=false (accessed November 2, 2023).

[10] M. Madian, A. Eychmüller, L. Giebeler, Current Advances in TiO2-Based Nanostructure Electrodes for High Performance Lithium Ion Batteries, Batteries 2018, Vol. 4, Page 7 4 (2018) 7. https://doi.org/10.3390/BATTERIES4010007.

[11] T. Chen, Y. Jin, H. Lv, A. Yang, M. Liu, B. Chen, Y. Xie, Q. Chen, Applications of Lithium-Ion Batteries in Grid-Scale Energy Storage Systems, Transactions of Tianjin University 26 (2020) 208–217. https://doi.org/10.1007/S12209-020-00236-W/FIGURES/4.

[12] C. De Las Casas, W. Li, A review of application of carbon nanotubes for lithium ion battery anode material, J Power Sources 208 (2012) 74–85. https://doi.org/10.1016/J.JPOWSOUR.2012.02.013.

[13] D.J. Pereira, A.M. Aleman, J.W. Weidner, T.R. Garrick, A Mechano-Electrochemical Battery Model that Accounts for Preferential Lithiation Inside Blended Silicon Graphite (Si/C) Anodes, J Electrochem Soc 169 (2022) 020577. https://doi.org/10.1149/1945-7111/AC554F.

[14] B.J. Landi, M.J. Ganter, C.D. Cress, R.A. DiLeo, R.P. Raffaelle, Carbon nanotubes for lithium ion batteries, Energy Environ Sci 2 (2009) 638–654. https://doi.org/10.1039/B904116H.

[15] W. Lv, Z. Wang, H. Cao, Y. Sun, Y. Zhang, Z. Sun, A Critical Review and Analysis on the Recycling of Spent Lithium-Ion Batteries, ACS Sustain Chem Eng 6 (2018) 1504–1521. https://doi.org/10.1021/ACSSUSCHEMENG.7B03811/ASSET/IMAGES/LARGE/SC-2017-03811A_0006.JPEG.

[16] J. Xu, S.L. Chou, Q.F. Gu, H.K. Liu, S.X. Dou, The effect of different binders on electrochemical properties of LiNi1/3Mn1/3Co1/3O2 cathode material in lithium ion batteries, J Power Sources 225 (2013) 172–178. https://doi.org/10.1016/J.JPOWSOUR.2012.10.033.

[17] S.S. Zhang, A review on electrolyte additives for lithium-ion batteries, J Power Sources 162 (2006) 1379–1394. https://doi.org/10.1016/J.JPOWSOUR.2006.07.074.

[18] W. Zhao, J. Yi, P. He, H. Zhou, Solid-State Electrolytes for Lithium-Ion Batteries: Fundamentals, Challenges and Perspectives, Electrochemical Energy Reviews 2019 2:4 2 (2019) 574–605. https://doi.org/10.1007/S41918-019-00048-0.

[19] S. Luiso, P. Fedkiw, Lithium-ion battery separators: Recent developments and state of art, Curr Opin Electrochem 20 (2020) 99–107. https://doi.org/10.1016/J.COELEC.2020.05.011.

[20] C.M. Costa, Y.H. Lee, J.H. Kim, S.Y. Lee, S. Lanceros-Méndez, Recent advances on separator membranes for lithium-ion battery applications: From porous membranes to solid electrolytes, Energy Storage Mater 22 (2019) 346–375. https://doi.org/10.1016/J.ENSM.2019.07.024.

[21] A.A. Heidari, H. Mahdavi, Recent Development of Polyolefin-Based Microporous Separators for Li−Ion Batteries: A Review, The Chemical Record 20 (2020) 570–595. https://doi.org/10.1002/TCR.201900054.

[22] C. Lamiel, I. Hussain, X. Ma, K. Zhang, Properties, functions, and challenges: current collectors, Mater Today Chem 26 (2022) 101152. https://doi.org/10.1016/J.MTCHEM.2022.101152.

[23] M. Zackrisson, S. Schellenberger, Toxicity of lithium ion battery chemicals-overview with focus on recycling, (2020). https://urn.kb.se/resolve?urn=urn:nbn:se:ri:diva-66063 (accessed November 13, 2023).

[24] Vinylene carbonate | C3H2O3 | CID 13385 - PubChem, (n.d.). https://pubchem.ncbi.nlm.nih.gov/compound/13385 (accessed November 13, 2023).

[25] Databasen för klassificerings- och märkningsregistret, (n.d.). https://echa.europa.eu/sv/information-on-chemicals/cl-inventory-database/-/discli/details/135702 (accessed November 13, 2023).

[26] T. Schmidt, M. Buchert, L. Schebek, Investigation of the primary production routes of nickel and cobalt products used for Li-ion batteries, Resour Conserv Recycl 112 (2016) 107–122. https://doi.org/10.1016/J.RESCONREC.2016.04.017.

[27] C.J. Ferron, The recycling of cobalt from alloy scrap, spent batteries or catalysts and metallurgical residues - an overview, Ni-Co 2013 (2016) 53–71. https://doi.org/10.1007/978-3-319-48147-0_3/COVER.

[28] M.L.C.M. Henckens, E. Worrell, Reviewing the availability of copper and nickel for future generations. The balance between production growth, sustainability and recycling rates, J Clean Prod 264 (2020) 121460. https://doi.org/10.1016/J.JCLEPRO.2020.121460.

[29] A. Keller, M.W. Hlawitschka, H.J. Bart, Manganese recycling of spent lithium-ion batteries via solvent extraction, Sep Purif Technol 275 (2021) 119166. https://doi.org/10.1016/J.SEPPUR.2021.119166.

[30] O. Velázquez-Martínez, J. Valio, A. Santasalo-Aarnio, M. Reuter, R. Serna-Guerrero, A Critical Review of Lithium-Ion Battery Recycling Processes from a Circular Economy Perspective, Batteries 2019, Vol. 5, Page 68 5 (2019) 68. https://doi.org/10.3390/BATTERIES5040068.

[31] Z.J. Baum, R.E. Bird, X. Yu, J. Ma, Lithium-Ion Battery Recycling─Overview of Techniques and Trends, ACS Energy Lett 7 (2022) 712–719. https://doi.org/10.1021/ACSENERGYLETT.1C02602/ASSET/IMAGES/LARGE/NZ1C02602_0005.JPEG.

[32] Q. Wei, Y. Wu, S. Li, R. Chen, J. Ding, C. Zhang, Spent lithium ion battery (LIB) recycle from electric vehicles: A mini-review, Science of The Total Environment 866 (2023) 161380. https://doi.org/10.1016/J.SCITOTENV.2022.161380.

[33] X. Lai, Y. Huang, H. Gu, C. Deng, X. Han, X. Feng, Y. Zheng, Turning waste into wealth: A systematic review on echelon utilization and material recycling of retired lithium-ion batteries, Energy Storage Mater 40 (2021) 96–123. https://doi.org/10.1016/J.ENSM.2021.05.010.

[34] X. Lai, Y. Huang, C. Deng, H. Gu, X. Han, Y. Zheng, M. Ouyang, Sorting, regrouping, and echelon utilization of the large-scale retired lithium batteries: A critical review, Renewable and Sustainable Energy Reviews 146 (2021) 111162. https://doi.org/10.1016/J.RSER.2021.111162.

[35] C.H. Illa Font, H.V. Siqueira, J.E. Machado Neto, J.L.F. dos Santos, S.L. Stevan, A. Converti, F.C. Corrêa, Second Life of Lithium-Ion Batteries of Electric Vehicles: A Short Review and Perspectives, Energies 2023, Vol. 16, Page 953 16 (2023) 953. https://doi.org/10.3390/EN16020953.

[36] X. Lai, D. Qiao, Y. Zheng, M. Ouyang, X. Han, L. Zhou, A rapid screening and regrouping approach based on neural networks for large-scale retired lithium-ion cells in second-use applications, J Clean Prod 213 (2019) 776–791. https://doi.org/10.1016/J.JCLEPRO.2018.12.210.

[37] L. Chen, C. Xu, X. Bao, A. Lopes, P. Li, C. Zhang, State-of-health estimation of Lithium-ion battery based on back-propagation neural network with adaptive

hidden layer, Neural Comput Appl 35 (2023) 14169–14182. https://doi.org/10.1007/S00521-023-08471-7/TABLES/1.

[38] D. Yu, Z. Huang, B. Makuza, X. Guo, Q. Tian, Pretreatment options for the recycling of spent lithium-ion batteries: A comprehensive review, Miner Eng 173 (2021) 107218. https://doi.org/10.1016/J.MINENG.2021.107218.

[39] A. Holzer, J. Zimmermann, L. Wiszniewski, T. Necke, C. Gatschlhofer, W. Öfner, H. Raupenstrauch, A Combined Hydro-Mechanical and Pyrometallurgical Recycling Approach to Recover Valuable Metals from Lithium-Ion Batteries Avoiding Lithium Slagging, Batteries 2023, Vol. 9, Page 15 9 (2022) 15. https://doi.org/10.3390/BATTERIES9010015.

[40] A. Holzer, M. Baldauf, L. Wiszniewski, S. Windisch-Kern, H. Raupenstrauch, Influence of impurities on the high-temperature behavior of the lithium-ion battery cathode material NMC under reducing conditions for use in the InduRed reactor concept, Detritus 20 (2022) 22–28. https://doi.org/10.31025/2611-4135/2022.15215.

[41] S. Al-Thyabat, T. Nakamura, E. Shibata, A. Iizuka, Adaptation of minerals processing operations for lithium-ion (LiBs) and nickel metal hydride (NiMH) batteries recycling: Critical review, Miner Eng 45 (2013) 4–17. https://doi.org/10.1016/J.MINENG.2012.12.005.

[42] X. Zhou, W.Z. He, G.M. Li, X.J. Zhang, J.W. Huang, S.G. Zhu, Recycling of electrode materials from spent lithium-ion batteries, 2010 4th International Conference on Bioinformatics and Biomedical Engineering, ICBBE 2010 (2010). https://doi.org/10.1109/ICBBE.2010.5518015.

[43] G. Khodadadmahmoudi, K. Javdan Tabar, A.H. Homayouni, S. Chehreh Chelgani, Recycling spent lithium batteries – an overview of pretreatment flowsheet development based on metallurgical factors, Environmental Technology Reviews 12 (2023). https://doi.org/10.1080/21622515.2023.2248559.

[44] G. Zhang, Y. He, H. Wang, Y. Feng, W. Xie, X. Zhu, Removal of Organics by Pyrolysis for Enhancing Liberation and Flotation Behavior of Electrode Materials Derived from Spent Lithium-Ion Batteries, ACS Sustain Chem Eng 8 (2020) 2205–2214. https://doi.org/10.1021/ACSSUSCHEMENG.9B05896/ASSET/IMAGES/LARGE/SC9B05896_0002.JPEG.

[45] S. Yu, J. Xiong, D. Wu, X. Lü, Z. Yao, S. Xu, J. Tang, Pyrolysis characteristics of cathode from spent lithium-ion batteries using advanced TG-FTIR-GC/MS analysis, Environmental Science and Pollution Research 27 (2020) 40205–40209. https://doi.org/10.1007/S11356-020-10108-4/FIGURES/5.

[46] R. Mende, D. Kaiser, S. Pavón, M. Bertau, The COOL process – a holistic approach towards Lithium recycling, (2022). https://doi.org/10.21203/RS.3.RS-1965148/V1.

[47] E. Mousa, X. Hu, L. Ånnhagen, G. Ye, A. Cornelio, A. Fahimi, E. Bontempi, P. Frontera, C. Badenhorst, A.C. Santos, K. Moreira, A. Guedes, B. Valentim, Characterization and Thermal Treatment of the Black Mass from Spent Lithium-Ion Batteries, Sustainability (Switzerland) 15 (2023) 15. https://doi.org/10.3390/SU15010015/S1.

[48] S. Babanejad, H. Ahmed, C. Andersson, C. Samuelsson, A. Lennartsson, B. Hall, L. Arnerlöf, High-Temperature Behavior of Spent Li-Ion Battery Black Mass in Inert Atmosphere, Journal of Sustainable Metallurgy 8 (2022) 566–581. https://doi.org/10.1007/S40831-022-00514-Y/TABLES/3.

[49] T. Georgi-Maschler, B. Friedrich, R. Weyhe, H. Heegn, M. Rutz, Development of a recycling process for Li-ion batteries, J Power Sources 207 (2012) 173–182. https://doi.org/10.1016/J.JPOWSOUR.2012.01.152.

[50] F. Habashi, Metallurgy, Kirk-Othmer Encyclopedia of Chemical Technology (2019) 1–14. https://doi.org/10.1002/0471238961.1921182208091911.A01.PUB2.

[51] A. Holzer, J. Zimmermann, L. Wiszniewski, T. Necke, C. Gatschlhofer, W. Öfner, H. Raupenstrauch, A Combined Hydro-Mechanical and Pyrometallurgical Recycling Approach to Recover Valuable Metals from Lithium-Ion Batteries Avoiding Lithium Slagging, Batteries 2023, Vol. 9, Page 15 9 (2022) 15. https://doi.org/10.3390/BATTERIES9010015.

[52] P. Liu, L. Xiao, Y. Tang, Y. Chen, L. Ye, Y. Zhu, Study on the reduction roasting of spent LiNi x Co y Mn z O 2 lithium-ion battery cathode materials, J Therm Anal Calorim 136 (2019) 1323–1332. https://doi.org/10.1007/S10973-018-7732-7/FIGURES/13.

[53] J. Li, G. Wang, Z. Xu, Environmentally-friendly oxygen-free roasting/wet magnetic separation technology for in situ recycling cobalt, lithium carbonate and

graphite from spent LiCoO2/graphite lithium batteries, J Hazard Mater 302 (2016) 97–104. https://doi.org/10.1016/J.JHAZMAT.2015.09.050.

[54] K. Yan, Q. Chen, Z. Xiong, J. Wu, Z. Zhang, Z. Xu, R. Wang, J. Li, S. Zhong, A Novel Method for the Recovery of Li from Spent Lithium-Ion Batteries Using Reduction Roasting–Countercurrent Leaching, JOM 74 (2022) 3821–3832. https://doi.org/10.1007/S11837-022-05432-8/FIGURES/8.

[55] X. Hu, E. Mousa, Y. Tian, G. Ye, Recovery of Co, Ni, Mn, and Li from Li-ion batteries by smelting reduction - Part I: A laboratory-scale study, J Power Sources 483 (2021) 228936. https://doi.org/10.1016/J.JPOWSOUR.2020.228936.

[56] X. Hu, E. Mousa, G. Ye, Recovery of Co, Ni, Mn, and Li from Li-ion batteries by smelting reduction - Part II: A pilot-scale demonstration, J Power Sources 483 (2021) 229089. https://doi.org/10.1016/J.JPOWSOUR.2020.229089.

[57] Y. Huang, P. Shao, L. Yang, Y. Zheng, Z. Sun, L. Fang, W. Lv, Z. Yao, L. Wang, X. Luo, Thermochemically driven crystal phase transfer via chlorination roasting toward the selective extraction of lithium from spent LiNi1/3Co1/3Mn1/3O2, Resour Conserv Recycl 174 (2021) 105757. https://doi.org/10.1016/J.RESCONREC.2021.105757.

[58] Z. Yao, P. Shao, D. Fang, J. Shao, D. Li, L. Liu, Y. Huang, Z. Yu, L. Yang, K. Yu, X. Luo, Thiol-rich, porous carbon for the efficient capture of silver: Understanding the relationship between the surface groups and transformation pathways of silver, Chemical Engineering Journal 427 (2022) 131470. https://doi.org/10.1016/J.CEJ.2021.131470.

[59] Y. Zheng, P. Shao, L. Yang, Y. Huang, H. Zhang, L. Fang, C. Qiu, H. Tang, J. Shao, X. Luo, Gas exchange-driven carbothermal reduction for simultaneous lithium extraction from anode and cathode scraps, Resour Conserv Recycl 188 (2023) 106696. https://doi.org/10.1016/J.RESCONREC.2022.106696.

[60] M. Derhy, Y. Taha, R. Hakkou, M. Benzaazoua, Review of the Main Factors Affecting the Flotation of Phosphate Ores, Minerals 2020, Vol. 10, Page 1109 10 (2020) 1109. https://doi.org/10.3390/MIN10121109.

[61] B.A. Nuraeni, K. Avarmaa, L.H. Prentice, W.J. Rankin, M.A. Rhamdhani, Carbothermic reduction of LiCoO2 cathode material: Thermodynamic analysis, microstructure and mechanisms, Sustainable Materials and Technologies 34 (2022) e00526. https://doi.org/10.1016/J.SUSMAT.2022.E00526.

[62] S. Pindar, N. Dhawan, Kinetic Evaluation of In-Situ Carbothermic Processing of Mixed Electrode Material of Discarded Li-Ion Batteries, Metallurgical and Materials Transactions B: Process Metallurgy and Materials Processing Science 52 (2021) 3078–3092. https://doi.org/10.1007/S11663-021-02235-1/FIGURES/10.

[63] S. Pindar, N. Dhawan, Carbothermal Reduction of Spent Mobile Phones Batteries for the Recovery of Lithium, Cobalt, and Manganese Values, JOM 71 (2019) 4483–4491. https://doi.org/10.1007/S11837-019-03799-9/FIGURES/8.

[64] Z. Liang, C. Cai, G. Peng, J. Hu, H. Hou, B. Liu, S. Liang, K. Xiao, S. Yuan, J. Yang, Hydrometallurgical Recovery of Spent Lithium Ion Batteries: Environmental Strategies and Sustainability Evaluation, ACS Sustain Chem Eng 9 (2021) 5750–5767. https://doi.org/10.1021/ACSSUSCHEMENG.1C00942/ASSET/IMAGES/LARGE/SC1C00942_0010.JPEG.

[65] Z. Sun, H. Cao, Y. Xiao, J. Sietsma, W. Jin, H. Agterhuis, Y. Yang, Toward Sustainability for Recovery of Critical Metals from Electronic Waste: The Hydrochemistry Processes, ACS Sustain Chem Eng 5 (2017) 21–40. https://doi.org/10.1021/ACSSUSCHEMENG.6B00841/ASSET/IMAGES/LARGE/SC-2016-00841T_0023.JPEG.

[66] F. Su, X. Zhou, X. Liu, J. Yang, J. Tang, W. Yang, Z. Li, H. Wang, Y. Ma, Efficient recovery of valuable metals from spent Lithium-ion batteries by pyrite method with hydrometallurgy process, Chemical Engineering Journal 455 (2023) 140914. https://doi.org/10.1016/J.CEJ.2022.140914.

[67] N. Vieceli, R. Casasola, G. Lombardo, B. Ebin, M. Petranikova, Hydrometallurgical recycling of EV lithium-ion batteries: Effects of incineration on the leaching efficiency of metals using sulfuric acid, Waste Management 125 (2021) 192–203. https://doi.org/10.1016/J.WASMAN.2021.02.039.

[68] X. Chen, Y. Chen, T. Zhou, D. Liu, H. Hu, S. Fan, Hydrometallurgical recovery of metal values from sulfuric acid leaching liquor of spent lithium-ion batteries, Waste Management 38 (2015) 349–356. https://doi.org/10.1016/J.WASMAN.2014.12.023.

[69] B. Huang, Z. Pan, X. Su, L. An, Recycling of lithium-ion batteries: Recent advances and perspectives, J Power Sources 399 (2018) 274–286. https://doi.org/10.1016/J.JPOWSOUR.2018.07.116.

[70] F. Su, X. Zhou, X. Liu, J. Yang, J. Tang, W. Yang, Z. Li, H. Wang, Y. Zhang, Y. Ma, Recovery of valuable metals from spent lithium-ion batteries by complexation-assisted ammonia leaching from reductive roasting residue, Chemosphere 312 (2023) 137230. https://doi.org/10.1016/J.CHEMOSPHERE.2022.137230.

[71] S. Ilyas, R.R. Srivastava, H. Kim, N. Ilyas, R. Sattar, Extraction of nickel and cobalt from a laterite ore using the carbothermic reduction roasting-ammoniacal leaching process, Sep Purif Technol 232 (2020) 115971. https://doi.org/10.1016/J.SEPPUR.2019.115971.

[72] R. Mende, D. Kaiser, S. Pavón, M. Bertau, The COOL Process: A Holistic Approach Towards Lithium Recycling, Waste Biomass Valorization 14 (2023) 3027–3042. https://doi.org/10.1007/S12649-023-02043-5/FIGURES/16.

[73] N.B. Horeh, S.M. Mousavi, S.A. Shojaosadati, Bioleaching of valuable metals from spent lithium-ion mobile phone batteries using Aspergillus niger, J Power Sources 320 (2016) 257–266. https://doi.org/10.1016/J.JPOWSOUR.2016.04.104.

[74] J. Liu, T.Y. Mak, Z. Meng, X. Wang, Y. Cao, Z. Lu, D.W.S. Suen, X.Y. Lu, Y. Tang, Efficient recovery of lithium as Li2CO3 and cobalt as Co3O4 from spent lithium-ion batteries after leaching with p-toluene sulfonic acid, Hydrometallurgy 216 (2023) 106012. https://doi.org/10.1016/J.HYDROMET.2022.106012.

[75] R. Golmohammadzadeh, F. Faraji, F. Rashchi, Recovery of lithium and cobalt from spent lithium ion batteries (LIBs) using organic acids as leaching reagents: A review, Resour Conserv Recycl 136 (2018) 418–435. https://doi.org/10.1016/J.RESCONREC.2018.04.024.

[76] Y. Chen, P. Shi, D. Chang, Y. Jie, S. Yang, G. Wu, H. Chen, J. Zhu, F. Hu, B.P. Wilson, M. Lundstrom, Selective extraction of valuable metals from spent EV power batteries using sulfation roasting and two stage leaching process, Sep Purif Technol 258 (2021) 118078. https://doi.org/10.1016/J.SEPPUR.2020.118078.

[77] F. Meng, Q. Liu, R. Kim, J. Wang, G. Liu, A. Ghahreman, Selective recovery of valuable metals from industrial waste lithium-ion batteries using citric acid under reductive conditions: Leaching optimization and kinetic analysis, Hydrometallurgy 191 (2020) 105160. https://doi.org/10.1016/J.HYDROMET.2019.105160.

[78] L. Xing, J. Bao, S. Zhou, Y. Qiu, H. Sun, S. Gu, J. Yu, Ultra-fast leaching of critical metals from spent lithium-ion batteries cathode materials achieved by the synergy-coordination mechanism, Chemical Engineering Journal 420 (2021) 129593. https://doi.org/10.1016/J.CEJ.2021.129593.

[79] S. Gu, J. Kong, L. Xing, H. Sun, Y. Qiu, J. Yu, Insights into the coordination enhanced leaching mechanism of spent lithium-ion batteries cathode materials, J Environ Chem Eng 10 (2022) 107745. https://doi.org/10.1016/J.JECE.2022.107745.

[80] J. Lie, S. Tanda, J.-C. Liu, J. Vladi´cvladi´c, S.J. Joki´c, Subcritical Water Extraction of Valuable Metals from Spent Lithium-Ion Batteries, Molecules 2020, Vol. 25, Page 2166 25 (2020) 2166. https://doi.org/10.3390/MOLECULES25092166.

[81] J. Lie, J.C. Liu, Closed-vessel microwave leaching of valuable metals from spent lithium-ion batteries (LIBs) using dual-function leaching agent: Ascorbic acid, Sep Purif Technol 266 (2021) 118458. https://doi.org/10.1016/J.SEPPUR.2021.118458.

[82] Á. Martín, A. Navarrete, Microwave-assisted process intensification techniques, Curr Opin Green Sustain Chem 11 (2018) 70–75. https://doi.org/10.1016/J.COGSC.2018.04.019.

[83] S. Pindar, N. Dhawan, Evaluation of in-situ microwave reduction for metal recovery from spent lithium-ion batteries, Sustainable Materials and Technologies 25 (2020) e00201. https://doi.org/10.1016/J.SUSMAT.2020.E00201.

[84] L. Brückner, J. Frank, T. Elwert, Industrial Recycling of Lithium-Ion Batteries—A Critical Review of Metallurgical Process Routes, Metals 2020, Vol. 10, Page 1107 10 (2020) 1107. https://doi.org/10.3390/MET10081107.

[85] J. Diekmann, C. Hanisch, L. Froböse, G. Schälicke, T. Loellhoeffel, A.-S. Fölster, A. Kwade, Ecological Recycling of Lithium-Ion Batteries from Electric Vehicles with Focus on Mechanical Processes, J Electrochem Soc 164 (2017) A6184–A6191. https://doi.org/10.1149/2.0271701JES/XML.

[86] Duesenfeld, Low energy consumption and highest recovery rates, (n.d.). https://www.duesenfeld.com/recycling_en.html (accessed November 21, 2023).

[87] Fortum, Lithium-ion Battery Recycling Technology, (n.d.). https://www.fortum.com/services/battery-recycling/lithium-ion-battery-recycling-technology (accessed November 21, 2023).

[88] Stena Recycling, Stena Recycling opens industry scale battery recycling plant in Europe, (2023). https://www.stenarecycling.com/news-insights/news-room/2023/stena-recycling-opens-industry-scale-battery-recycling-plant-in-europe/ (accessed November 21, 2023).

[89] K. Hebden, UK's first industrial scale lithium-ion battery recycling plant to open, The Chemical Engineer (2023). https://www.thechemicalengineer.com/news/uks-first-industrial-scale-lithium-ion-battery-recycling-plant-to-open/ (accessed November 21, 2023).

[90] F. Motasemi, M.T. Afzal, A review on the microwave-assisted pyrolysis technique, Renewable and Sustainable Energy Reviews 28 (2013) 317–330. https://doi.org/10.1016/J.RSER.2013.08.008.

[91] K.E. Haque, Microwave energy for mineral treatment processes—a brief review, Int J Miner Process 57 (1999) 1–24. https://doi.org/10.1016/S0301-7516(99)00009-5.

[92] D. El Khaled, N. Novas, J.A. Gazquez, F. Manzano-Agugliaro, Microwave dielectric heating: Applications on metals processing, Renewable and Sustainable Energy Reviews 82 (2018) 2880–2892. https://doi.org/10.1016/J.RSER.2017.10.043.

[93] Y.F. Huang, P. Te Chiueh, S.L. Lo, A review on microwave pyrolysis of lignocellulosic biomass, Sustainable Environment Research 26 (2016) 103–109. https://doi.org/10.1016/J.SERJ.2016.04.012.

[94] M. Omran, Microwave dephosphorisation of high phosphorus iron ores of the Aswan region, Egypt : developing a novel process for high phosphorus iron ore utilization, (2015).

[95] P. Yadoji, R. Peelamedu, D. Agrawal, R. Roy, Microwave sintering of Ni–Zn ferrites: comparison with conventional sintering, Materials Science and Engineering: B 98 (2003) 269–278. https://doi.org/10.1016/S0921-5107(03)00063-1.

[96] A.B. Haruna, K.I. Ozoemena, Effects of microwave irradiation on the electrochemical performance of manganese-based cathode materials for lithium-ion batteries, Curr Opin Electrochem 18 (2019) 16–23. https://doi.org/10.1016/J.COELEC.2019.08.005.

[97] D.A.C. Stuerga, P. Gaillard, Microwave Athermal Effects in Chemistry: A Myth's Autopsy: Part II: Orienting effects and thermodynamic consequences of

electric field., Journal of Microwave Power and Electromagnetic Energy 31 (1996) 101–113. https://doi.org/10.1080/08327823.1996.11688300.

[98] Z. Peng, J.Y. Hwang, J. Mouris, R. Hutcheon, X. Huang, Microwave Penetration Depth in Materials with Non-zero Magnetic Susceptibility, ISIJ International 50 (2010) 1590–1596. https://doi.org/10.2355/ISIJINTERNATIONAL.50.1590.

[99] D.E. Clark, D.C. Folz, J.K. West, Processing materials with microwave energy, Materials Science and Engineering: A 287 (2000) 153–158. https://doi.org/10.1016/S0921-5093(00)00768-1.

[100] S. Agrawal, V. Rayapudi, N. Dhawan, Comparison of microwave and conventional carbothermal reduction of red mud for recovery of iron values, Miner Eng 132 (2019) 202–210. https://doi.org/10.1016/J.MINENG.2018.12.012.

[101] R. Roy, D. Agrawal, J. Cheng, S. Gedevanlshvili, Full sintering of powdered-metal bodies in a microwave field, Nature 1999 399:6737 399 (1999) 668–670. https://doi.org/10.1038/21390.

[102] J. Tang, Unlocking Potentials of Microwaves for Food Safety and Quality, J Food Sci 80 (2015) E1776–E1793. https://doi.org/10.1111/1750-3841.12959.

[103] Y. Liu, Y. Zhang, Y. Liu, J. Zhu, Z. Ge, Z. Li, Y. Chen, Super heating/cooling rate enabled by microwave shock on polymeric graphene foam for high performance Lithium–Sulfur batteries, Carbon N Y 173 (2021) 809–816. https://doi.org/10.1016/J.CARBON.2020.11.061.

[104] K.Y. Foo, B.H. Hameed, Microwave-assisted regeneration of activated carbon, Bioresour Technol 119 (2012) 234–240. https://doi.org/10.1016/J.BIORTECH.2012.05.061.

[105] X. Li, F.I. Hai, L.D. Nghiem, Simultaneous activated carbon adsorption within a membrane bioreactor for an enhanced micropollutant removal, Bioresour Technol 102 (2011) 5319–5324. https://doi.org/10.1016/J.BIORTECH.2010.11.070.

[106] S. Kumar N, D. Grekov, P. Pré, B.J. Alappat, Microwave mode of heating in the preparation of porous carbon materials for adsorption and energy storage applications – An overview, Renewable and Sustainable Energy Reviews 124 (2020) 109743. https://doi.org/10.1016/J.RSER.2020.109743.

[107] S. Kosai, D. Kurogi, K. Kozaki, E. Yamasue, Distributed recycling system with microwave-based heating for obsolete alkaline batteries, Resources, Environment and Sustainability 9 (2022) 100071. https://doi.org/10.1016/J.RESENV.2022.100071.

[108] C. Yuwen, B. Liu, H. Zhang, S. Tian, L. Zhang, S. Guo, B. Zhou, Efficient recovery and regeneration of waste graphite through microwave stripping from spent batteries anode for high-performance lithium-ion batteries, J Clean Prod 333 (2022) 130197. https://doi.org/10.1016/J.JCLEPRO.2021.130197.

[109] D. Hou, Z. Guo, Y. Wang, X. Hou, S. Yi, Z. Zhang, S. Hao, D. Chen, Microwave-assisted reconstruction of spent graphite and its enhanced energy-storage performance as LIB anodes, Surfaces and Interfaces 24 (2021) 101098. https://doi.org/10.1016/J.SURFIN.2021.101098.

[110] Y. Zhao, B. Liu, L. Zhang, S. Guo, Microwave-absorbing properties of cathode material during reduction roasting for spent lithium-ion battery recycling, J Hazard Mater 384 (2020) 121487. https://doi.org/10.1016/J.JHAZMAT.2019.121487.

[111] S. Pindar, N. Dhawan, Recycling of mixed discarded lithium-ion batteries via microwave processing route, Sustainable Materials and Technologies 25 (2020) e00157. https://doi.org/10.1016/J.SUSMAT.2020.E00157.

[112] S. Lin, R. Liu, S. Guo, High temperature microwave dielectric and thermochemical properties of waste LixMn2O4 battery cathode materials reduced by moso bamboo, Renew Energy 181 (2022) 714–724. https://doi.org/10.1016/J.RENENE.2021.09.055.

[113] S. Pindar, N. Dhawan, Rapid recycling of spent lithium-ion batteries using microwave route, Process Safety and Environmental Protection 147 (2021) 226–233. https://doi.org/10.1016/J.PSEP.2020.09.012.

[114] A. Fahimi, I. Alessandri, A. Cornelio, P. Frontera, A. Malara, E. Mousa, G. Ye, B. Valentim, E. Bontempi, A microwave-enhanced method able to substitute traditional pyrometallurgy for the future of metals supply from spent lithium-ion batteries, Resour Conserv Recycl 194 (2023) 106989. https://doi.org/10.1016/J.RESCONREC.2023.106989.

[115] Y. Fu, Y. He, Y. Yang, L. Qu, J. Li, R. Zhou, Microwave reduction enhanced leaching of valuable metals from spent lithium-ion batteries, J Alloys Compd 832 (2020) 154920. https://doi.org/10.1016/J.JALLCOM.2020.154920.

[116] LibreTexts, X-ray diffraction (XRD) basics and application, in: Materials Characterization Fundamentals, n.d. https://chem.libretexts.org/Courses/Franklin_and_Marshall_College/Introduction_to_Materials_Characterization__CHM_412_Collaborative_Text/Diffraction_Techniques/X-ray_diffraction_(XRD)_basics_and_application (accessed January 29, 2024).

[117] A. Bijelic, A. Rompel, Polyoxometalates: more than a phasing tool in protein crystallography, ChemTexts 4 (2018). https://doi.org/10.1007/S40828-018-0064-1.

[118] D. Henry, N. Eby, J. Goodge, D. Mogk, X-ray reflection in accordance with Bragg's Law, (2024). https://serc.carleton.edu/msu_nanotech/methods/BraggsLaw.html (accessed January 30, 2024).

[119] Britannica, Bohr model, (n.d.). https://www.britannica.com/science/Bohr-model (accessed February 14, 2024).

[120] Agilent, An Introduction to the Fundamentals of Inductively Coupled Plasma – Optical Emission Spectroscopy (ICP-OES), (n.d.). https://www.agilent.com/en/support/atomic-spectroscopy/inductively-coupled-plasma-optical-emission-spectroscopy-icp-oes/icp-oes-faq (accessed February 2, 2024).

[121] V. Rantala, M. Kokko, R. Suvela, M. Manninen, T. Hu, U. Lassi, J. Pesonen, S. Tuomikoski, Elemental Concentrations of Natural Graphite and Steelmaking Slag: Development of Microwave-Assisted Acid Digestion, Anal Lett (2023). https://doi.org/10.1080/00032719.2023.2289083.

[122] S. Swapp, Scanning Electron Microscopy (SEM), Geochemical Instrumentation and Analysis (n.d.). https://serc.carleton.edu/research_education/geochemsheets/techniques/SEM.html (accessed February 7, 2024).

[123] M.K. Singh, A. Singh, Scanning electron microscope, Characterization of Polymers and Fibres (2022) 387–419. https://doi.org/10.1016/B978-0-12-823986-5.00008-7.

[124] Ted Pella Inc., Electron Microscopy Sciences, Micros Today 26 (2018) 10–10. https://doi.org/10.1017/S155192951800010X.

[125] N.F.A. Zainal, J.M. Saiter, S.I.A. Halim, R. Lucas, C.H. Chan, Thermal analysis: Basic concept of differential scanning calorimetry and thermogravimetry for beginners, Chemistry Teacher International 3 (2021) 59–75. https://doi.org/10.1515/CTI-2020-0010/DOWNLOADASSET/SUPPL/J_CTI-2020-0010_SUPPL_004.PDF.

[126] U. of P. Department of Chemistry, Mass Spectrometry Introduction, (n.d.). https://www.chem.pitt.edu/facilities/mass-spectrometry/mass-spectrometry-introduction (accessed February 12, 2024).

[127] Y. Zhang, W. Wang, Q. Fang, S. Xu, Improved recovery of valuable metals from spent lithium-ion batteries by efficient reduction roasting and facile acid leaching, Waste Management 102 (2020) 847–855. https://doi.org/10.1016/J.WASMAN.2019.11.045.